Radiation tolerance studies of the double sided silicon strip sensor

(両面ストリップ型シリコンセンサーの放射線耐性評価)

By

Fumiaki Otani

男谷　文彰

A Master Thesis

修士論文

Submitted to

The University of Tokyo

Department of Physics, Graduate School of Science

On 2023/01/27

Thesis Supervisor: Takeo Higuchi　樋口　岳雄

ABSTRACT

The B meson decays can be studied precisely and compared with the standard model (SM) to search for new physics of elementary particles. The Belle II experiment, which has an accelerator and detector in Tsukuba, Ibaraki, Japan, is also called the "B factory" experiment, and produces many B mesons and can precisely measure their decays.

Currently, efforts are underway to bring the beam luminosity of the SuperKEKB collider to $6 \times 10^{35}\,\mathrm{cm}^2/\mathrm{s}$ for the Belle II experiment. While an increase in beam luminosity increases the number of B produced and allows for more precise measurements, the beam background also increases with beam luminosity. Therefore, radiation damage to the detector is also expected to worsen. In particular, the innermost layer of the Silicon Vertex Detector (SVD), which plays an important role in the search for new physics, is simulated to receive 20 kGy of radiation after 10 years of target luminosity operation. We decided to investigate whether there would be any problems with the operation of the SVD after receiving this radiation dose through the electron beam irradiation test.

In order to evaluate the radiation hardness of the SVD sensor, a measurement system was developed that allowed for the remote measurement of the leakage current-voltage characteristics (IV), capacitance-voltage (CV), and interstrip capacitance-voltage (cint) of the sensor. The system was used to focus on the stepwise changes in IV, CV, and $\mathrm{C_{int}}$with a radiation dose up to 100 kGy for the TID and $3 \times 10^3 \mathrm{n_{eq}} 1/\mathrm{cm}^2$ for the NIEL. Additionally, changes in noise and charge collection efficiency were measured before and after irradiation of the sensor by utilizing a signal readout module equipped with a readout ASIC that was attached to the sensor.

The evaluation results confirm that our SVD has no operational problems even after 10 years of cumulative radiation dose under beam luminosity $6 \times 10^{35}\,\mathrm{cm}^2/\mathrm{s}$.

Contents

Chapter 1

Introduction

1.1 Physics motivation

1.1.1 New physics

The Standard Model (SM) of particle physics explains the experimental results to date well and without contradiction. However, there are still many things that the SM cannot explain. For example, it cannot explain what has become the imbalance between matter and antimatter in this world (matter-dominated universe). Therefore, the SM is not believed to be yet the ultimate theory "theory of everything" that can explain all particle behaviors of the universe. Therefore, we search for a new theory of particles by precisely measuring their reactions and looking for deviations from the standard theory.

In particular, decays involving the $b \to s\gamma$ processes are sensitive to the new theory.

The $b \to s\gamma$ process is allowed in the SM only through W boson one loop as Fig. 1.1. Because the parity breaking occurs here, the gammas that appear in the final state are predominantly left- or right-handed, as shown by the pair of solid arrows in Fig. 1.2; the direction of the dashed arrow is strongly suppressed in the SM. Therefore, B^0 and $\overline{B}^0$ decay into $X_s\gamma$ are independent and the CP asymmetry is supressed. For example, the CP asymmetry of the process $B^0 \to K_S^0\pi^0\gamma$ mediated by the $b \to s\gamma$ transition is theoretically expected to be $\mathcal{S}_{CP} \approx -0.023 \pm 0.016$ suppressed by $(2m_s)/m_b$ [6].

On the other hand, if there are new physics in this loop that can contribute the $b \to s\gamma$ process regardless of whether the photon is left- or right-handed, the percentage of events in the direction of the dashed arrow in Fig. 1.2 will increase, and CP asymmetry is no longer zero and can be significant. From the above, it is possible to look for new physics by actually measuring the CP asymmetry $\mathcal{S}_{CP}$ by precisely measuring the events involving $b \to s\gamma$. To experimentally measure the CP asymmetry, the Time Dependent CP Violation (TDCPV) method is used.

1.1.2 Belle II experiment and TDCPV method

The Belle II experiment is a high energy experiment, uses the SuperKEKB collider and Belle II detector at the High Energy Accelerator Research Organization in Tsukuba, Ibaraki, Japan. Electron and positron beams produced at the SuperKEKB accelerator collide, and particle reactions are recorded by the Belle II detector. The collision energy of the beams is set to the $\Upsilon(4S)$ resonant mass energy and the SuperKEKB can produce a large amount of $\Upsilon(4S)$ mesons by its high beam luminosity. $\Upsilon(4S)$ then decays into B $\overline{B}$ pair. In other words, the Belle II experiment is provided with a large amount of B meson by SuperKEKB and its decay

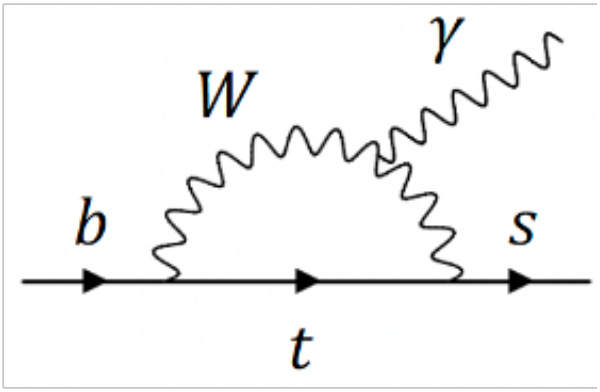

Figure 1.1: $b \to s\gamma$ diagram

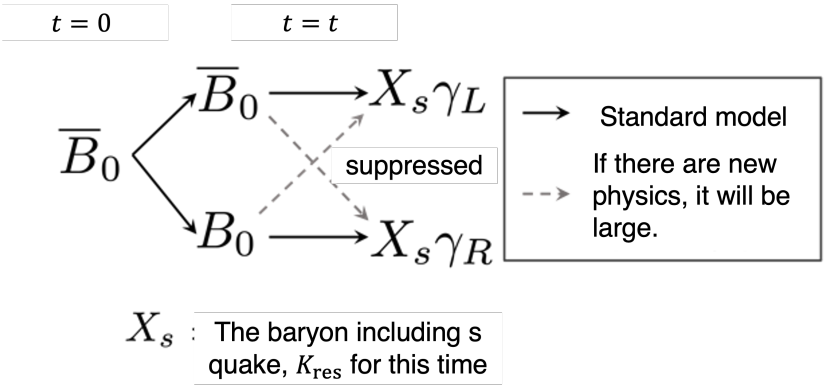

Figure 1.2: Photon polarization in B meson decay. $\gamma_L(\gamma_R)$ represents Left-(Right-) handed photon.

events can be observed, thus, the Belle II experiment is well suited for the precise measurement of $b \to s\gamma$.

Since the $X_s\gamma$ state is the CP-specific decay mode for B and $\overline{B}$, theoretically, the CP asymmetry is seen in the difference between the time-dependent decay widths $\Gamma_{B\to X_s^{CP}\gamma}(t)$ of B and $\overline{B}$ as the following equation [15],

$$\text{Asym.} = \frac{\Gamma_{\overline{B}^0\to X_s^{CP}\gamma}(t) - \Gamma_{B^0\to X_s^{CP}\gamma}(t)}{\Gamma_{\overline{B}^0\to X_s^{CP}\gamma}(t) + \Gamma_{B^0\to X_s^{CP}\gamma}(t)} = \mathcal{A}_{CP}\cos(\Delta mt) + \mathcal{S}_{CP}\sin(\Delta mt) \quad , \tag{1.1}$$

so, we can obtain the CP asymmetry by measuring the time-dependent decay widths of $X_s\gamma$ each of B and $\overline{B}$.

1.2 Motivation of this thesis

In the experiment, the decay time t of $\Gamma_{B\to X_s^{CP}\gamma}(t)$ is calculated from the decay point. Therefore, the precise determination of the decay vertices of the B mesons is essential to precisely measure the of the CP asymmetry, and in the Belle II experiment, the silicon vertex detector (SVD) plays an important role in the measurement of the decay vertices of the B mesons.

In the Belle II experiment, it is planned to increase the peak luminosity of the SuperKEKB collider to $6 \times 10^{35}\,\mathrm{cm}^2/\mathrm{s}$. This increase in luminosity will result in a higher number of events produced, thus providing a more accurate measurement of $btos\gamma$. However, it is also anticipated that the increased luminosity will lead to a higher beam background. Consequently, it is imperative to estimate the effect of the radiation damage caused to the SVD by the higher beam background will pose a problem for SVD operation. In particular, the amount of radiation received during 10 years of operation at the target luminosity ($\approx 20\,\mathrm{kGy}$) will be used as an indicator to confirm that the operation will not be affected by the amount of radiation received. For confirmation, we decide to actually irradiate electron beams to the SVD to inversticate the effects from the NIEL damage mainly.

The previous studies have investigated the effects of Total Ionizing Dose (TID) damage on SVD up to 100 kGy using ^{60}Co [24] radiation, however, no studies have been conducted on Non-Ionizing Energy Loss (NIEL) effects. Despite this, the Silicon Vertex Tracker (SVT) [9] used in the Babar experiment has similar characteristics to our SVD and based on the results of SVT irradiation tests [21], it can be inferred that our sensor also possesses sufficient radiation tolerance to withstand NIEL effects in practical use, and its has been used to date.

Chapter 2

Belle II detector

2.1 Overview of the Belle II detector

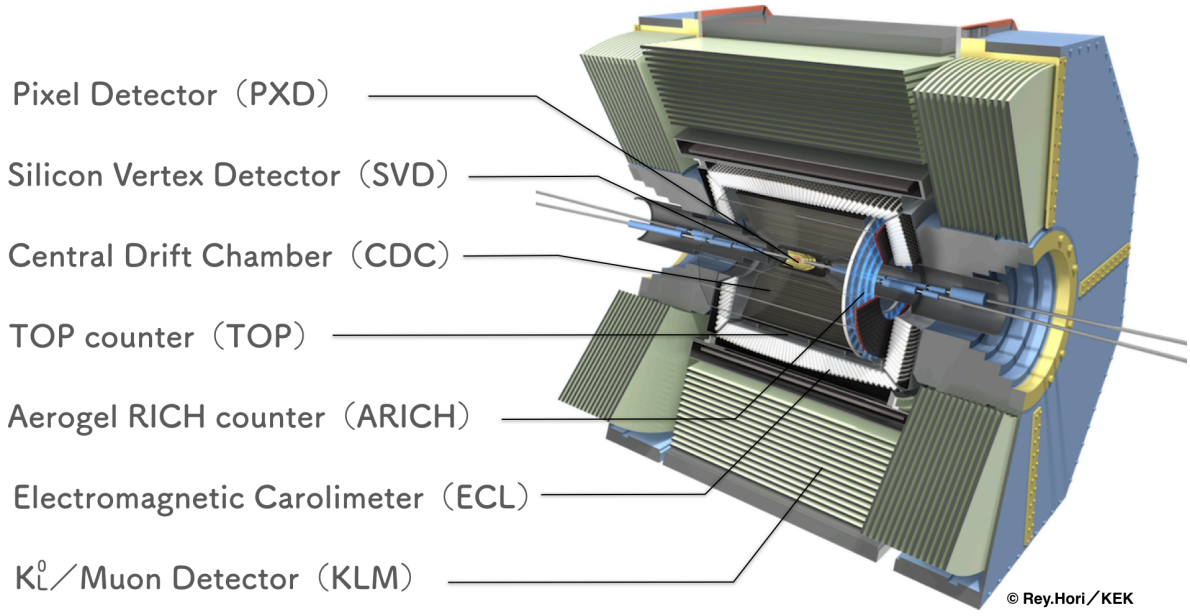

Figure 2.1: Overview of the Belle II detector [22]

The Belle II detector Fig. 2.1 [10] has a near cylindrical shape with a diameter of approximately 8 meters. At the center of the detector is the interaction point (IP) of the electron and positron beams produced by SuperKEKB (detail in Sec. 3.1), with various sub-detectors covering the IP in an onion-like structure.

This thesis focuses on the Silicon Vertex Detector (SVD) [2] and briefly introduces the other sub-detectors, presented in order of proximity to the IP:

Pixel Detector (PXD) The design consists of two layers of PXD sensors, with 8 sensors in the inner layer and 12 sensors in the outer layer, placed 14 mm and 22 mm from the IP, respectively. The sensors are made of silicon and each sensor has 250×768 pixels of size $50 \times (55 \sim 85\,\mu m^2)$. Each pixel serves as a signal readout channel. The sensors are used

in a fully depleted state, similar to the SVD. When a particle passes through, the nearest pixel collects the charge generated by the passing particle and identifies the position of the particle as a signal. Together with the SVD, the system is called the VeteX Detector (VXD) and uses the positions of the particles passing through the PXD two layers and the SVD four layers to reconstruct the trajectories of the passing particles and estimate the point of generation of the particles (the point of decay of the parent particle)

Silicon Vertex Detector (SVD) See Sec. 2.2

Central Drift Chamber (CDC) The CDC is a cylindrical gas-chambered detector with an inner diameter of 32 cm and an outer diameter of 226 cm, which exists in the outer layer of the SVD. The inside of the detector is lined with a large number of gold-plated tungsten wires of 30 µm diameter and aluminum alloy wires of 126 µm diameter and is filled with a mixture of helium and ethane gas. The aluminum alloy wires are called field wires and are not voltage-applied, whereas the gold-plated tungsten wires are called sense wires and are voltage-applied. One sense wire is surrounded by eight field wires, which are the cells of the CDC measurement. When charged particles pass through this cell, they ionize the gas, producing electrons. These electrons move toward the sense wire due to the voltage difference in the cell, causing an electron avalanche and then a signal will be generated.

It measures the trajectory of the charged particles and uses the obtained trajectory to measure the momentum of the charged particles and to generate trigger signals. In addition, the $\mathrm{d}E/\mathrm{d}x$ of the particles in the gas can be measured, and the particles can be identified.

Time Of Propagation counter (TOP) The TOP counter is installed outside the CDC. It consists of a quartz radiator 2.7 m long, 45 cm wide, and 2 cm thick, and a Micro-Channel-Plate Photo-Multiplier Tube (MCP-PMT) placed at the end. When a particle passes through the radiator of the TOP counter and its velocity exceeds c/n, Cherenkov light is generated. (c is the speed of light and n is the refractive index of the radiator) The Cherenkov light reaches the MCP-PMT and becomes a signal while being totally reflected inside the radiator.

Using the fact that the emission angle of Cherenkov light is larger for particles with the same momentum but smaller mass, we can identify particles based on the difference in the propagation time of Cherenkov light. It is particularly good at identifying π and K.

Aerogel Ring Imaging CHerenkov counter (ARICH) ARICH is installed near the end cap portion of the CDC on the right side of Fig. 2.1. The ARICH is composed of a radiator composed of a silica aerogel with an outer diameter of 1.1 m, an inner diameter of 0.4 m, and a thickness of 40 mm, as well as a Hybrid Avalanche Photo-Detector (HAPD) with a thickness of 30 mm. The HAPD and radiator are separated by a distance of 160 mm.

Similar to the TOP, when charged particles pass through the radiator, Cherenkov light is produced. The Hybrid Avalanche Photo-Detector (HAPD) receives this produced light and performs particle identification (of π and K) by reconstructing the Cherenkov ring.

Electromagnetic Carolimeter (ECL) The ECL is placed outside of the ARICH and the TOP counter to enclose detectors and other detectors mentioned above (White area in

Fig. 2.1). A set of cmthallium-doped caesium iodide CsI(Tl) crystals of approximately 30 cm × 5.5 cm × 5.5 cm size combined with a PIN-PD (PhotoDiode) is used as a scintillation detector. This scintillation detector set is used 8736 sets in the ECL. As the gamma rays and electrons pass through the ECL crystal, an electromagnetic shower is generated, and the particles lose energy in the electromagnetic shower. On the other hand, scintillation light is emitted in proportion to the energy lost. By measuring the scintillation light, the total energy of each particle can be calculated.

K-Long-Muon detector (KLM) The KLM is the Belle II detector outermost detector. 14 steel plates about 4.7 cm thick are spaced about 4.4 cm apart. The detector is placed between them. The detector is basically a Resistive Plate Counter (RPC), and a part of the detector (the end cap and the innermost two layers of the barrel section) uses a strip plastic scintillator as a detector.

The charged particles that reach the KLM are occupied by muons or K_L^0, and the KLM distinguishes between these two types of particles. Muon penetrates the steel plates in the KLM and leave trails on the detector, while K_L^0 interacts with iron and form hadron showers. In this way, the particles are distinguished by the difference in their tracks.

2.2 Silicon Vertex Detector

The SVD is arranged in four cylindrical layers that wrap around the PXD as shown in Fig. 2.2. Each layer consists of a ladder with a different shape in each layer as shown in Fig. 2.3. Each of the innermost layer 3, as well as layers 4, 5, and 6, consists of 7, 10, 12, and 16 ladders, respectively. An example of the ladder structure is shown in Fig. 2.4.

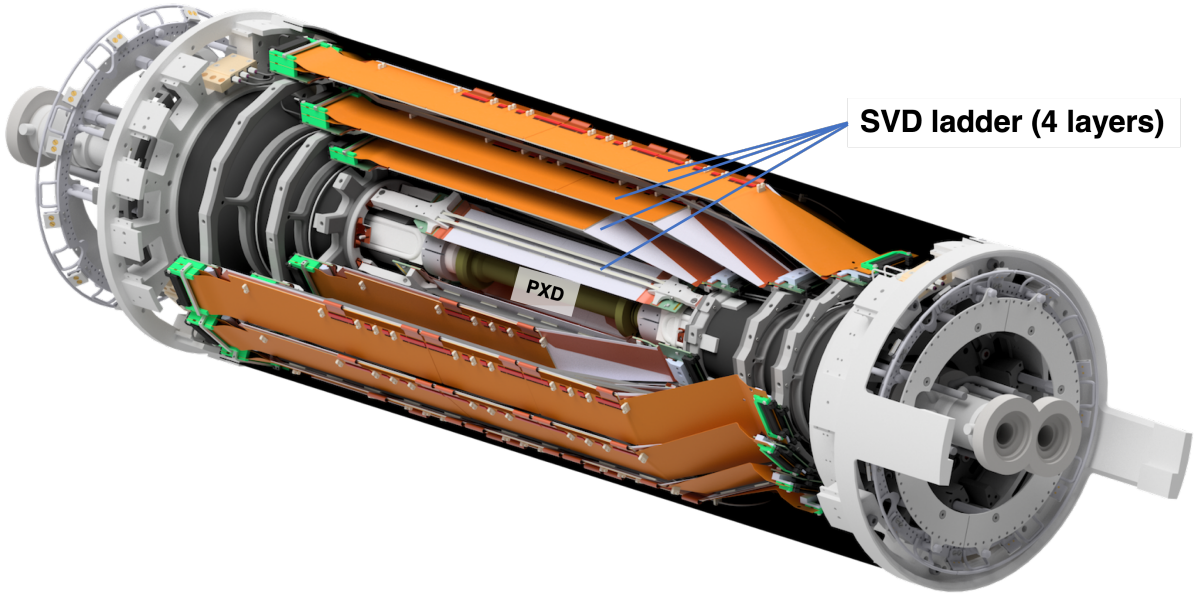

Figure 2.2: The Belle II vertex detector, Constructed with two layers PXD and four SVD layers.

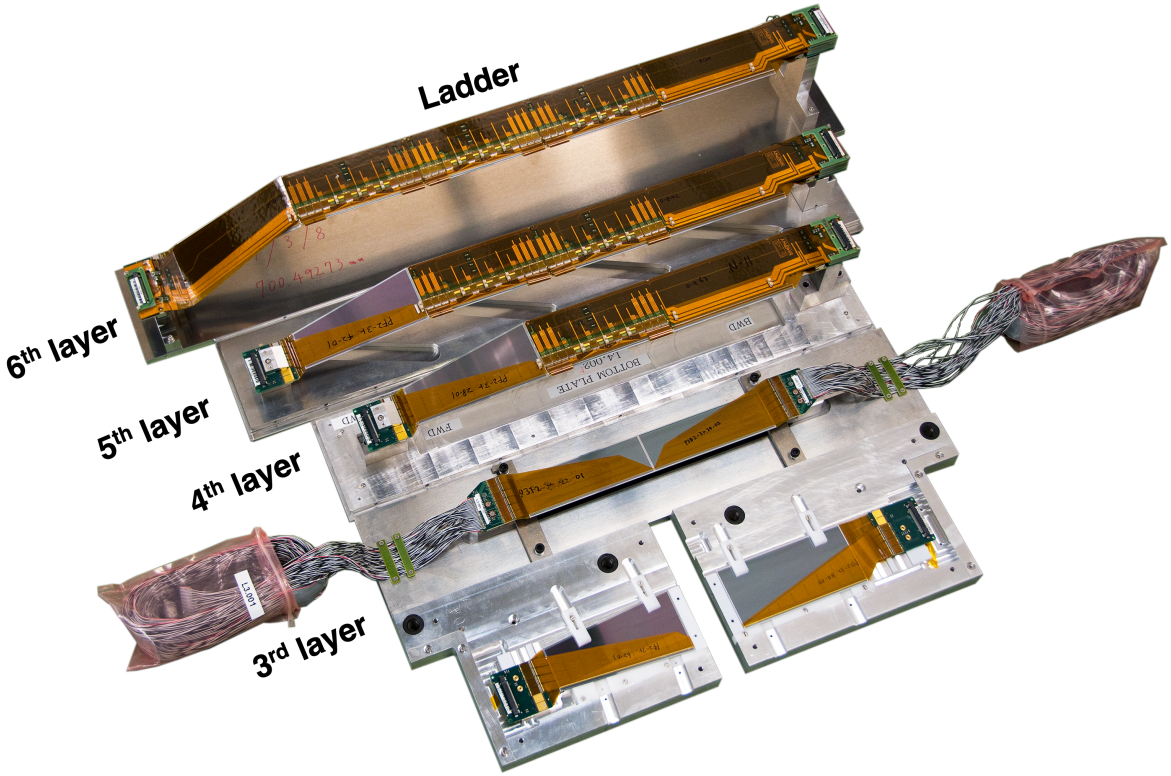

Figure 2.3: Ladders for each layer

2.2.1 Double-sided strip detectors

The DSSD is an SVD sensor and one of the most important parts of the SVD to capture the position of the particles as they pass through. A more detailed principle of operation is described below (Sec. 3.3). The structure and overview are described here.

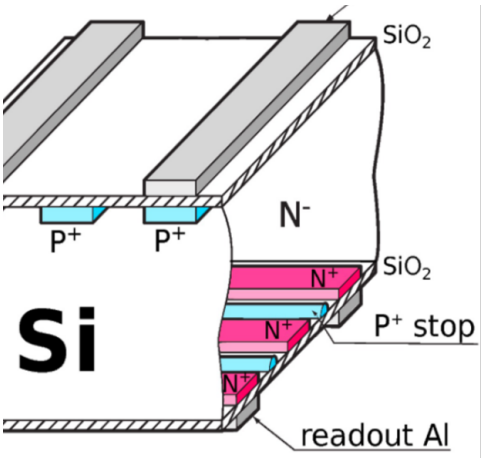

Figure 2.5: The strip structure of the DSSD, SVD sensor.

DSSD is a semiconductor detector, and the bulk of the sensor is an n-type semiconductor.

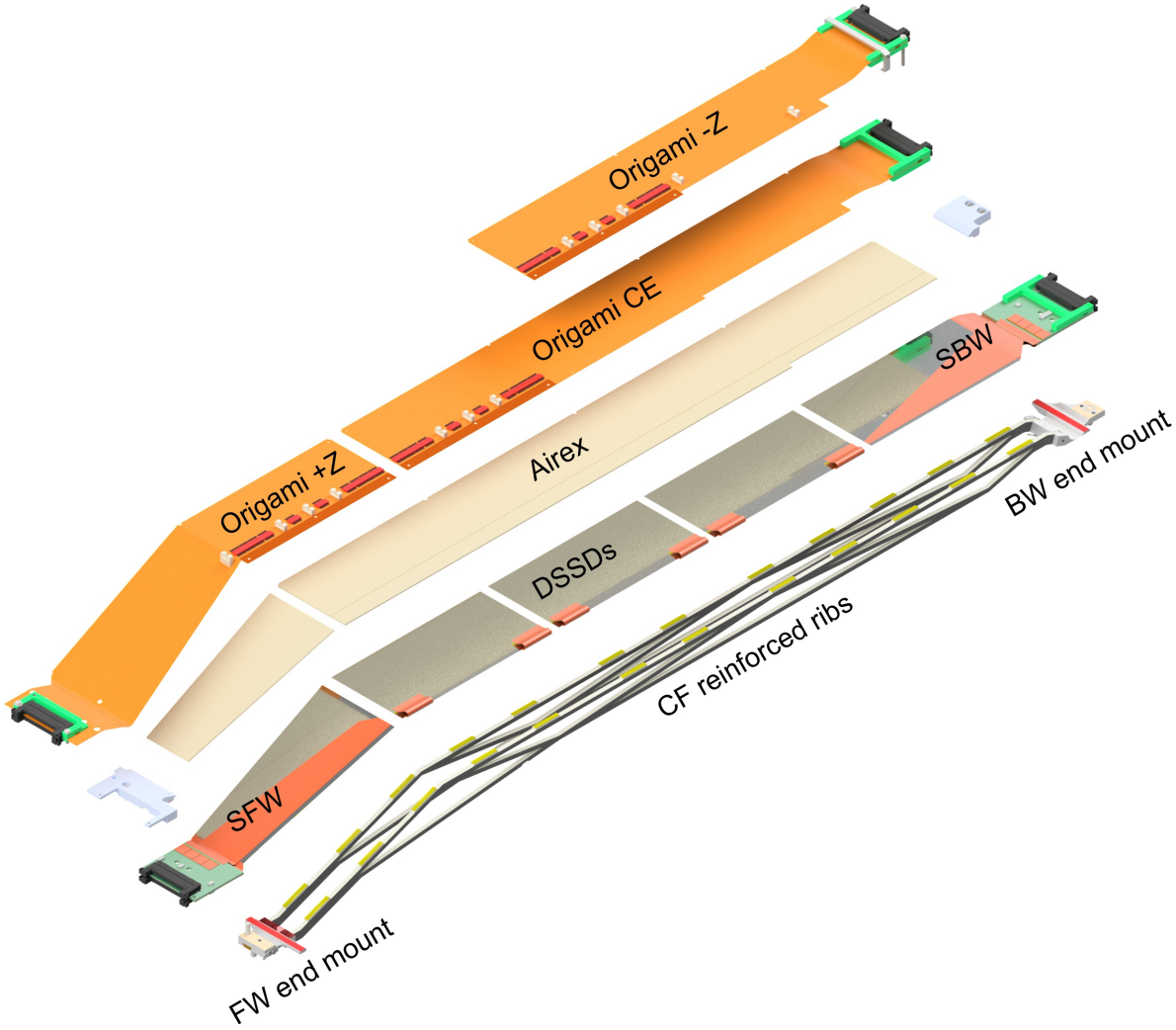

Figure 2.4: Example of ladder structure, the 6th layer ladder

It has a strip-like structure on both surfaces of its bulk, as shown in Fig. 2.5. The individual strips are also semiconductors, but they are much more highly doped with impurities than the bulk semiconductor; one side (called P side) uses P^+ strips with high acceptor concentration and the other side (called N side) uses N^+ strips with high donor concentration.

The entire sensor can be depleted by applying a voltage between the P^+ and N^+ strips. When a particle passes through this depleted DSSD, the P^+ and N^+ strips near the point of passage react; since the P^+ and N^+ strips are orthogonal, the point of passage can be estimated in two dimensions. Each strip on both sides is coupled to an aluminum strip that has undergone a SiO_2 oxide coating. Through this aluminum strip, signals can be read out to the outside of the sensor (to ASIC; APV25). In addition, the Belle II DSSD has a P^+ strip (called P^+ stop) between the N^+ strips, which does not have a small readout, and the space between the N^+ strips is wider than the P side, and the sensor bulk is N-type bulk, which makes it difficult to apply voltage. Therefore, depletion is difficult to occur, and the P^+ stop is placed to completely isolate the strips from each other.

Hereafter, P^+ and N^+ strips will be referred to simply as P strips and N strips, respectively.

DSSDs are incorporated into the SVD ladder as shown in Fig. 2.4. Each layer has a different number and different geometries of DSSDs in a single ladder. The DSSDs showed in table 2.1. As can be seen in Fig. 2.3 and Fig. 2.4, there is an angled fabricated section on the rudder after layer 4. That section also has a DSSD, which is a trapezoidal DSSD. That part we call SVD Forward (SFW) and the other end we call SVD Backward (SBW).

	Small rectangular	Large rectangular	Trapezoidal
Readout strips P-side	768	768	768
Readout strips N-side	768	512	512
Readout pitch P-side (μm)	50	75	$50 \sim 75$
Readout pitch N-side (μm)	160	240	240
Sensor active area (mm^2)	122.90×38.55	122.90×57.72	$122.76 \times (38.42 \sim 57.59)$
Sensor thickness (μm)	320	320	300
The number in layer3 ladder	2	0	0
The number in layer4 ladder	0	2	1 (for SFW)
The number in layer5 ladder	0	3	1 (for SFW)
The number in layer6 ladder	0	4	1 (for SFW)

Table 2.1: The properties of three types of double-sided strip detector

2.2.2 Front-end readout ASIC: APV25

The DSSD strip is connected to the readout ASIC; APV25 [11], and the signal induced on the strip is shaped and amplified by APV25 and sent to the subsequent stage. One chip has 128 readout channels. The APV25 has fast shaping time 50 ns, and high radiation tolerance; It has been confirmed that the system works fine even after 100 Mrad irradiation [16].

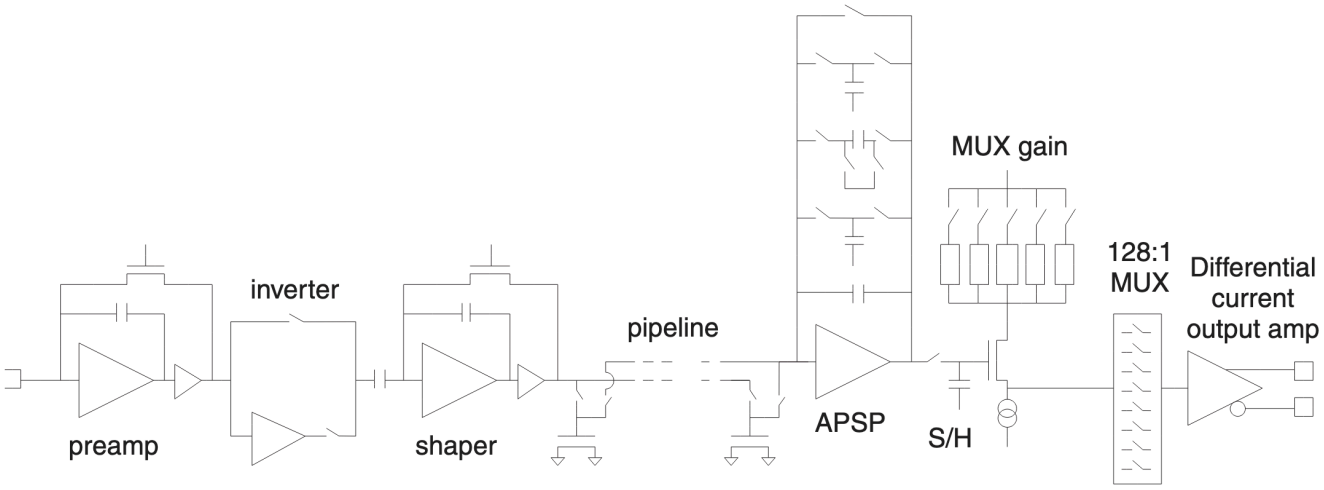

Figure 2.6: Block diagram of the one channel of the APV25

Chapter 3

SuperKEKB and the radiation dameges

3.1 SuperKEKB

3.1.1 Overview of SuperKEKB

The SuperKEKB collider [3] (Fig. 3.1) is a circular lepton collider with a circumference of 3 km located at the High Energy Accelerator Research Organization (KEK) in Tsukuba-city, Ibaraki-Pref., Japan. The Belle II detector measures the events produced by collisions of 7 GeV electrons and 4 GeV positrons. The Belle II experiment precisely tests the Standard Model of particle physics by observing a large number of events. In order to increase the number of physical events produced by the collider, the luminosity of the collider must be increased. The luminosity $\mathcal{L}$ is proportional to the following parameters in SuperKEKB;

$$\mathcal{L} \propto \gamma_{\pm} \frac{I_{\pm} \xi_{y\pm}}{{\beta_y}^*_{\pm}} \tag{3.1}$$

where γ: Lorenz factor, I: beam current, ξ_y: vertical beam-beam parameter, ${\beta_y}^*$: vertical beta function at the beam collisions point. The subscript $\pm$ indicates electron $(-)$ and positron $(+)$. The target values for those values are summarized in table. 3.1. The ξ parameter represents the electromagnetic effect from the current or the particles of one beam to the other, and while an increase in ξ is desirable in order to enhance luminosity, it has been observed through empirical evidence that there exists an upper limit $(0.1 \sim 0.2)$ beyond which improvement is not possible [29]. The beta function is an envelope function (for particle trajectories; related to beam size) determined by the collider optics (magnetic field) design. Compressing the beta function can increase luminosity, but if the beta function becomes narrower than the beam size, the beam bunch will take an hourglass shape, with a narrow center and bulges at the front and back. And, particle collisions within the finite area before and after the collision point also contribute to luminosity, so due to the bulging of the beam bunch, The luminosity can not be improved. In other words, the lower limit for the beta function is roughly equal to the beam size (hourglass effect). In order to reduce the achievable beta while taking into account the hourglass effect, a method of colliding beams at an angle ϕ with each other was considered [19], and was adopted in the SuperKEKB collider.

The SuperKEKB can be divided into two main parts: the main ring and the linac section which accelerates the beams. In the Linac section, electrons are first produced by a photocathode electron gun using the field emission effect. They are then accelerated through a Radio-Frequency (RF) cavity. A tungsten target for positron generation is placed in the middle

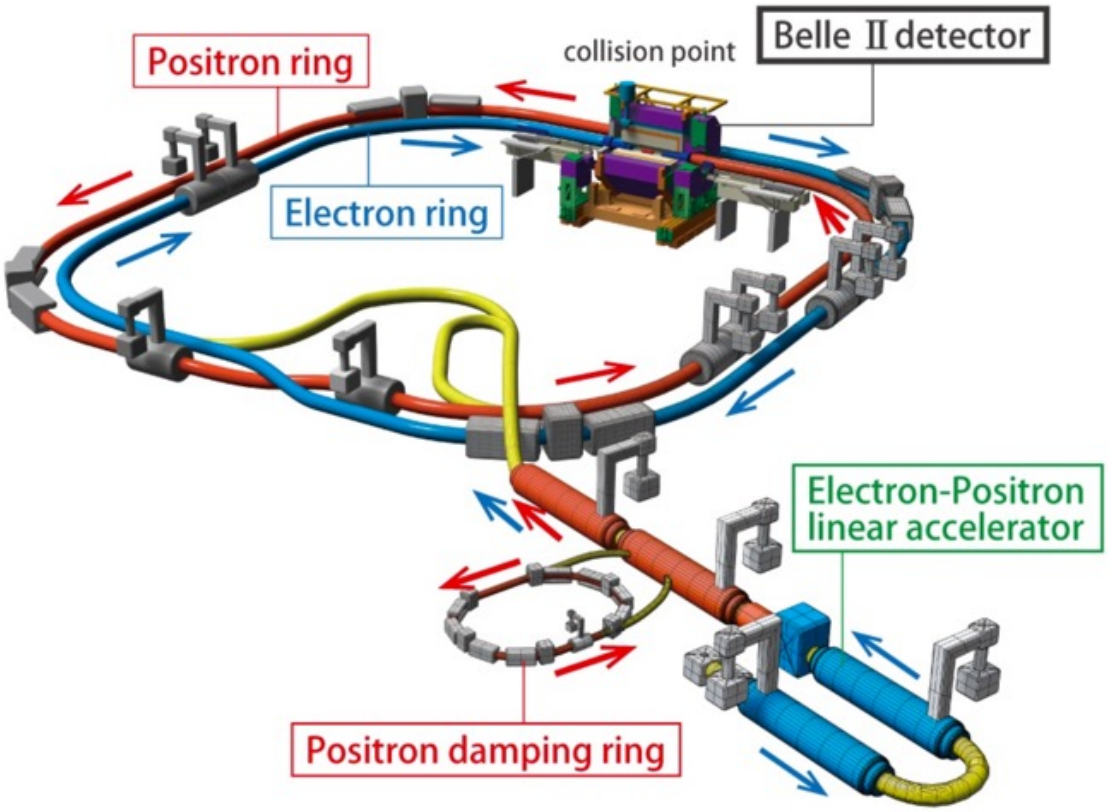

Figure 3.1: SuperKEKB collider

of the linac, and positrons are generated by striking the target with electrons. Electrons are produced at the photocathode, so the beam emittance (beam size and momentum spread) is small. Positrons, on the other hand, are produced and accelerated by pair production using tungsten as a catalyst to produce low-energy positrons. Therefore, the positron beam emittance is large. A positron damping ring was installed to reduce positron emittance. Emittance can be reduced by radiation damping when positrons are traveling in the damping ring. The electrons and positrons in the low emittance state are then injected into the main ring. Since electrons and positrons have very low mass, acceleration is completed in the linac section, and beam velocity is maintained and stored in the main ring. Then, the beams collide with each other at a sufficient timing.

Table 3.1: The designed parameters of the SuperKEKB collider [10]

	e^- beam (HER)	e^+ beam (LER)
Energy [GeV]	7.0	4.0
Beam current I [A]	2.62	3.60
ξ_y	0.088	0.090
${\beta_y}^*$ [mm]	0.41	0.27

3.1.2 Future luminosity

On June 8, 2022, the peak luminosity $\mathcal{L}$ reached a value of $\mathcal{L} = 4.65 \times 10^{34}\,\mathrm{cm}^2/\mathrm{s}$, and the integrated luminosity $L = \int \mathcal{L} dt$ accumulated through the operation of the SuperKEKB collider was $L = 424\,\mathrm{fb}^{-1}$. The Belle II experiment is currently in the first long shutdown period for upgrading and is scheduled to resume in 2023. After that, SuperKEKB will continue to be enhanced, and continuous improvement of the instantaneous luminosity is planned. The current goal is to reach the peak luminosity of $\mathcal{L} = 6 \times 10^{35}\,\mathrm{cm}^2/\mathrm{s}$ by 2034. In addition to this goal, one benchmark is SuperKEKB's original design Luminosity $\mathcal{L}_{\mathrm{design}} = 8 \times 10^{35}\,\mathrm{cm}^2/\mathrm{s}$.

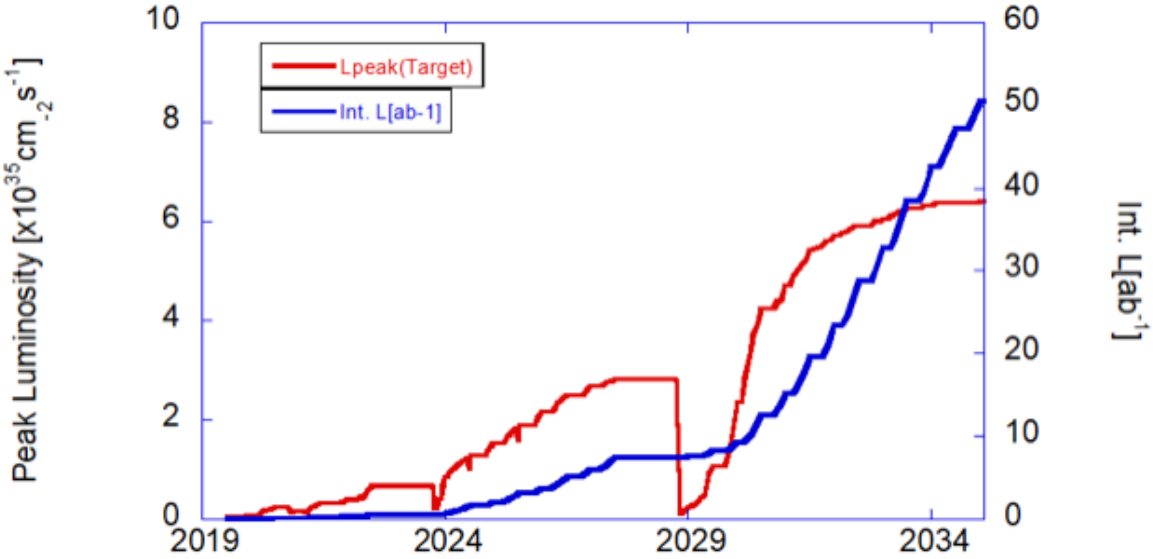

Figure 3.2: The Luminosity projection of SuperKEKB [1], The red line represents the planned peak luminosity, and the blue line represents the integrated luminosity

3.2 Beam background

Beam background refers to the phenomena described below that cause beam particles to deviate from the beam orbit and strike the beam pipe, producing electromagnetic showers, neutrons, *etc.* These are called the beam background. The background is not only noise to the physical event signal, but also damaging to the detector. In particular, because of the proximity of the SVD to the beam pipe at the point of impact, it is necessary to understand the damage caused by the background. The background can be classified into two types: Single beam backgrounds and luminosity-related backgrounds.

- **Single beam background**: Background due to reactions between particles in the beam bunch or with residual gas inside the beam ring.

  Touschek effect : Scattering by particles in a bunch of beams. Significant in positron ring (with low energy). The rate of occurrence increases in proportion to

$$\frac{{I_\pm}^2}{\sigma_{y_\pm} n_{b\pm} {E_\pm}^3} \tag{3.2}$$

where σ_y is the beam size, n_b is the number of beam bunch, and E is beam energy. Therefore, the rate of the Touschek effect occurring in the HER and the LER is different, and it is higher in the LER due to $E_+ < E_-$.

Coulomb scattering : Elastic Scattering of beam particles with residual gas particles in the beam pipe, which changes the direction of the particles; scattering of residual particles with nuclei: Rutherford scattering, scattering with electrons outside nuclei: Møller scattering. The rate of occurrence can be represented as follows

$$\text{rate} = \sigma_{\text{Coulomb}} N_{\text{beam}} N_{\text{nucl.}} \propto \sigma_{\text{Coulomb}} N_{\text{nucl.}} I_{\pm} \tag{3.3}$$

where σ_{Coulomb} is the cross-section of the Coulomb scattering, N_{beam} is the number of the beam particles in one circle of the ring, and $N_{\text{nucl.}}$ is the number of nuclei seen from the beam particles per barn per second. The rate increases in proportion to the beam current, so the rate at LER is higher due to $I_- < I_+$.

Bremsstrahlung (Brems) : Inelastic scattering caused by the electric field of an atomic nucleus. This scattering produces electromagnetic waves that reduce the energy of the beam particles. The particles with reduced energy are deflected off the ideal beam orbit by the deflector magnet. This influence is the strongest of the three.

The rate of the Bremsstrahlung can be obtained by rewriting σ_{Coulomb} in Eq. 3.3 as the cross-section of Bremsstrahlung $\sigma_{\text{Bremss.}}$. This means that the Bremsstrahlung also increases proportionally to the beam current, meaning that LER has a higher rate.

- **Luminosity related background**: Background caused by beam-to-beam collisions.

  Radiative Bhabha scattering $e^+e^- \to e^+e^-\gamma$, By emitting a gamma after beam impact, the electrons or positrons that have lost energy and hit the beam pipe, creating a background. The emitted gamma may also produce neutrons by hitting nearby magnets.

  Two-photons processes $e^+e^- \to e^+e^-(\gamma\gamma) \to e^+e^-e^+e^-$, Photons mediate the creation of new low-momentum electron-positron pairs, which become radiation to the VXD.

Increased luminosity is expected to increase luminosity related background especially. To date, the amount of beam background, around the SVD, generated during operation at designed luminosity $\mathcal{L}_{\text{design}} = 8 \times 10^{35}\,\text{cm}^2/\text{s}$ has been studied and reported using Monte Carlo simulation (MC) [2] [27]. Simulation results predict that the innermost (third) layer of the SVD will suffer the most radiation damage, exceeding 2 kGy in one snowmass year (smy; typical operation time of an collider facility in one year; 1×10^7 sec) with the designed luminosity, refer to Fig. 3.3.

The type of background radiation was also investigated in the simulations in the same way. Fig. 3.4 shows the results of weighting the amount of each particle with respect to the kinetic energy by the degree of damage each particle inflicts on the interior of the sensor in the innermost layer of the SVD in order to consider the damage to the sensor. In the high kinetic energy region (above 10 MeV), damage by electrons and positrons is dominant, while neutrons are higher in the region below 1 MeV.

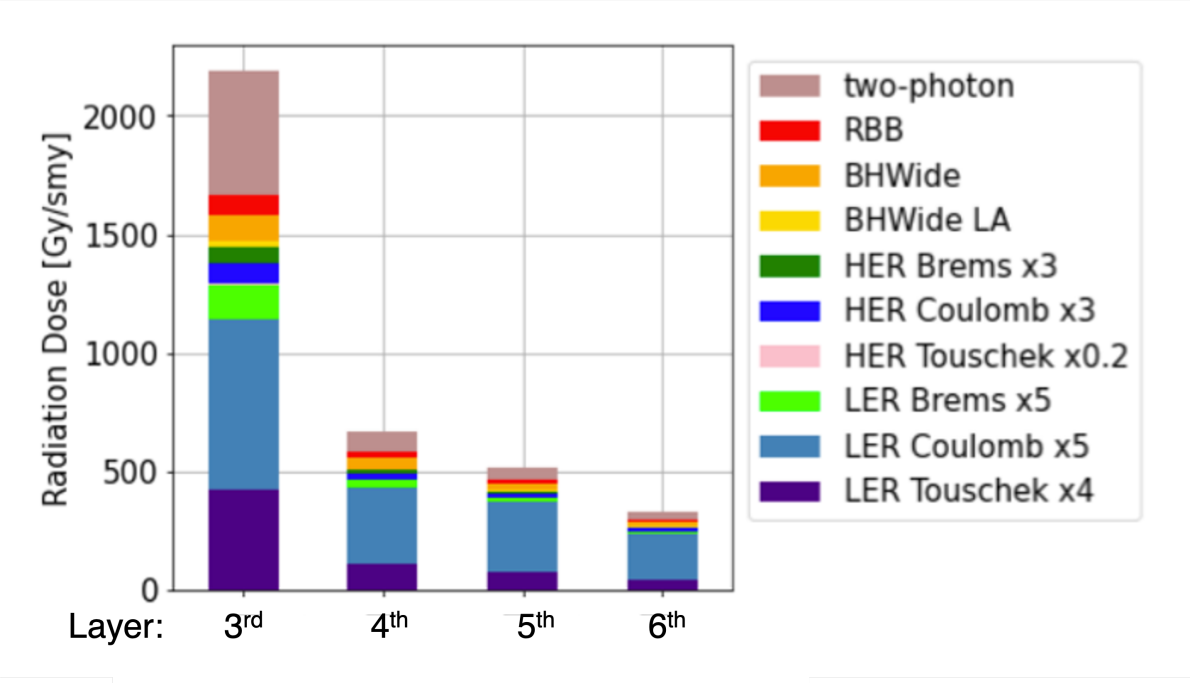

Figure 3.3: The simulation of beam background around the SVD with designed luminosity $\mathcal{L}_{\text{design}} = 8 \times 10^{35}\,\text{cm}^2/\text{s}$, 'RBB', 'RHWide', and 'BHWide LA' are generally included in the Radiative Bhabha scattering and are divided by the scattering angles of an electron θ_e; the 'BHWide LA' is defined as events that $\theta_e \geq 1^\circ$, the 'BHWide' is defined as events that $1 > \theta_e \geq 0.5^\circ$, the 'RBB' is defined as events that $\theta_e < 0.5^\circ$. 'HER' represents the electron beam line side, 'LER' represents the positron beam line side. The coefficients in the figure are correction coefficients obtained by comparing the difference between the MC results and the actual measured values during the same period using the radiation measurement data during actual operation in our past period. [27].

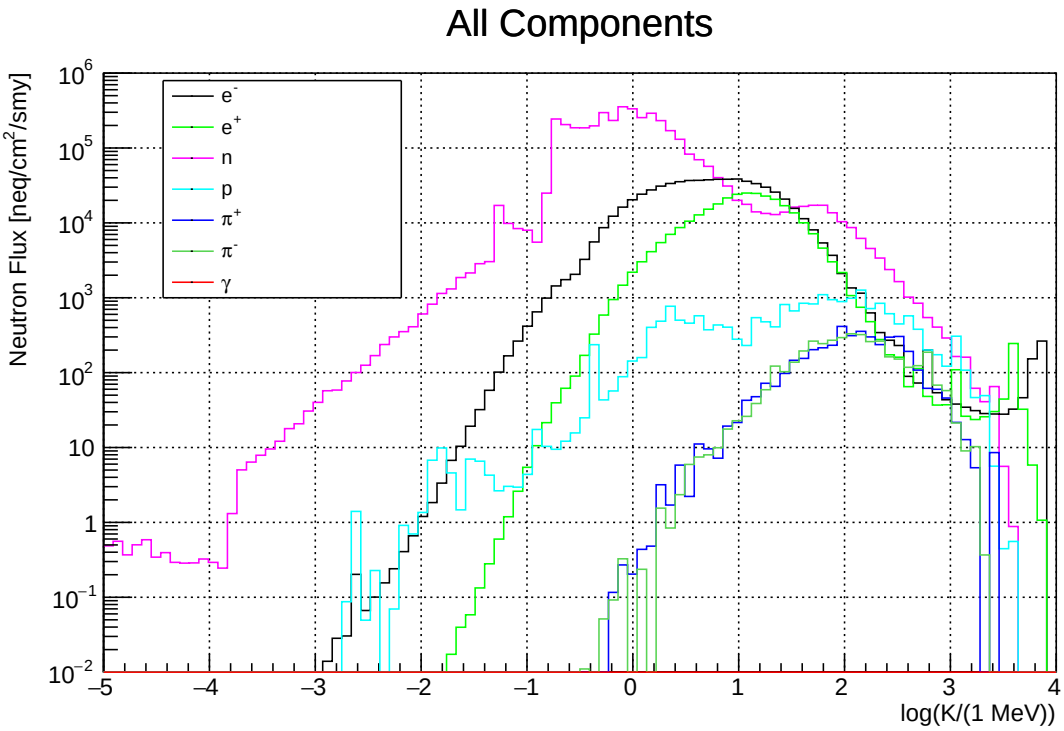

Figure 3.4: Converted neutron flux vs kinetic energy. The vertical axis uses the NIEL factor (below for details, Sec. 3.4), converted to neutron flux, and the damage is evaluated as NIEL damage; damage in the bulk of a sensor bulk. K represents kinetic energy [25]. The distribution of all background elements (two-photon, RBB,...) has a peak at $1 \sim 10\,\mathrm{MeV}$, but only RHWide LA also has a small peak near 10 GeV. The peak around 10 GeV in this figure is the contribution from the electromagnetic shower caused by RHWide LA.

3.3 Woriking principle of double-sided readout silicon strip detector

3.3.1 Silicon semiconductor

Silicon is an atom with four electrons in its outermost shell. It forms crystals by covalently bonding its outermost electrons with other silicon atoms. A pure silicon crystal is an intrinsic semiconductor and does not conduct current easily. By adding a small amount of a pentavalent atom (e.g., phosphorus) to a silicon crystal, one extra electron of phosphorus becomes a carrier and moves through the silicon crystal. This makes it easier for the current to flow. On the other hand, if a small amount of trivalent atom (e.g., boron) is added, one electron pair of silicon that should be filled is not filled, and it becomes a carrier called a hole, which also facilitates current flow. A semiconductor to which a pentavalent atom is added is called an N type semiconductor, and the added pentavalent atom is called a donor. On the other hand, a semiconductor to which trivalent atoms are added is called a P type semiconductor, and the added pentavalent atoms are called acceptors. Fig. 3.5 shows an example of N type silicon semiconductor.

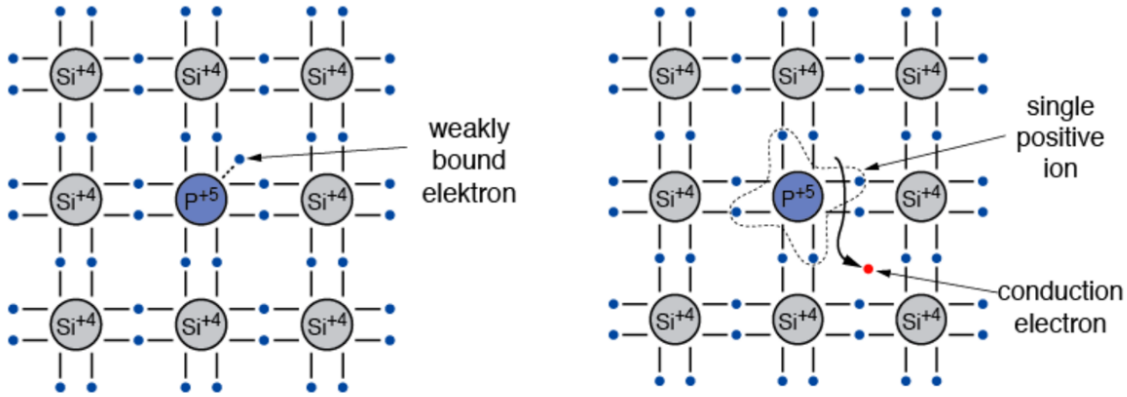

Figure 3.5: Bond model of Phosphorus doped silicon [7]

3.3.2 PN junction

In semiconductors, doped atoms (dopants) create new levels in the band gap. The new level occurs close to the conduction band E_C in P type semiconductors and close to the valence band E_V in N type semiconductors. Carriers in each type of semiconductor can easily transition from the new level to the corresponding immediate band at room temperature. This causes a change in the Fermi level (quasi-Fermi level); the Fermi level of a P type semiconductor drops to near E_V and rises to near E_C at the Fermi level of an N type semiconductor, as shown in the left diagram in Fig. 3.6. When P-type and N-type semiconductors are joined (PN junction), the Fermi levels of the two semiconductors are aligned, and a built-in potential ΔE is spontaneously generated near the junction due to the difference in E_C of the two semiconductors. At this time, the carriers are in thermal equilibrium and no net carrier current exists at the junction. The region where the carriers are in equilibrium is called the depletion layer.

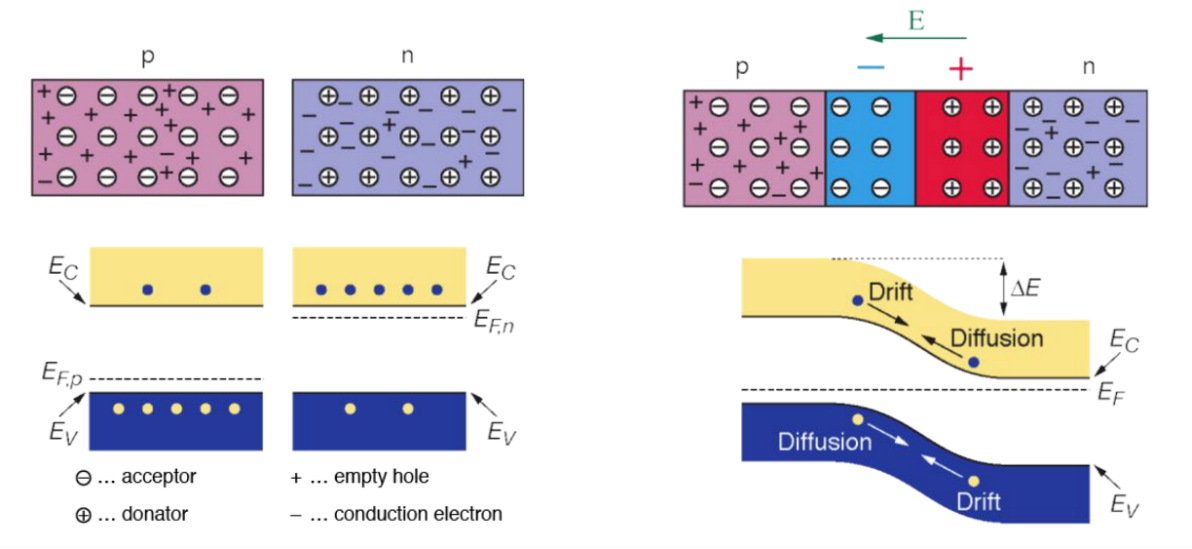

Figure 3.6: Band structure of P type and N type semiconductors (left) and after PN junction (right) [7]

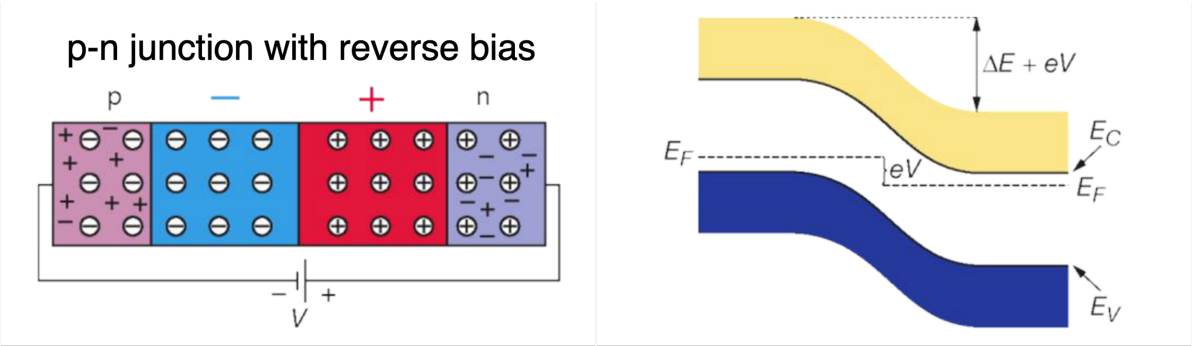

Figure 3.7: Reverse bias [7]

3.3.3 Reverse bias voltage and depletion layer

If a further voltage is applied in the direction of the built-in electric field E in the right diagram of Fig. 3.6, the potential barrier at the junction to the carrier becomes $e(\Delta E + V)$ as shown in the right diagram of Fig. 3.7. Therefore, carrier migration becomes more difficult and very little current occurs in the depletion layer itself. This tiny current is due to electron-hole generation caused by thermal fluctuations in the silicon crystal. For this reason, the current has a temperature T dependence, which is written by the following relation;

$$\frac{I}{I_0} = \left(\frac{T}{T_0}\right)^2 \exp\left[-\frac{1}{2k_B}\left(\frac{E_g(T)}{T} - \frac{E_g(T_0)}{T_0}\right)\right] \quad , \tag{3.4}$$

k_B: Boltzmann constant, $E_g(T)$: energy gap of silicon, $E_g(T) \approx E_g(T_0) \approx 1.12\,\mathrm{eV}$ typically.

In this thesis, the current is called leakage current. Since leakage current leads to noise, DSSD is used for its small leakage current and low noise.

Considering the boundary condition that there is no electric field in the region outside the depletion layer, the depth of the depletion layer widens as the voltage is added to make a

smooth connection of the potential with the region where there is no electric field. the depletion layer width d can be written using the applied reverse bias voltage $V_{\rm bias}$ as the equation [28];

$$d = \sqrt{\frac{2\epsilon_{\rm Si}(\Delta E + V_{\rm bias})}{e} \cdot \frac{N_A + N_D}{N_A N_D}} \propto \sqrt{V_{\rm bias}} \quad , \tag{3.5}$$

N_A: acceptor concentration, N_D: donor concentration, $\epsilon_{\rm Si}$: dielectric constant, e: elementary change.

In the case of our double-sided readout sensor, the P side sensor strip corresponds to the P side semiconductor in the discussion here, and the N type bulk corresponds to the N side semiconductor here. However, the depletion layer spreads in the bulk because the carrier concentration in the P-side sensor strip (N_A) is much higher than that in the bulk (N_D). In addition, the above equation becomes

$$d = \sqrt{\frac{2\epsilon_{\rm Si} V_{\rm bias}}{e N_D}} \propto \sqrt{V_{\rm bias}} \quad , \tag{3.6}$$

basically, the applied reverse bias voltage is much higher than the built-in voltage. The upper limit of d for a typical DSSD is the thickness $d_{\rm sensor}$ of the DSSD, and when $d = d_{\rm sensor}$, the sensor is said to be Full depleted, and the bias voltage at that time is called Full depletion voltage $V_{\rm FD}$.

In this paper, the "reverse bias voltage" will simply be referred to as the "bias voltage".

3.3.4 Signal generation and collection mechanism of DSSD by particles passage

The mean energy required for an electron-hole pair production in silicon is $\epsilon = 3.63\,\mathrm{eV}$. On the other hand, charged particles impart energy $\mathrm{d}E/\mathrm{d}x$ to silicon as they pass through it. Thus, when a charged particle passes through silicon, it produces $\rho_{\rm Si} d_{\rm sensor}(\mathrm{d}E/\mathrm{d}x)/\epsilon$ electron-hole pairs, ρ is silicon density.

A bias voltage is applied to the DSSD when the DSSD is used, and a steady electric field is generated between the P and N side strips. The surrounding steady-state electric field is disturbed by the movement of an electron or a hole generated by charged particles that pass through it. The disturbed electric field is instantly transmitted around the strips near where the electron-hole pairs were generated, and an induced current is generated in those strips, which is processed as a signal by the ASIC (APV25).

Thus, an electric field is required to receive signals from charged particles. Since the electric field is generated only in the depletion layer, DSSD is used by depleting the entire sensor (called full depletion). In addition, charge collection per strip cannot be done correctly because the strips may be electrically connected to each other if the sensor is not fully depleted. This makes it difficult to determine the correct location of particles passing through.

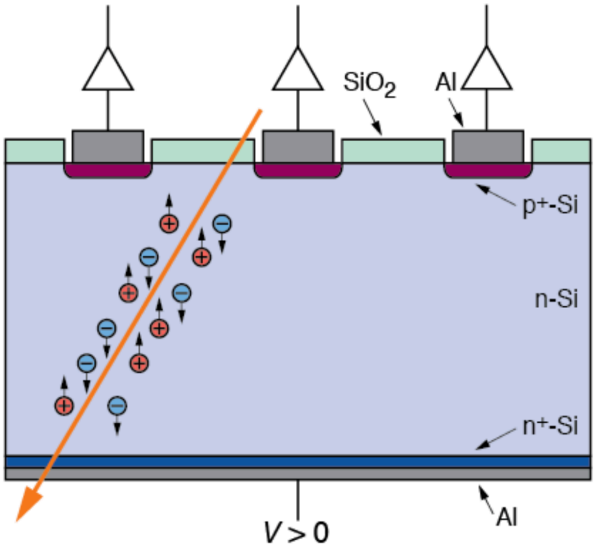

Figure 3.8: Electron hole pair generation in the DSSD by particle passage [7]

3.4 Possible radiation damages of the SVD

The damage caused to SVD silicon sensors by background radiation falls into two main categories; Total Ionizing Dose (TID) and Non-Ionizing Energy Loss (NIEL).

TID : TID is sensor surface damage caused by charged particles (mainly electron, positron, and proton) and photons through ionization. These can cause electron-hole generation within the oxide film (SiO_2), with electrons going to the electrode but holes being transported and captured as a fixed positive charge near the interface between the oxide film and silicon. This creates new levels near the interface (Si-SiO_2) and increases leakage current near the surface, causing interstrip capacitace and other surface properties to change. Fig. 3.9.

NIEL : NIEL is damage inside the silicon sensor (sensor bulk) caused primarily by neutrons or high-energy charged particles. As shown in Fig. 3.10, for a silicon crystal lattice, radiation can bounce off the silicon atoms that form the lattice, creating lattice defects. These defects act as acceptors. In addition to Schottky defects, where silicon is repelled out of the lattice, there are cases where the repelled silicon remains in the lattice, as in the case of Frenkel defects. The excess silicon in the lattice has unpaired electrons, which act as acceptors. This increase in acceptors causes silicon bulk to change from N type to P type. This is called the type inversion.

The NIEL is evaluated in terms of the number of 1 MeV neutrons passing per unit. The amount of damage in various momentum regimes for different particles is compared to the amount caused by 1 MeV neutrons and investigated to obtain a scaling factor to 1 MeV neutrons, these parameters are shown in Fig. 3.11, and Fig. 3.4 was used these parameters on scaling.

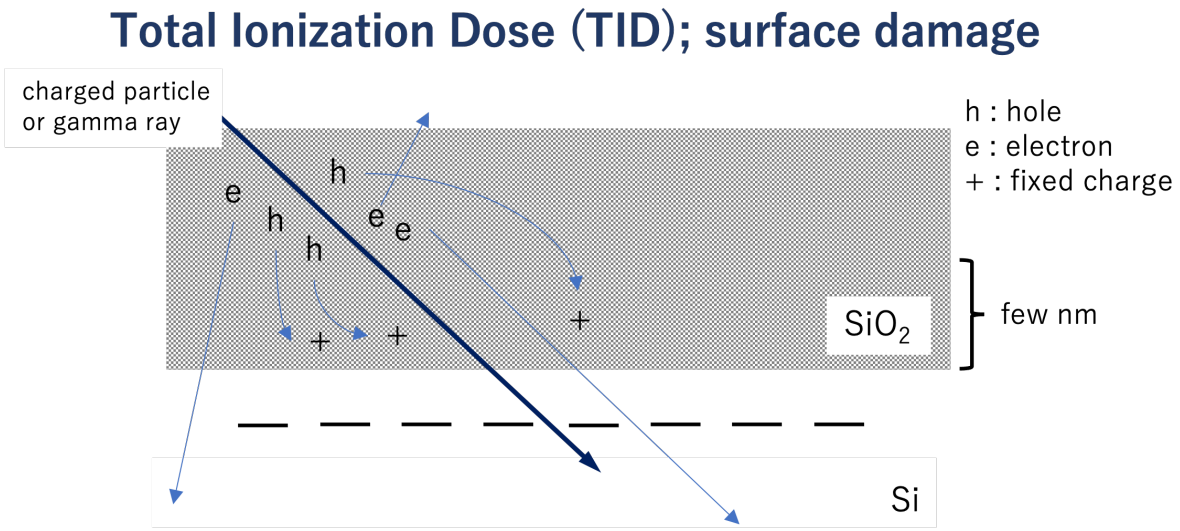

Figure 3.9: The scheme of Total Ionizing Dose

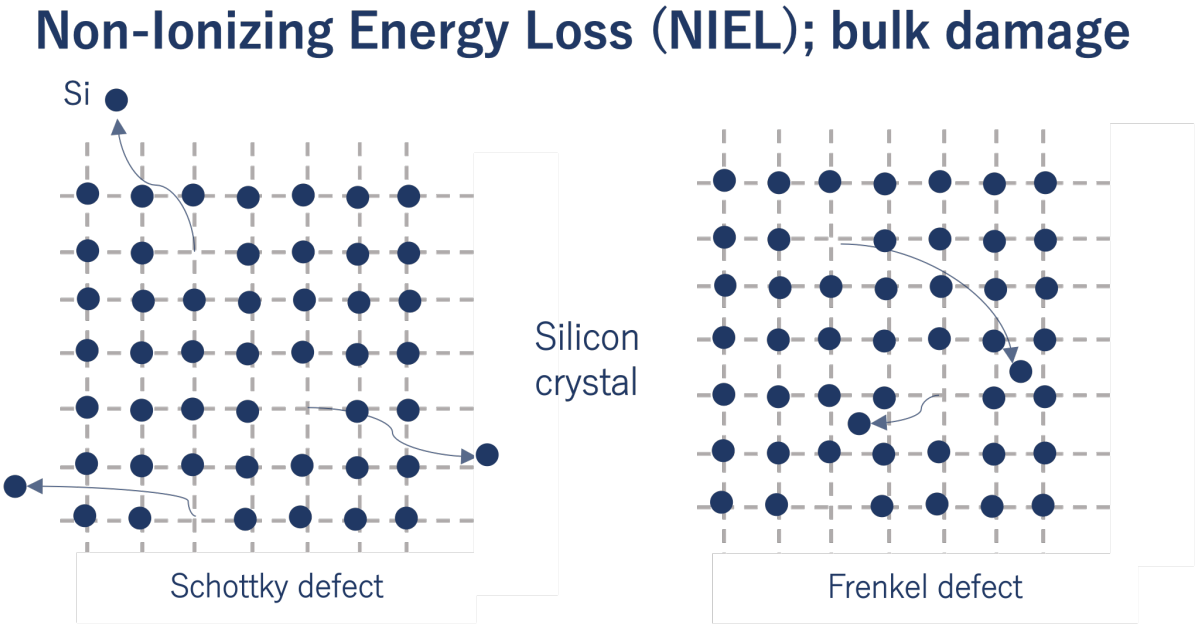

Figure 3.10: The scheme of Non-Ionizing Energy Loss

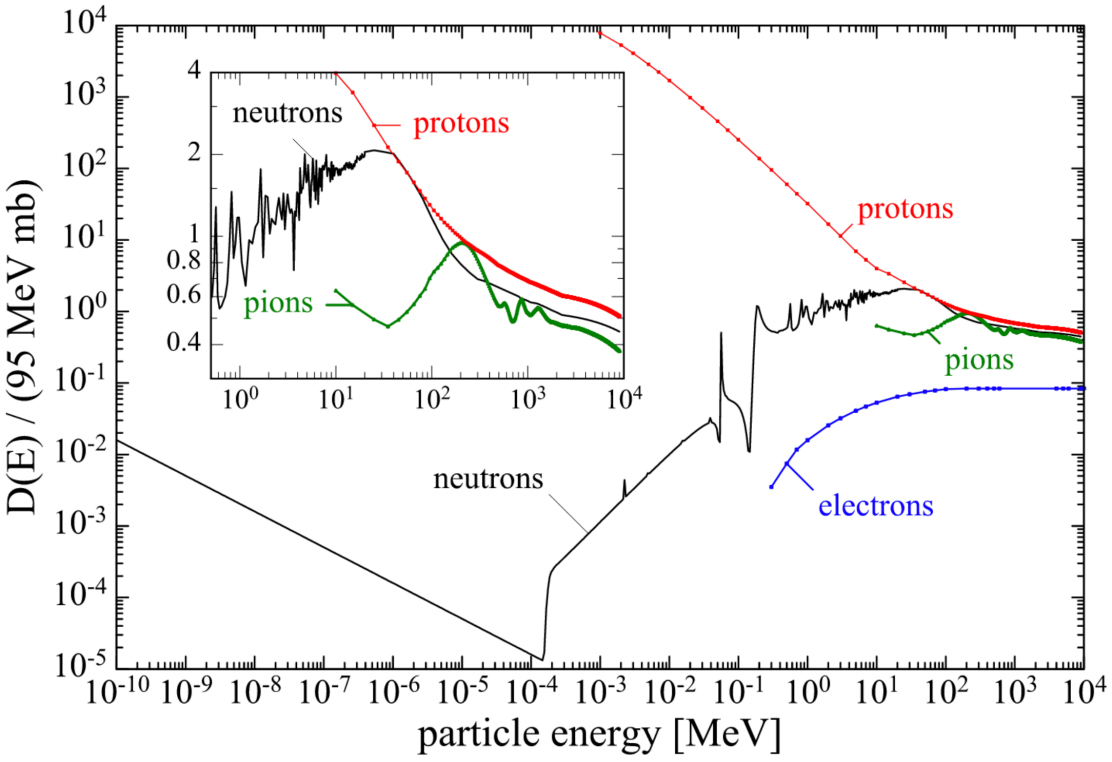

Figure 3.11: NIEL scaling parameter of each particle, $D(1\,\mathrm{MeV}) = 95\,\mathrm{MeVmb}$ [14]

3.5 Operational concerns due to radiation damage

3.5.1 Type inversion and V_{FD} increase after Type inversion

As described in Sec. 3.4, NIEL damage can change the carrier concentration and cause type inversion, in which the N-type bulk changes to the P type. It is necessary to understand the dose that causes such a drastic change in the properties of the bulk. The variation of carrier concentration (charged carrier concentration called effective carrier concentration N_{eff}) with irradiation dose can be considered in the following equation [17];

$$N_{\mathrm{eff}}(\Phi) = N_D \mathrm{e}^{-c\Phi} - \beta\Phi \tag{3.7}$$

where Φ is equivalent neutron fluence, β is rate of the generated acceptors, c is donor removal cross section. The type inversion occurs when N_{eff} decreases due to radiation and becomes 0 and When $N_{\mathrm{eff}} < 0$, the acceptor concentration is more, indicating that the bulk is the P type.

As the carrier concentration changes, V_{FD} also changes. Rewriting Eq.(3.6) for the full depletion, changing N_D to $|N_{\mathrm{eff}}|$, and rearranging for V_{FD} , we obtain

$$V_{\mathrm{FD}}(\Phi) = \frac{e|N_{\mathrm{eff}}(\Phi)|}{2\epsilon_{\mathrm{Si}}} {d_{\mathrm{sensor}}}^2 \quad . \tag{3.8}$$

Fig. 3.12 is an example of V_{FD} behavior. We expect that the V_{FD} we measure will have a structure with the type inversion as shown in the figure.

Based on the above, it is necessary to understand the type inversion and to examine how the V_{FD} rises after type inversion. The way to find out the type inversion is to follow the V_{FD} value for each irradiation dose. And there are two ways to evaluate the V_{FD} .

1. **CV measurement**, The capacitance of DSSD can be calculated as a parallel plate capacitor. Taking the area of the sensor as S_{sensor}, the capacitance C is related to the applied voltage by the following equation;

$$C^{-2} = \left(\epsilon_{\mathrm{Si}}\epsilon_0 \frac{S_{\mathrm{sensor}}}{d}\right)^{-2} = (\epsilon_{\mathrm{Si}}\epsilon_0 S_{\mathrm{sensor}})^{-2} \frac{2\epsilon_{\mathrm{Si}} V_{\mathrm{bias}}}{e|N_{\mathrm{eff}}|} \propto V_{\mathrm{bias}} \tag{3.9}$$

   Capacitance is inversely proportional to the depletion layer width spread. In other words, capacitance works in the region where $V \leq V_{\mathrm{FD}}$, while for $V > V_{\mathrm{FD}}$, the depletion layer does not expand any further, so capacitance remains constant. Thus, we can measure the CV of the sensor and follow the plot of $C^{-2}V$ to consider V_{FD} as the point where the slope of $C^{-}2$ reaches a plateau.

2. **IV measurement**, The leakage current I can be written using the electron-hole pair generate rate U and the depletion layer width, the bias voltage and the following equation

$$I^2 = (eUdS_{\mathrm{sensor}})^2 = (eUS_{\mathrm{sensor}})^2 \frac{2\epsilon_{\mathrm{Si}}(V_{\mathrm{bias}})}{q|N_{\mathrm{eff}}|} \propto V_{\mathrm{bias}} \quad , \tag{3.10}$$

   the leakage current follows this formula until the voltage at which $d < d_{\mathrm{sensor}}$, i.e., $V \leq V_{\mathrm{FD}}$, and then it is expected that the leakage current will not increase. This leakage current is considered only within the sensor bulk, but other currents occur on surfaces and other areas of the actual sensor. However, those currents are small compared to the bulk current, so these current can be ignored and the leakage current behavior of the entire sensor follows Eq. 3.10. This means that we can estimate V_{FD} by making an IV measurement and plotting I^2V, looking for where the slope of I^2V reaches a plateau.

Thus, we estimate the V_{FD} for each irradiation dose through CV and IV measurements. We then look for type inversion based on the structure of V_{FD} by irradiation dose, and estimate the degree of increase in vfd after type inversion.

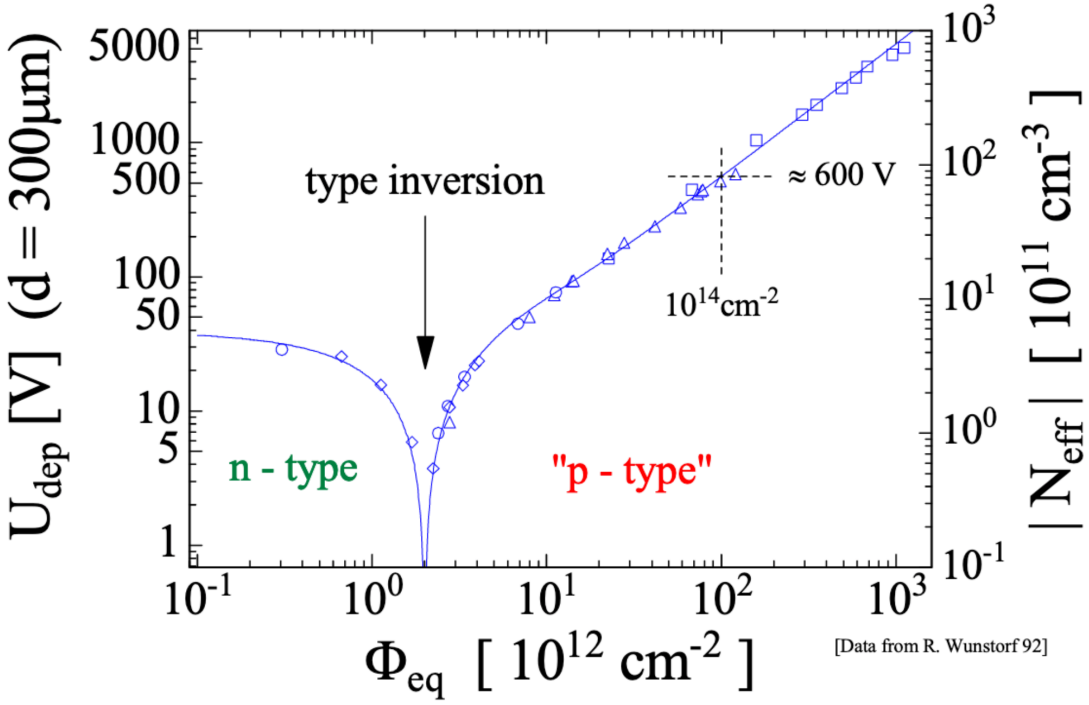

Figure 3.12: A example of V_{FD} change with Type inverison [14], U_{dep} equivalent of our V_{FD}

3.5.2 Leakage current increase

It is known that there is a proportional relationship between leakage current and radiation dose (equivalent neutron fluence Φ) as in the following equation [14].

$$I/v_{\mathrm{sensor}} = \alpha\Phi \tag{3.11}$$

where v_{sensor} is sensor volume, and α is a coefficient that called damage factor.

Increased leakage current leads to increased signal noise. In addition, it may exceed the allowable current range of the power supply module that is providing the bias voltage to the DSSD. For this purpose, we perform IV measurements for each irradiation dose and calculate the damage factor to determine how much the current increases with radiation and up to what irradiation dose our SVD module can withstand.

3.5.3 Noise increase and charge collection efficiency deterioration

The main source of noise in DSSD is the interstrip capacitance of the sensor strip. In our ASIC, APV25, the noise ENC_C is investigated to vary depending on a capacitance C connected to APV25 as follows [20];

$$\mathrm{ENC}_C = 270 + 38 \times C \tag{3.12}$$

Therefore, the increase in interstrip capacitance due to radiation leads to an increase in noise. In fact, interstrip capacitance and the resulting increase in noise on the other group's DSSD have also been reported. [4] with 12 GeV proton beam test.

The change in interstrip capacitance is actually measured by measuring the interstrip capacitance and the applied voltage.

On the other hand, charge collection efficiency (CCE) is also considered to be degraded by radiation. The reason is that if the time required for carriers generated by transit particles to be trapped and re-emitted (detrapping) due to silicon crystal defects caused by radiation damage is longer than the shaping time of the ASIC (50 ns for APV25), the trapped carriers will not become a signal.

Noise and CCE are measured using the SBW module, which is capable of reading out signals connected to DSSD and APV25.

3.5.4 Annealing effect

Thermal vibration of silicon crystals can repair defects in the crystal. This is called the annealing effect. This annealing effect depends on the elapsed time after irradiation and the environmental temperature, and we will investigate how much radiation damage is recovered by the annealing effect by focusing on the change over time of the measurement from Sec. 3.5.1 to Sec. 3.5.3.

Chapter 4

Measurement methods of the irradiation damage in sensor

IV, CV, $C_{int}V$ are useful ways to evaluate the irradiation damage in sensors as described in the previous chapter described. To measure changes in these properties during and after, we develope a remote measurement system for these tests.

4.1 The sensors for the irradiation tests

Three different types of sensors are prepared for the irradiation tests. Their geometries are listed in Tab. 4.1.

Table 4.1: The specification of irradiation sensor samples

	HPK large sensor	HPK mini sensor
thickness [µm]	320	320
sensor area [cm×cm]	12.492×5.964	2.12×2.12
number of strips P side/N side	768/512[*1]	192/192
strip pitch P side/N side [µm]	75/240[*1]	100/100
strip length P side/N side [cm]	12.29/5.772	1.92/1.92
number of irradiated sensor	1	10
irradiated area[*2]	16 mm wide along P strips at center	whole sensor

*1 HPK large sensor has readout strips and non-readout strips (floating strips), the described value of number and pitch are for readout strips only.
*2 Refer to Fig. 4.7

The HPK large sensor and the HPK mini sensor were manufactured from the same silicon wafer provided by Hamamatsu Photonics K.K. (Fig. 4.1). The HPK large sensor is used for the DSSD sensor in the operating SVD modules, thus the properties of the sensor bulk can be expected as the same as the operating DSSD sensor, and the characteristic of the bulk of the HPK mini sensor can be expected to be close to the HPK large sensor due to both cut from the same wafer. On the other hand, the layout of the surface including the strips around the mini sensor is different from the large sensor, this difference would appear in the $C_{int}V$ measurement.

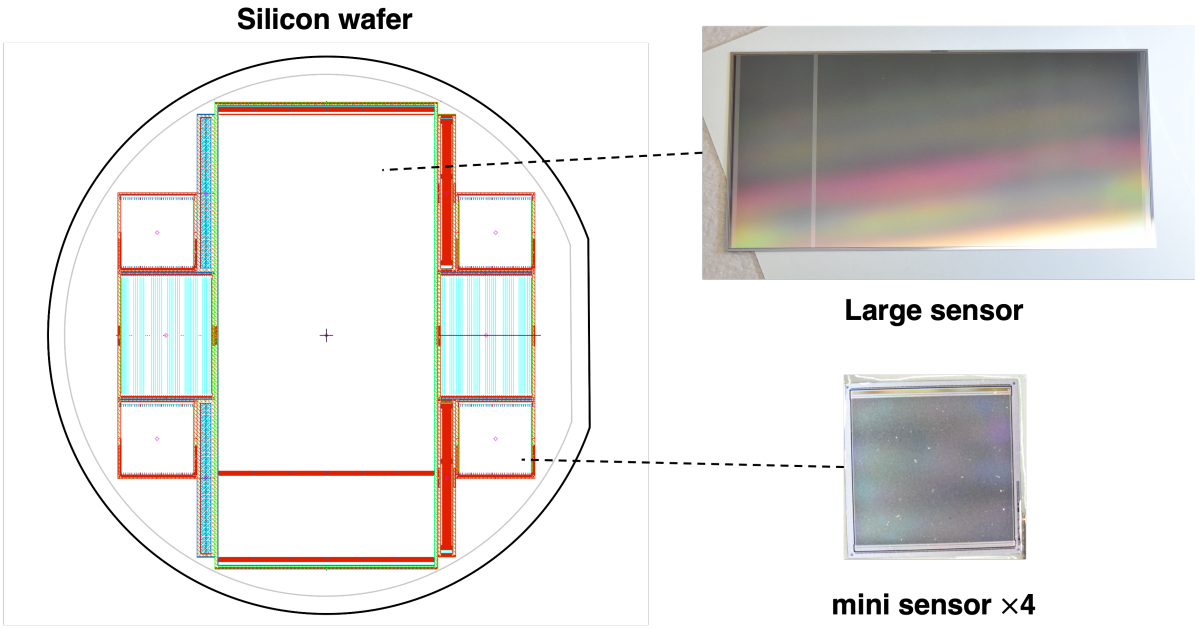

Figure 4.1: The silicon wafer layout. One large sensor and four mini sensors can be taken from a wafer, a large sensor is in the center and four mini sensors are arranged to surround the large sensor.

4.2 Devices and methods of IV, CV, $C_{int}V$ measurement

The used meter of each measurement and conceptual drawings of the connection to the sensor are shown here.

4.2.1 IV measurement

A source meter is able to apply bias voltage to a sensor and measures the leakage current of the sensor at the same time. The positive and negative two terminals are directly connected with the corresponding N (+ terminal) or P (− terminal) side of a sensor. The connection to the sensor is through wire bonding to the bias pad of the N or P side bias ring.

We used the Keithley2614B (Fig. 4.2) source meter for the irradiation tests, it can apply the bias voltage from 0 V up to 200 V and can measure the leakage current range in 0.1 fA to 10 A order. Considering the range of change in leakage current before and after irradiation (expected from nA to mA region), the source meter capability is sufficient. The voltage range is also sufficient because the V_{FD} before irradiation was expected to be around 65 V, and the V_{FD} will be increased proportional to dose, but it will occur after the type inversion in the sensor so that voltage range is sufficient to and confirm the type inversion in the sensor and make sensor bulk full depleted up to a certain high dose after the type inversion.

Figure 4.2: Source meter; Keithley2614B

4.2.2 CV measurement

We used an LCR meter with a protection circuit to measure the bulk capacitance of the sensor. The circuit diagram of the protection circuit is shown in Fig. 4.3. By using this protection circuit, measurements can be made while an external DC power supply provides voltage up to 200 V to the sensor, and it is based on 4-terminal pair (4TP) method that can typically eliminate an ill effect from the probes own resistance or conduct resistance, and can minimize the influence come from measuring current induced magnetic field [23].

We used KeysightE4980AL (Fig. 4.4) as an LCR meter, which has four measuring terminals for 4TP, and the measurement signal amplitude is arbitrarily set to the range of 0 to 2 V_{rms}, the measurement signal frequency range is from 20 Hz to 300 kHz. The source meter to be used for IV measurements is also used for the external DC power supply here.

Regarding those connections, the source meter should be connected to the symbol marked Ex in the fig. 4.3, four terminals marked Hp, Hc, Lp, Lc should be connected to the corresponding LCR meter's terminal, and the sensor should be connected to the symbol of a capacitor marked Cx with wire bonding like the IV measurement.

In addition, To perform measurement more precisely, the so-called OPEN/SHORT correction should be done around the point attached to the sensor before the measurement to reduce the residual impedance of the measurement circuit and adjust the offset on the impedance measurement.

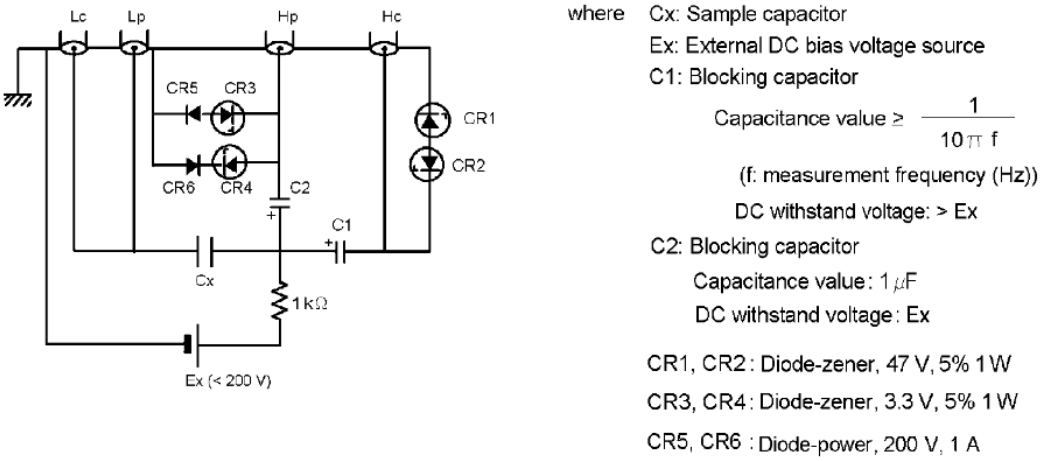

Figure 4.3: 4TP method with external DC bias circuit, in the principal, can be used for measuring frequency up to 2 MHz, external bias voltage up to 200 V [23]. We handmade it. (used a 100 µF electrolytic capacitor for C1)

Figure 4.4: LCR meter; KeysightE4980AL

4.2.3 $C_{int}V$ measurement

The measurement setup of $C_{int}V$ is similar to CV measurement, but in this measurement, the external DC bias power supply (source meter) should be directly connected to the bias ring; remove Ex and 1 kΩ resistor in Fig. 4.3, not needed via the protection circuit because two measurement terminals (Cx in Fig. 4.3) will be connected to the strips, and there are no needs to apply bias voltage.

The $C_{int}$was expected to be small as pF order, hence by measuring the combined capacitance

($> C_{\text{int}}$) consisting of two interstrip capacitances and averaged by dividing by 2 to obtain a more accurate interstrip capacitance. Therefore, we arranged the connection of Cx to strips like Fig. 4.5 and we defined the interstrip capacitance as the value of measured capacitance C_{measured} divided by 2; $C_{\text{int}} \equiv C_{\text{measured}}/2$.

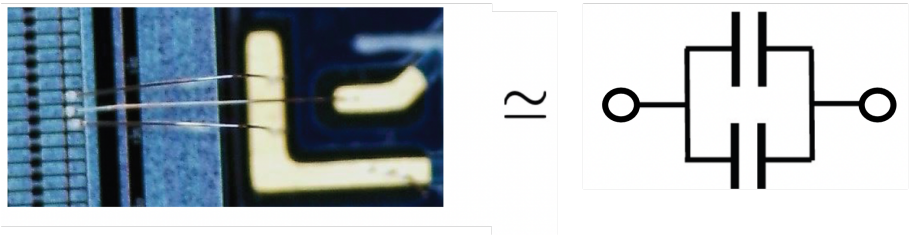

Figure 4.5: Example of the wire bonding for C_{int} measurement, wire bonded on the DC pad of each strip. There are three strips as one pair to measure C_{int}, the center strip and two adjacent strips are connecting different signal terminals via the protection circuit leading to an LCR meter. Thus, the equivalent electrical circuit is two capacitors (two interstrip capacitances) connected in parallel (right figure).

4.3 The configuration of remote measurement system

he system is designed based on the concepts of our remote measurement system are:

- can optionally switch IV, CV, C_{int} measurement circuit
- Minimize the effect come from the devices are irradiated in results except for the sensor
- Can operate the system through the outside of an irradiation chamber

The time available for measurements at the irradiation facility is limited, so users must complete their operations quickly. Our system reduces the time needed for measurement, allowing us to perform measurements between irradiation steps and quickly observe changes in sensor properties just after each irradiation.

4.3.1 Switching board

To satisfy the concepts above, We designed a switching board with a function to switch the circuit between IV, CV, C_{int}V measurement circuits, and all measurement meters were connected to this switching board. To prevent radiation damage from the beam to the board, we decided to create a switching board using an FR-4 PCB substrate, and for the switching function, we decided to use a mechanical relay (SANYU SWITCH Co., Ltd JS-105Z; drive voltage DC 5 V, maximum switching voltage DC 200 V). The detailed design can be found on Sec. 4.6.

4.3.2 Remote control system

What needs to be remotely controlled is the operation of meters (source meter, LCR meter and data logger) and circuit switching. The used source meter and LCR meter, the data logger (GL840) supporting the Virtual Instrument Software Architecture (VISA) which is a used standard in instruments, We utilized the VISA standard to send commands and receive responses to and from the meters via USB communication with PC.

The circuit switching; mechanical relay control was used a digital 5 V output control board (Interface Corporation PEX-234104; open collector sink type, photocoupler output), it had been installed in the PC, and provides a GUI operating screen to control output channels.

4.4 The beam facility and beam condition, dose estimation

The irradiation test was performed using the electron beam facility at ELPH, Tohoku University. The beam configuration is summarized in table. 4.2, The beam current is variable, and we typically operated it at 140 nA. To calculate the irradiation dose in a beam spot per irradiation time D from the beam current I, we used the following relationships;

$$D_{1\text{ electron}} = \frac{(\mathrm{d}E/\mathrm{d}x)\rho d q_e}{S_{\text{beam}}\rho d} = \frac{q_e}{S_{\text{beam}}}\frac{\mathrm{d}E}{\mathrm{d}x}; \tag{4.1}$$

$$D = \frac{I}{q_e} D_{1\text{ electron}} = \frac{I}{S_{\text{beam}}}\frac{\mathrm{d}E}{\mathrm{d}x} \tag{4.2}$$

where $D_{1\text{ electron}}$: dose by one electron, $\mathrm{d}E/\mathrm{d}x$: energy deposit in silicon per length; $1.6\,\mathrm{MeV}/(\mathrm{g/cm^2})$ in minimal ionizing particle energy [26], ρ: density; $2.3\,\mathrm{g/cm^3}$, e: electron charge, S_{beam}: beam spot area on a sensor; measured to be around $1\,\mathrm{mm^2}$. In particular, when the beam current is 140 nA, $D = 2.2\,\mathrm{kGy/s}$

Table 4.2: Beam status

Amplitude	90 MeV
Beam current	140 nA (70 nA)
Beam spot size	$\sim 1\,\mathrm{mm^2}$

In order to cause radiation damage to the entire irradiation area (refer to Table 4.1, Fig. 4.7), we moved the sensor position with two-axis stage (Fig. 4.8) to achieve uniform irradiation on the sensor; the beam sweeps in the irradiation area on the sensor like Fig. 4.6. We use "one routine" which means a single sweep of the entire irradiation area to estimate irradiation dose and time in operation. We adjust the beam sweeping speed to 1 mm/s during 1 routine, This allows an irradiation dose of 2.2 kGy to be given to the entire region in 1 routine when $I = 140\,\mathrm{nA}$, and the irradiated time $t_{\text{irradiation}}$ can be simply calculated as $t_{\text{irradiation}} = D_{\text{target}}/D \times S_{\text{irradiation}}$ from target dose D_{target}, irradiated area $S_{\text{irradiation}}$ (this comes from beam sweep speed 1 mm/s).

Figure 4.6: Beam sweep on a sensor. The red circle represents the beam spot, and the gray square represents a sensor. The beam sweeps on the sensor like a stroke as a red line

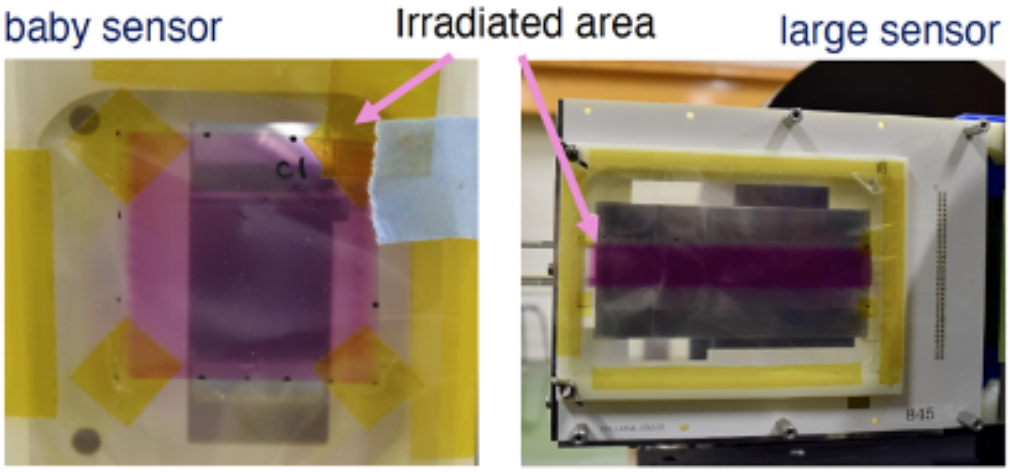

Figure 4.7: Irradiated area; pinkish area, we used radiochromic film to crosscheck the irradiated dose and area. As the irradiated dose increases, the color darkens. The radiation dose survey is currently being requested by a collaborator to a company.

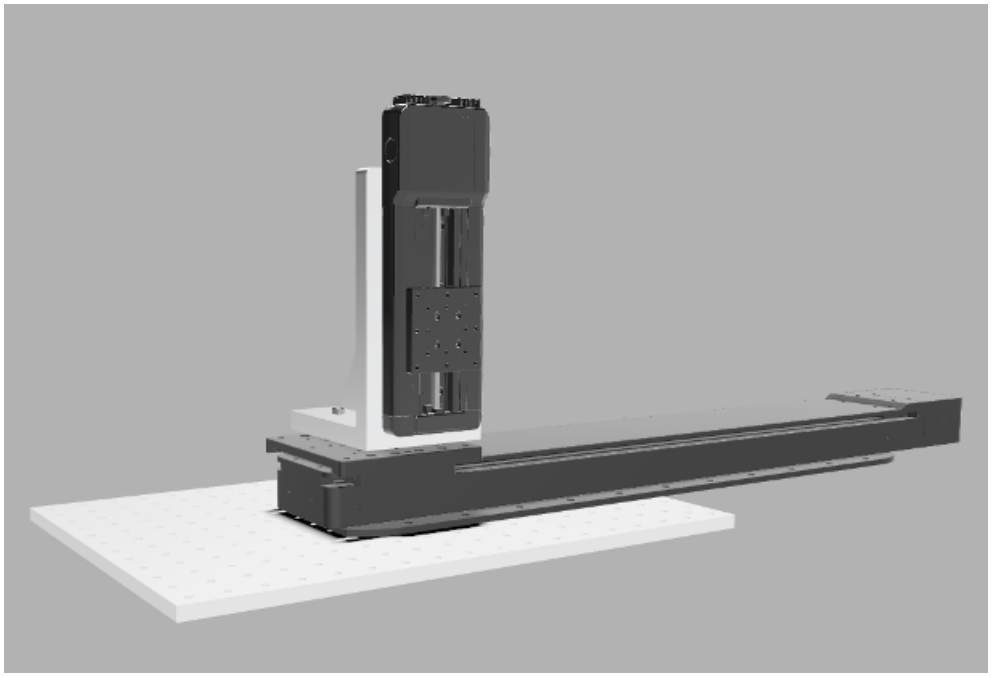

Figure 4.8: The 2-axis stage; consisted from SGSP20-85 (small stage) and OSMS33-500 (larger one) from SIGMAKOKI CO., LTD. An equerre was used to connect them, and the larger stage was fixed on the breadboard which was provided from the facility side. The substrate carrying the sensor is mounted on the smaller stage and moves in a plane perpendicular to the beam. These stages are also can be operated remotely via PC.

4.5 The measurement system placement and radiation shielding

A 2-axis stage was placed on the beamline. As mentioned above, a sensor and a switching board are attached to this 2-axis stage. The switching board is connected to each measurement meter and protection circuit with LEMO cables, and the connection to the data logger and relay power supply is provided by lead wires. The instruments were connected to the operating PC with USB cable.

Since radiation such as electrons and neutrons come from the beamline direction, polyethylene blocks for neutrons and lead blocks and lead sheets for electrons were prepared for shielding. The source meter and other precision instruments were placed in an aluminum-framed enclosure, and the enclosure was shielded with lead and Polyethylene blocks around the beamline direction. The operating PC is located at least 10 m away from the beamline to avoid radiation effects. The PC is connected to another PC outside of the beam radiation hall via a LAN cable and can be operated from outside of the radiation hall.

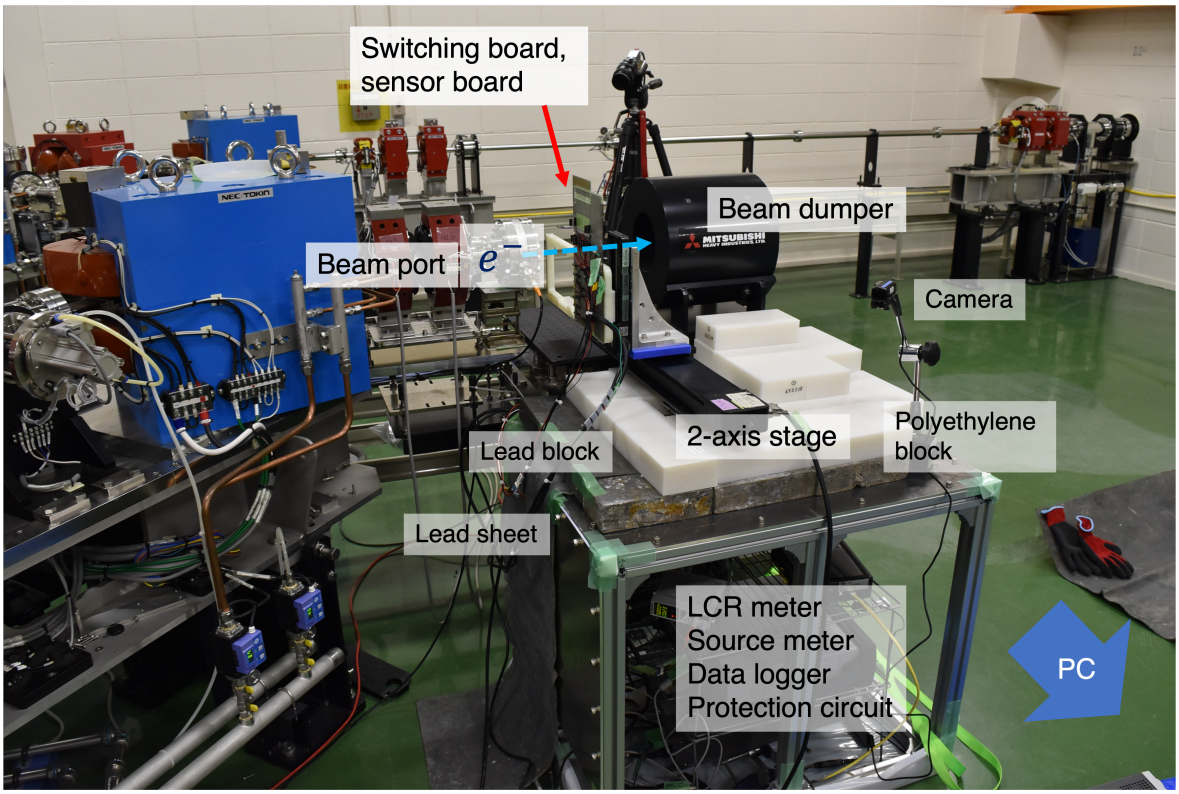

Figure 4.9: The measurement system placement

4.6 The detailed structure around sensor

In the irradiation test, two different types of boards were designed: one for sensor placement and the other for the switching circuits for connecting to measurement instruments. The switching board can be connected to a source meter and an LCR meter, allowing for the switching between IV, CV, and C_{int}measurement circuits. Additionally, both the sensor board and switching board feature MIL connectors, which can be connected to each other through the use of flat cables to complete the measurement circuit. Moreover, multiple sensor boards (up to three in this particular test) were stacked on top of one another to expose the sensors to irradiate like skewered. The first and second layers of sensor boards, when viewed from the beam port, can be connected to the switching board, enabling each sensor to independently measure IV, CV, and $C_{int}$by switching circuits.

A radiochromic film holder is positioned in front of the first layer of sensors and between the first and second layers. A radiochromic film, such as the one shown in Fig. 4.7, is placed in the holder. The film serves as a protective layer for the sensors to protect sensor from accidental touch to the sensor, as well as providing confirmation of the irradiation position and amount. Those boards are fixed to the 2-axis stage by board holders as shown in Fig. 4.10 and move in a plane perpendicular to the electron beam.

Moreover, the environmental temperature is an important input for the measurement, we prepared a Resistance Temperature Detector Pt100 around the sensor, which is connected to a Data logger and uses the fact that resistance changes at a constant rate with temperature to obtain the temperature.

By separating the sensor section and the switching circuit section, the majority of the measurement circuit can be shared, allowing for consistent measurement conditions even when sensors are replaced. Including a MIL connector also allows for quick measurement of different types of sensors, with only minor adjustments to the sensor design required.

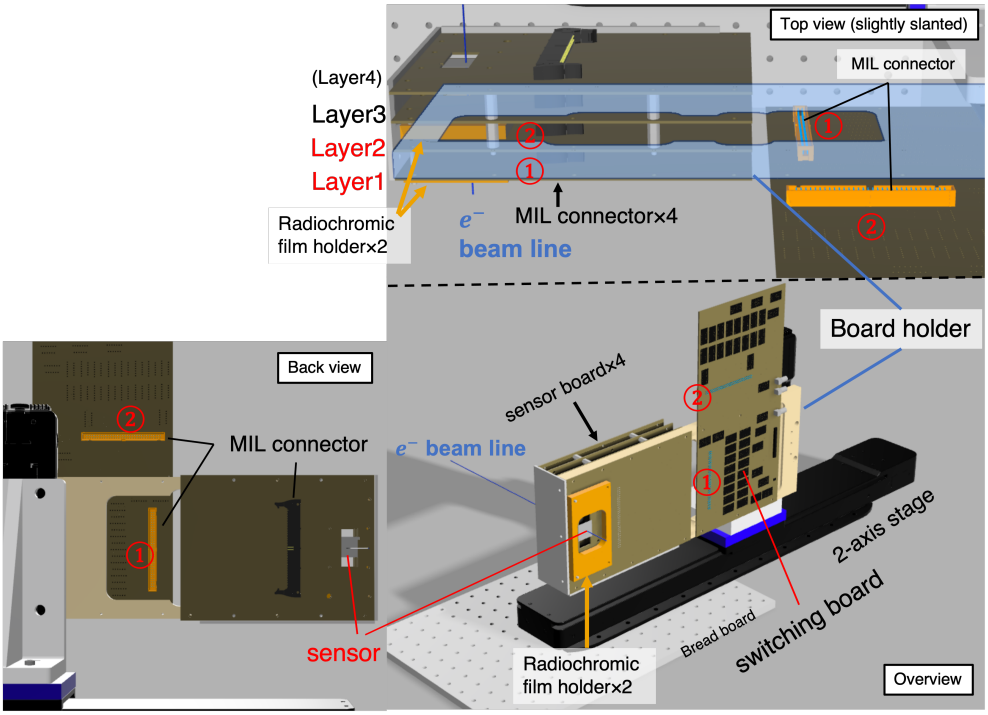

Figure 4.10: The structure around the sensor board and switching board. Each of the two boards ① MIL connectors connect to each other and ② connect to each other with 10 cm ∼ 20 cm MIL cables.

4.6.1 The design of the switching board

The actual switching board is shown in Fig. 4.11.

A source meter and an LCR meter are connected to the corresponding LEMO connectors via LEMO cables. By switching the relays of the switching circuit to IV, CV and $C_{int}V$ measurement circuits, the respective measurements can be performed. C_{int}measurements can be performed for 3 channels for each sensor.

To minimize leakage current and parasitic capacitance caused by the circuit board, we created a circuit using jumper wires on a universal board. Considering the damage to the relay to ensure the reliability of the system, we also included a socket for the relay, allowing it to be easily replaced if necessary.

4.6.2 The design of the sensor board

The board consists of a sensor and a MIL connector, with pads for wire bonding only. The sensor is connected to the MIL connector via wire bonding between the sensor and the pads, allowing for measurements to be taken.

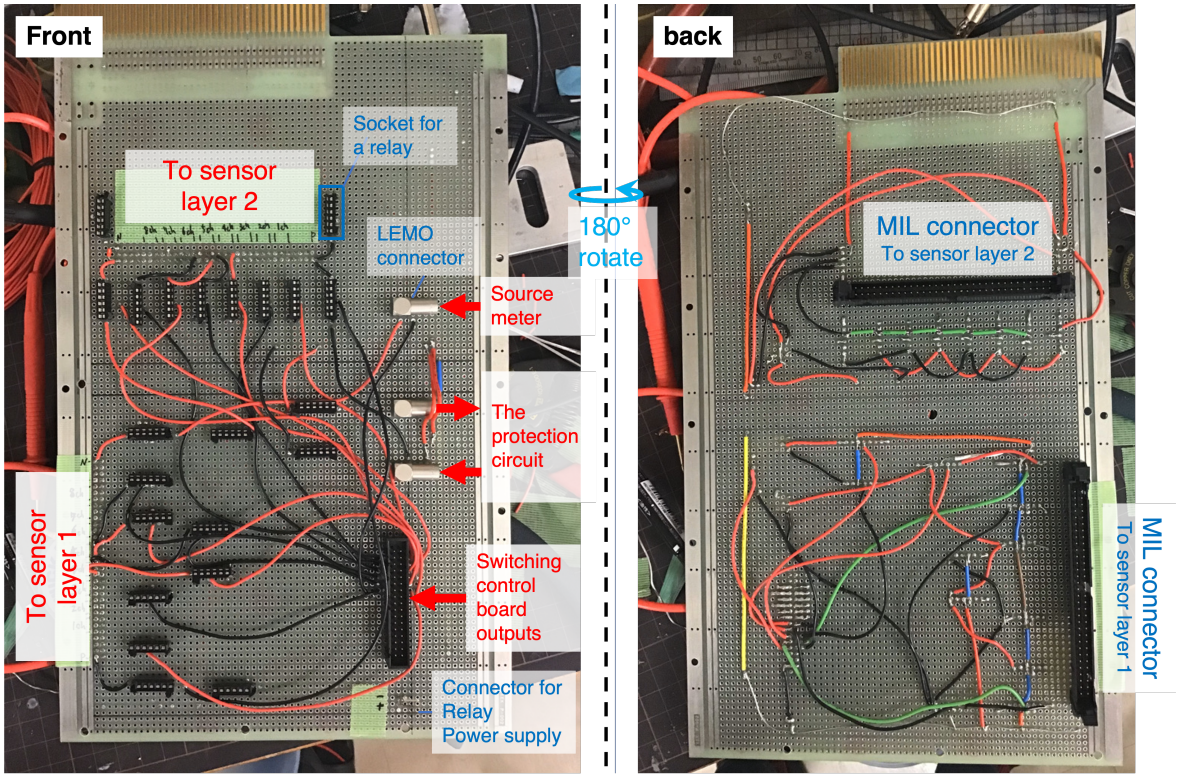

Figure 4.11: The designed switching board for the test.

Fig. 4.12 is for a large sensor, but the only difference is the geometry, and the other kind of sensors are based on a similar design. An epoxy adhesive Araldite 2011*, which has a proven track record of radiation tolerance, was used as the adhesive for bonding the sensors. The substrate behind the sensor was cut, leaving a tiny adhesive area.

*If the adhesive adheres to the pad on the sensor board, it cannot be bonded to that pad, so it is necessary to cover the pads with masking tape when attaching the sensor.

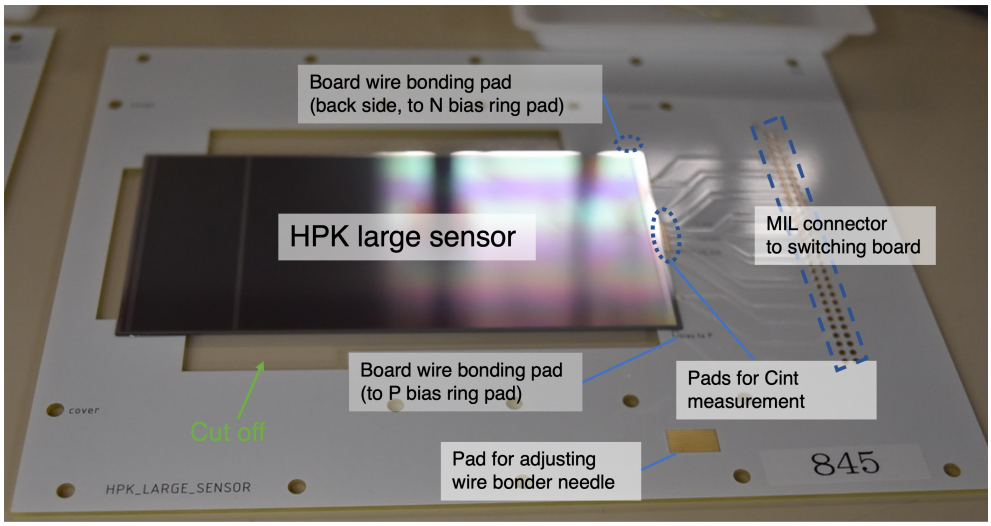

Figure 4.12: An example of the sensor board.

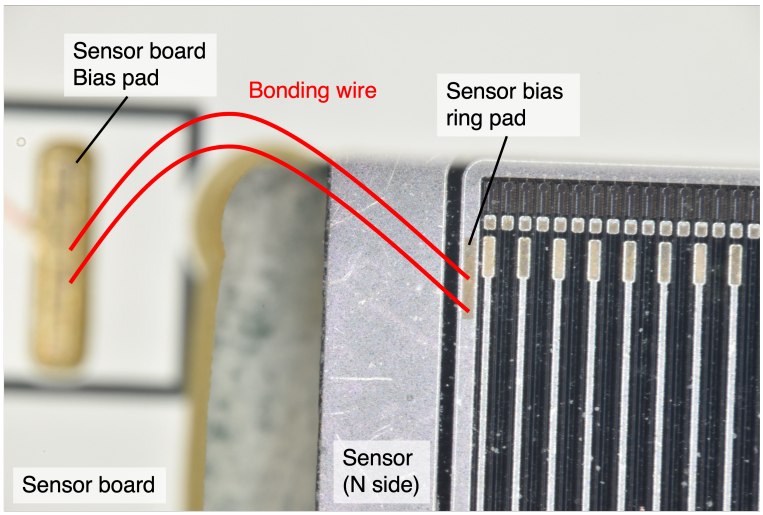

Figure 4.13: Wire bonding (aluminum) to bias pad. The Pad on the board is made of electroless nickel immersion gold (ENIG) as a material for wire bonding. It is known that the success rate of wire bonding will be much decreased when gold is not included in.

4.7 Annealing effect measurement

Annealing is a process that occurs after irradiation. We investigated the annealing effect over time after irradiation. The study will be evaluated by looking at changes over time in IV, CV, and $C_{int}V$ values.

The annealing effect is influenced by the sensor temperature (Since there is no substance near the sensor that can be a heat source this time, the environmental temperature near the sensor should be investigated.), so we needed to monitor the temperature changes in the environment where the sensors were stored. To do this, we use two types of thermometers shown in Fig. 4.14

Figure 4.14: Thermometer for checking environment temperature around sensor: Pt100 (left), TR-76Ui by T&D Corporation (right)

Fig. 4.15 shows the temperature and elapsed time since just after irradiation. The sensors were stored at ELPH until August 17th, 2022, and then transported by car to KEK Tsukuba experiment hall on the day. The sensors were stored at temperatures ranging from $17 \sim 20\,^{\circ}\mathrm{C}$ at ELPH and $23 \sim 27\,^{\circ}\mathrm{C}$ at KEK. IV, CV, and cint measurements were performed at the time corresponding to the green vertical line in the figure. For the annealing measurement, the switching board, the sensor board, each measurement meter, and the control PC, which constitute the measurement circuit used in the irradiation test, are used. A lightproof box is used to shield the sensors from light.

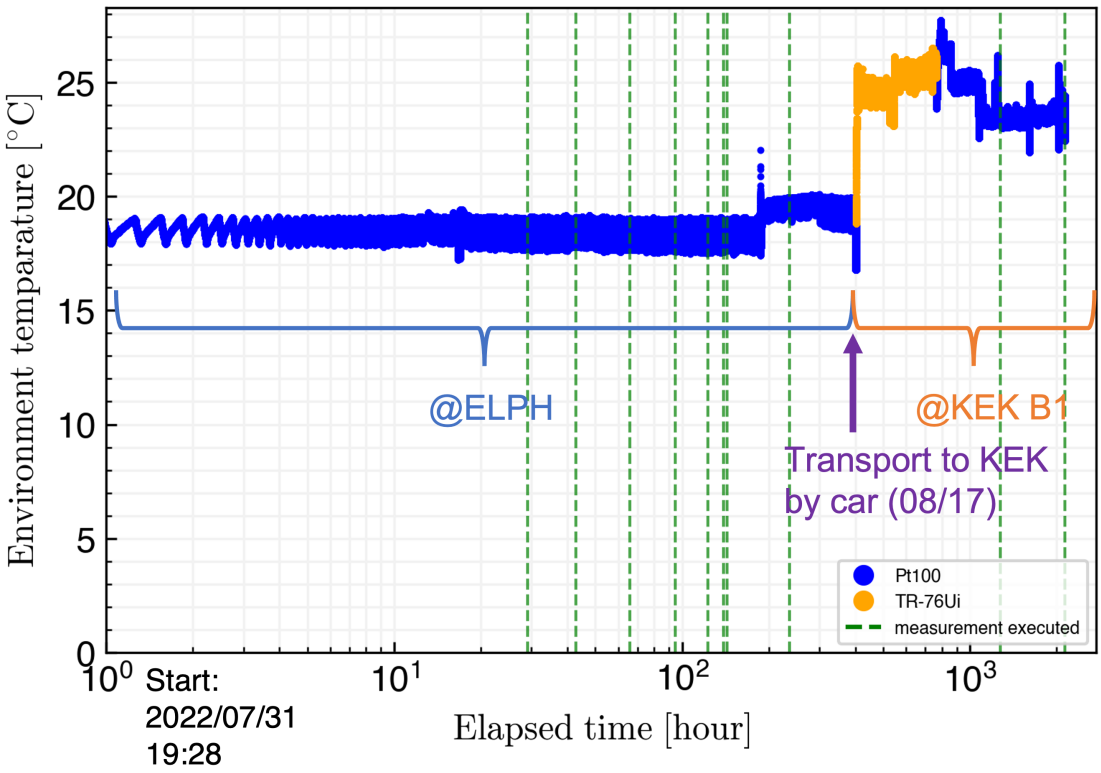

Figure 4.15: Envioment temperature changes in annealing process

Chapter 5

The results of the irradiation tests

5.1 Beam current

As described in Sec. 4.4, the irradiation dose is calculated from the beam current. The current value of the beam is monitored (an example: Fig. 5.1) by the facility and is used in our calculation. The current values were obtained without any problems during the entire irradiation period.

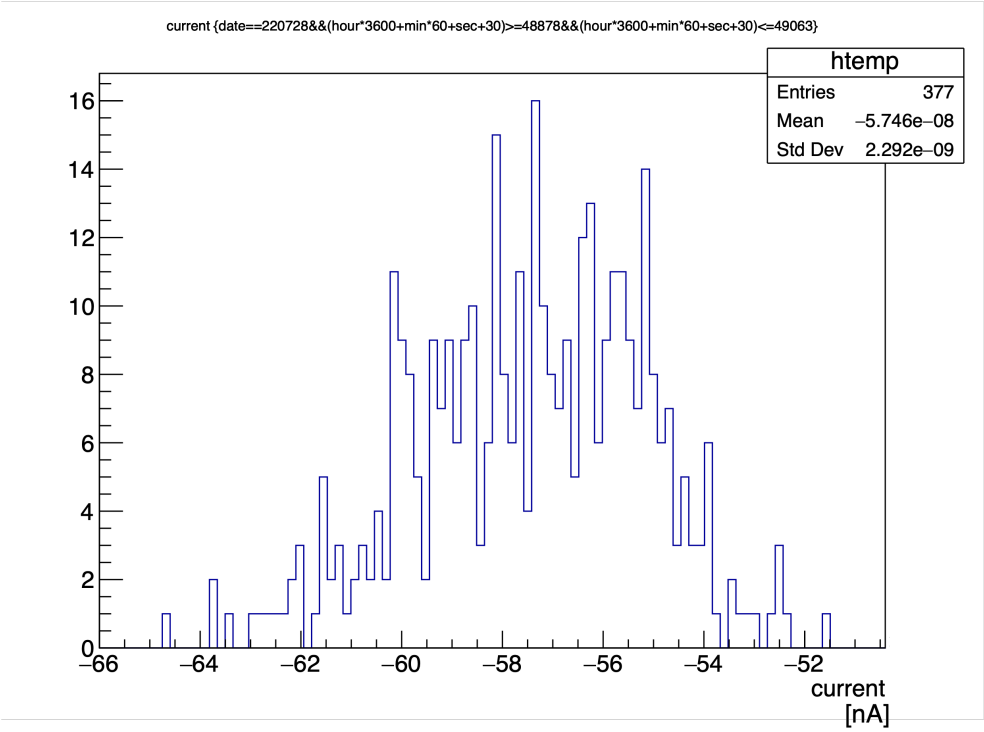

Figure 5.1: An example histogram of beam current during an irradiation period provided by the beam facility side. The unit of the horizontal axis is Ampere.

5.2 The results of the irradiation test

Irradiated dose on sensors

Fig. 5.2 shows the relationship between the irradiated sample and the irradiation dose to the sensor calculated from the current values using the method of Sec. 4.4. In the figure, the dots represent the doses at which IV, CV, and (C_{int} V) measurements were taken. The star symbol and accompanying number denote the dose at the end of the irradiation. At this irradiation test, 10 samples of HPK mini sensor and 1 HPK large sensor were irradiated.

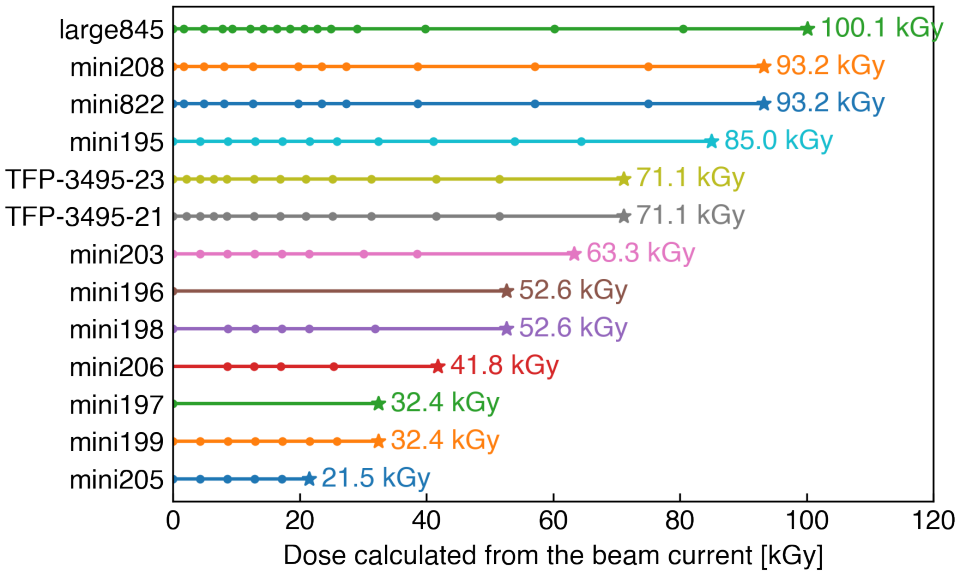

Figure 5.2: The samples with irradiated dose. In the vertical axis labels, 'mini' represents the HPK mini sensor, and 'large' represents HPK large sensor. The number beside it is the serial number of a sensor to identify.

In order to investigate annealing effects occurring in sensors with different irradiation doses, the different dose at the end of irradiation was intentionally chosen for each sensor.

5.2.1 The results of IV, CV, C_{int}V measurement of mini sensor

The results of the IV, CV, and C_{int} V measurements are presented here. The results are shown here for each irradiation dose of mini822 as a representative example of mini sensors, where the results of the other mini sensors show similar behavior.

The mini sensor has a different surface strip structure from the SVD sensor currently in operation, which makes it difficult to directly feedback with the information obtained from the mini sensor's C_{int} V measurement into the SVD operation. As a result, the number of C_{int} V measurements taken with the mini sensor was reduced and used for irradiation time instead.

The results are shown from Fig. 5.3 to Fig. 5.6. The order from the top to the bottom is IV, CV, and C_{int}V measurements, and to find the V_{FD} , we plotted in I^2V for IV and C^2V for CV. On the other hand, as mentioned in Sec. 4.2.3, the C_{int} is the measured value divided by 2. The plot shows 'NO DATA' for dose steps where C_{int}V measurement was not performed. The Dose where the measurement was performed is displayed above each plot.

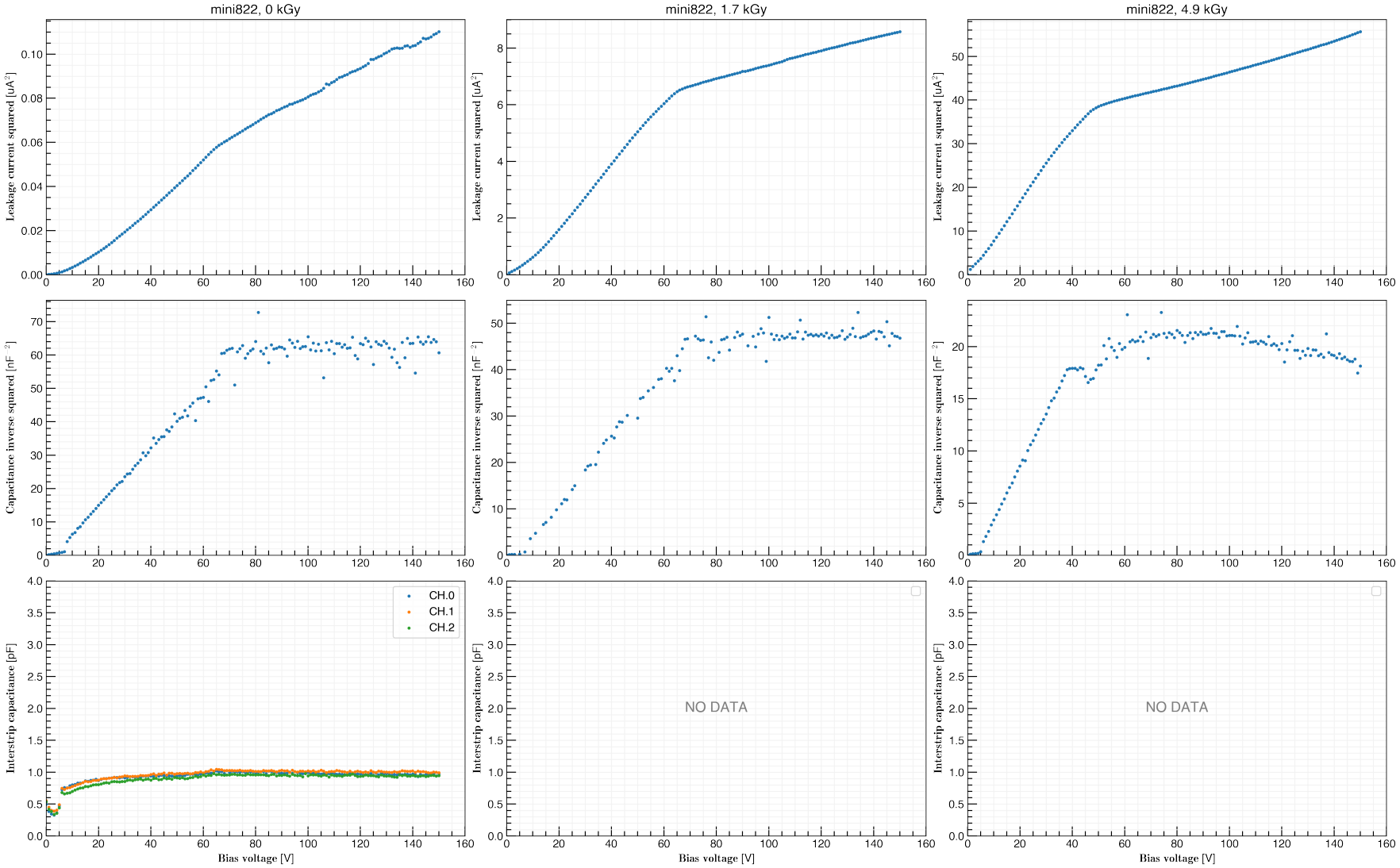

Figure 5.3: The IV, CV, $C_{int}V$ results of mini822 0 kGy $\sim$ 5.1 kGy

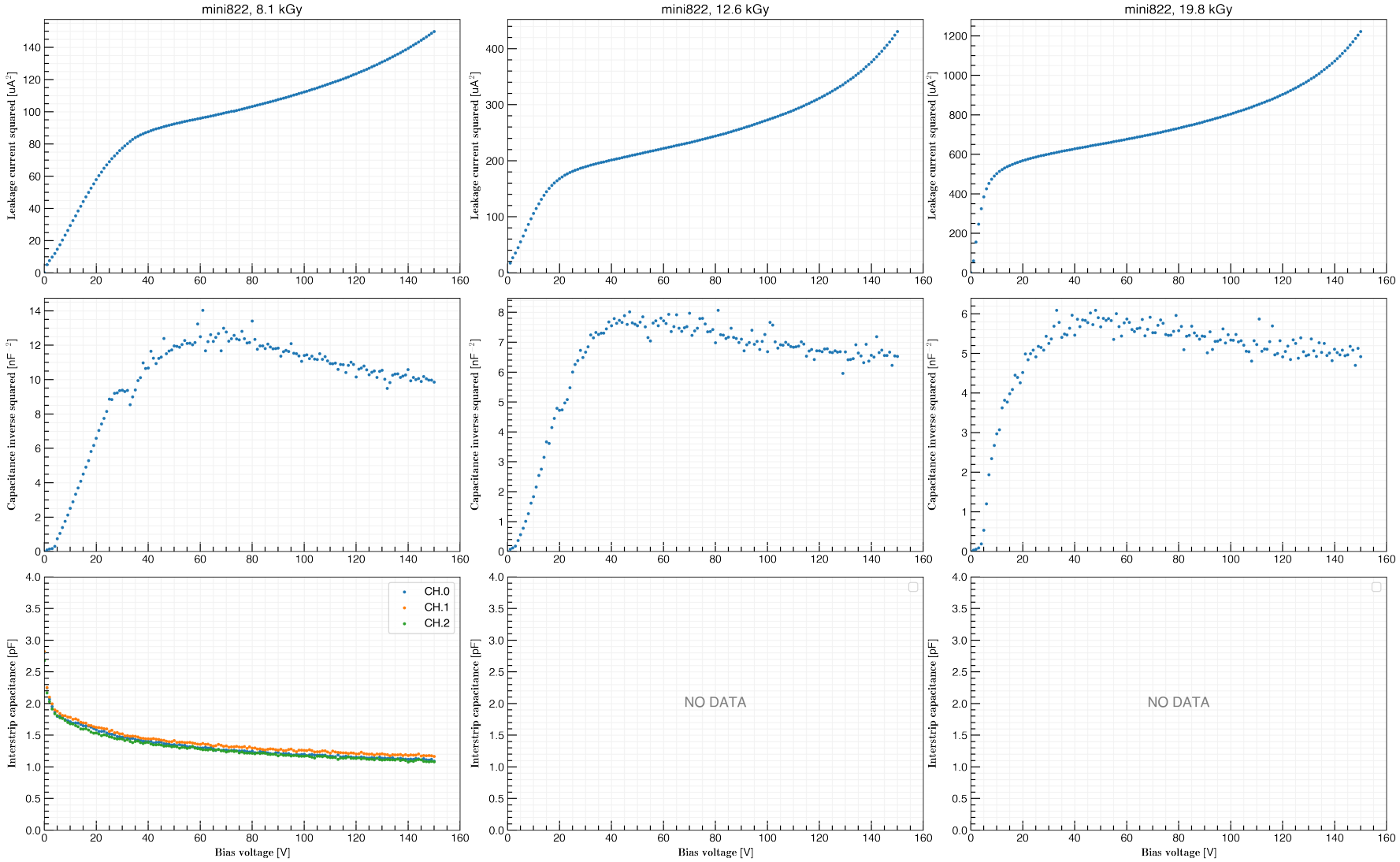

Figure 5.4: The IV, CV, $C_{int}V$ results of mini822 8.5 kGy $\sim$ 21.2 kGy

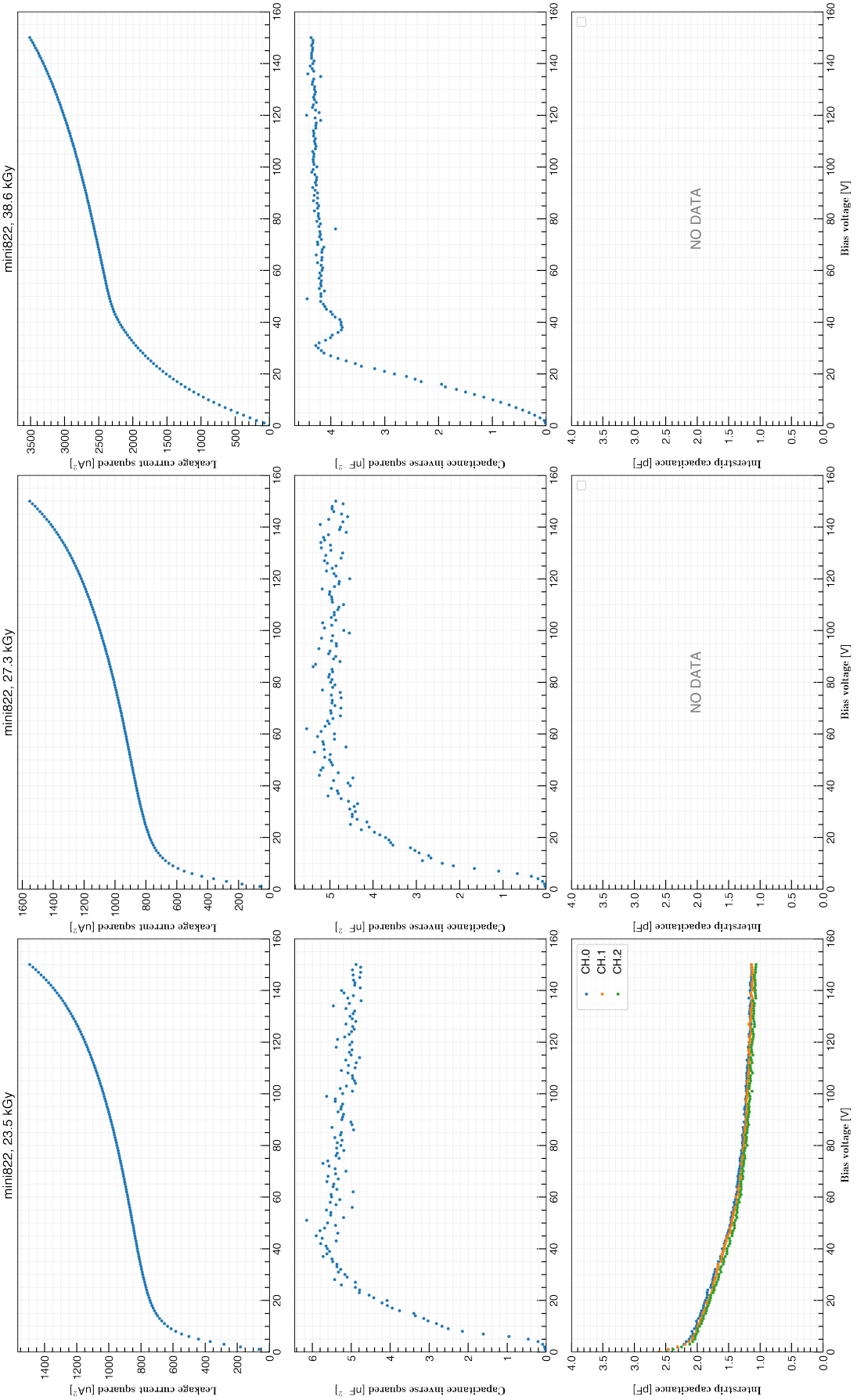

Figure 5.5: The IV, CV, C_{int} V results of mini822 25 kGy $\sim$ 40 kGy

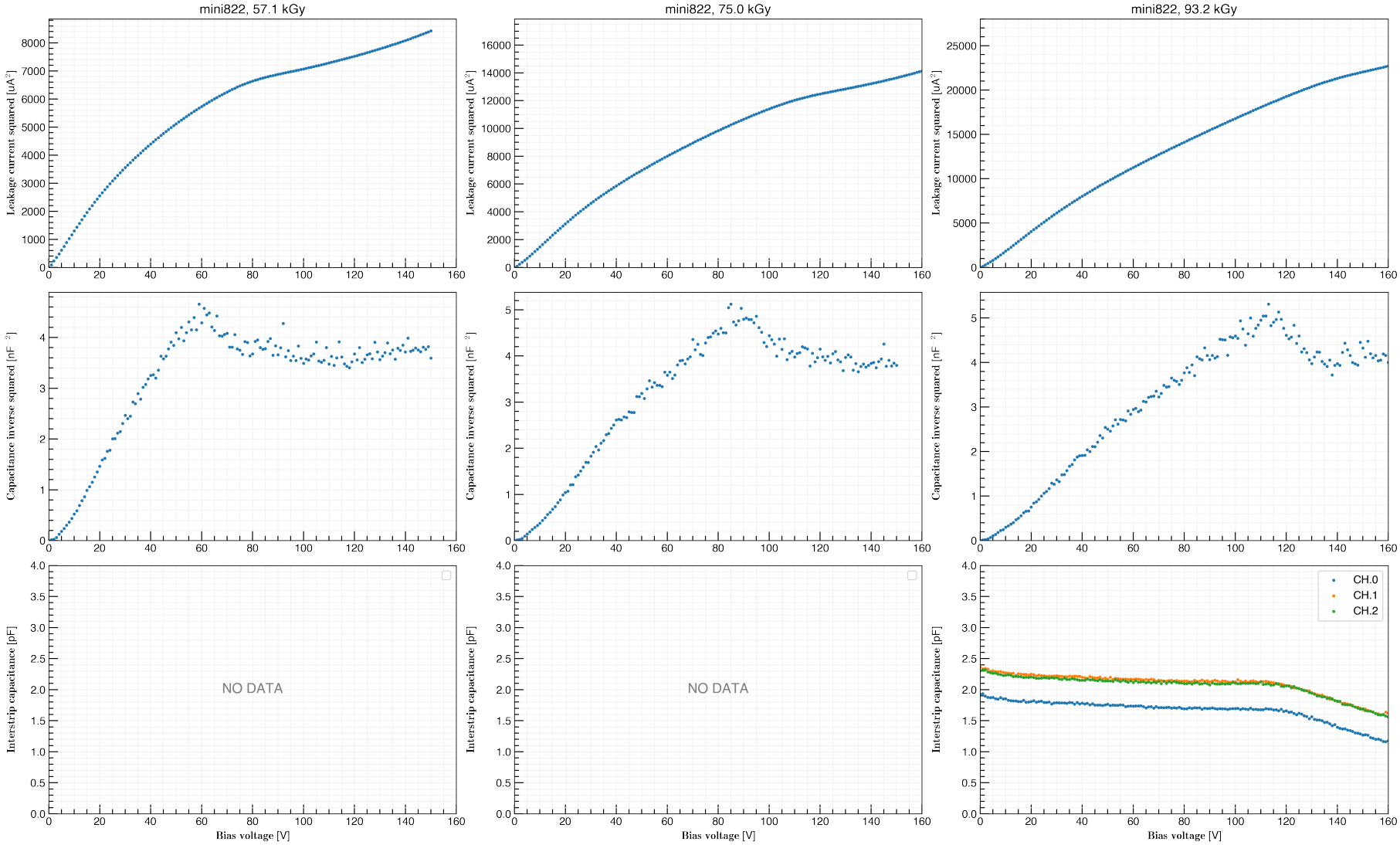

Figure 5.6: The IV, CV, $C_{int}V$ results of mini822 60 kGy $\sim$ 100 kGy

IV measurement summary

From the plots, A shoulder shape can be seen clearly on the I^2V curve (Henceforth referred to as IV curve) in the irradiation dose range from 1.7 kGy to 60 kGy. At 0 kGy, Observing the shoulder accurately is difficult because slight leakage currents ($\approx$ 100 nA) from external sources (most likely due to the switching board) have contaminated the measurement. However, a point can be identified at which the slope of IV curve changes around 65 V. The same CV measurement of 0 kGy shows a plateau from around 65 V Thus at 0 kGy measurement, the absolute values of the measurements are unreliable, but we can roughly estimate that the V_{FD} is around 65 V; Locating the V_{FD} is not an issue.

On the other hand, it is known that the leakage current of the sensor increases along with the increase of the irradiation dose, and this is supported by our results. While external leakage current was a problem at 0 kGy, it is thought that the external leakage current does not significantly increase with increasing irradiation dose because the rest of the sensor area is never irradiated. Therefore, the external leakage current is expected to be at most approximately 100 nA, which is a small fraction (around 2%) of the shoulder current value at 1.7 kGy irradiation. This value is considered to be insignificant, and even more so for measurements at higher irradiation dose steps.

The position of the shoulder of the IV curve shifts towards lower voltage with increasing irradiation dose up to 20 kGy, but beyond that point, it turns to shift towards higher voltage, To better visualize the changes in the shoulder's position, Fig. 5.7 shows each measurement scaled by the maximum value of the measurement. This behavior can be considered as a change in V_{FD} . From here it means that with this measurement we were able to confirm the type inversion, a detailed analysis will be given later.

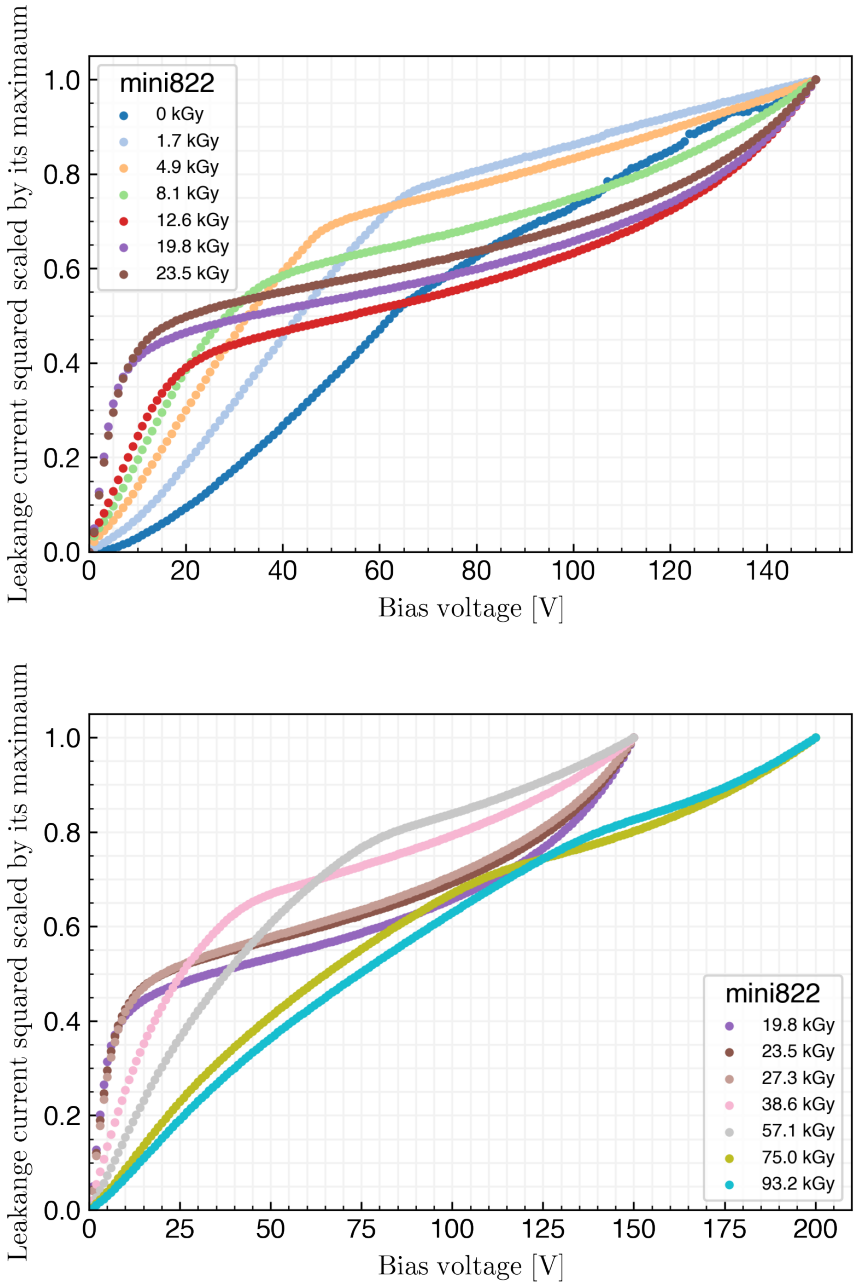

Figure 5.7: IV curves scaled by its maximum value. The unit of vertical axes is [arbitrary unit]. above: 0 kGy $\sim$ 23.5 kGy, below: 19.8 kGy $\sim$ 93.2 kGy. Only for 75.0 kGy and 93.2 kGy, data were taken up to 200 V of applied voltage because the shoulder of IV curves are at higher voltages. In the figure above, we can see the shoulder shifting more and more to the left until 19.8 kGy, In the lower figure, the shoulder appears to shift more and more to the right as the irradiation dose increases from 19.8 kGy.

CV measurement summary

Measurement frequency of LCR meter was set to 1 kHz and signal amplitude is 0.1 V.

The $C^{-2}V$ curve () is expected that the capacitance would be like as $C^{-2} \propto V$ before V_{FD} and then plateau. This trend is visible for 0 kGy and 1.7 kGy in this result Fig. 5.3, however, other irradiation doses show bulging in areas that were expected to be linear. Thus, we hard to find out the V_{FD} from the CV curve, the V_{FD} is expected to be a point that separates the two areas in the CV curve, but we can confirm that the angle between the rising edge of the CV curve and the horizontal axis tends to increase in proportion to the irradiation dose and decreases after a certain irradiation dose. This trend is consistent with that observed in the IV measurement.

$\mathbf{C_{int}}$V measurement summary

Measurement frequency of LCR meter was set to 100 kHz and signal amplitude is 0.1 V.

Basically, the structure around the strip surface of the mini sensor is different from that of the current SVD or HPK large sensor, so it is not possible to provide direct feedback from the C_{int} V measurement of the mini sensor, but we would like to see how it changes before and after the type inversion.

C_{int} V results were summarized in Fig. 5.8, we can confirm the C_{int}increases overall voltage region; near 0V after irradiation is nearly 2.3 pF, but can be reduced by about 1 pF when a bias voltage is applied beyond V_{FD} (star symbol in the figure), which is evaluated from the IV curve described below.

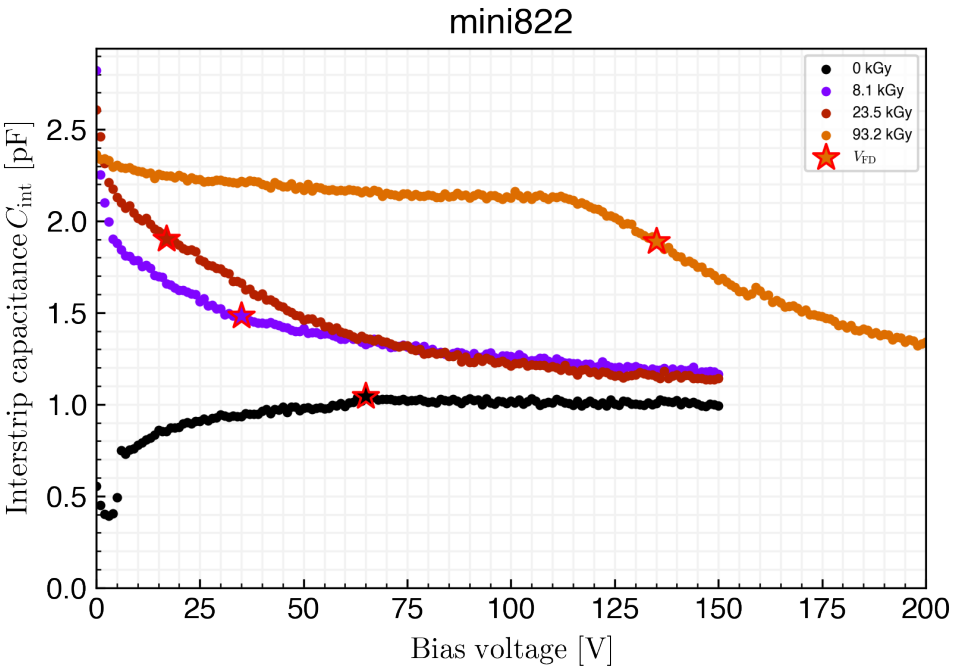

Figure 5.8: C_{int}V changes, 1 channel is picked up

5.2.2 The results of IV, CV, $C_{int}V$ measurement of HPK large sensor

The results of IV, CV, $C_{int}V$ of the HPK large sensor (large845) are shown here as the mini sensor results. It is important to note here that unlike the mini sensor, which was irradiated over its entire surface, the irradiated area for the HPK large sensor was limited to a 16 mm wide area along the Pstrip at the center of the sensor as shown in Fig. 4.7, thus it is possible that type inversion not occur in the non-irradiated areas of the HPK large sensor.

5.2.3 IV measurements

The change in the position of the shoulder (V_{FD}) of the IV curve and the increase in leakage current with irradiation dose like a mini sensor can be confirmed. However, the leakage current of the large sensor is larger than that of the mini sensor due to its larger area.

5.2.4 CV measurements

The $C_{int}V$ measurement were performed with the same settings as for the mini sensor. We summarized the results of CV measurements in Fig. 5.9. According to the figure, C^{-2} decreases as the irradiation dose increases. This indicates that C is increasing. However, the shoulders of the CV curves for 0 kGy and 1.7 kGy were around 50 V. As the irradiation dose increased, a peak appeared in that location. The position of the peak shifts slightly to the lower voltage side with increasing irradiation dose, but the overall location remains largely unchanged.

Based on the information provided, we can conclude that the HPK large sensor has difficulty in accurately estimating V_{FD} (voltage-for-discharge) using CV measurement. We speculate that this is due to the fact that the irradiated and non-irradiated regions are on the same sensor, and that the different behaviors of the two regions are mixed, and it appears on the results.

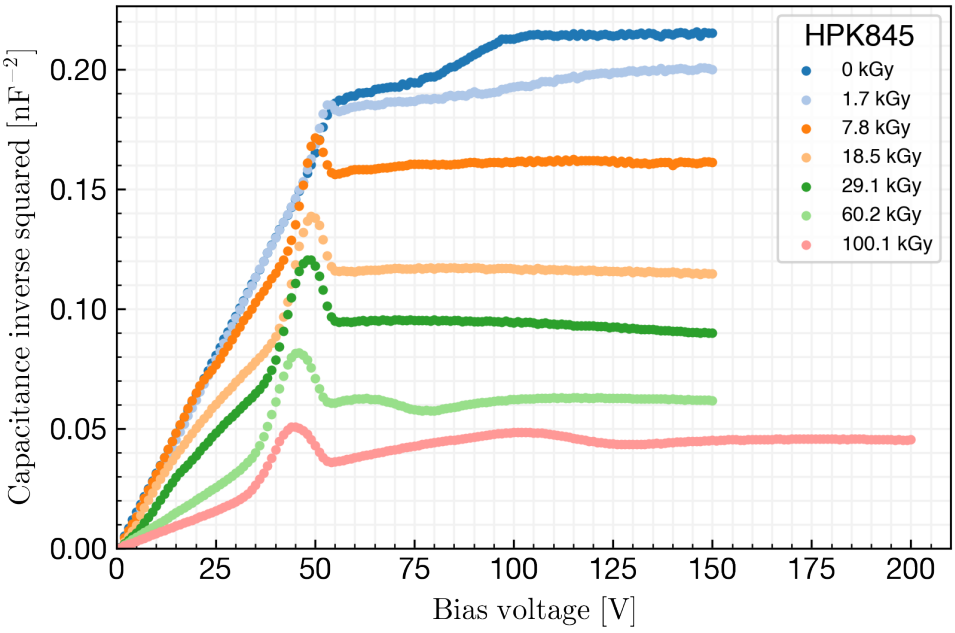

Figure 5.9: CV measurements of the HPK large sensor just after the irradiation

5.2.5 $C_{int}V$ measurement

The $C_{int}V$ measurements were performed with the same settings as for the mini sensor. A plot of $C_{int}V$ vs. irradiation dose obtained for one irradiated C_{int} measurement channel is shown in fig. 5.10.

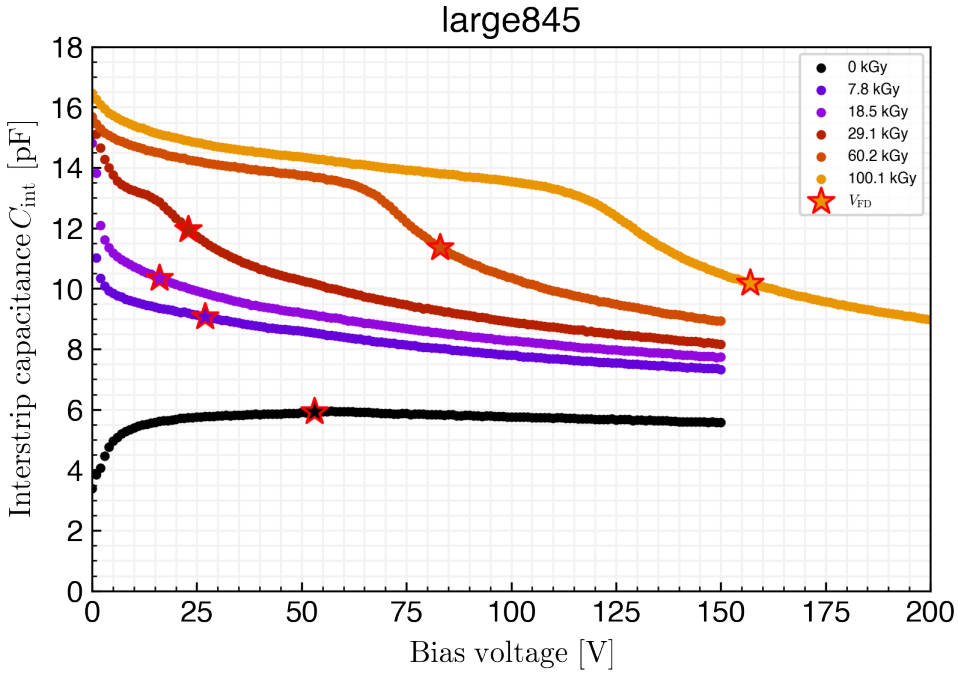

Figure 5.10: $C_{int}V$ measurement of the HPK large sensor just after the irradiation

From this figure, it can be confirmed that C_{int} increases in proportion to the irradiation dose over the entire bias voltage range as C_{int} of the mini sensor; the maximum C_{int} was 6 pF before irradiation, but by irradiated, it is confirmed that the C_{int} is more than 10 pF when no bias voltage is applied and gradually decreases with the applied bias voltage increasing.

After 29.1 kGy irradiation, a shoulder-like area appeared on the C_{int} V curve, which shifted toward a higher bias voltage with increasing irradiation dose. The position of the shoulder is close to V_{FD} , and the decrease in C_{int} appears to decrease after the bias voltage exceeds V_{FD} . From this, it can be inferred that the behavior of C_{int} has some relationship with V_{FD} .

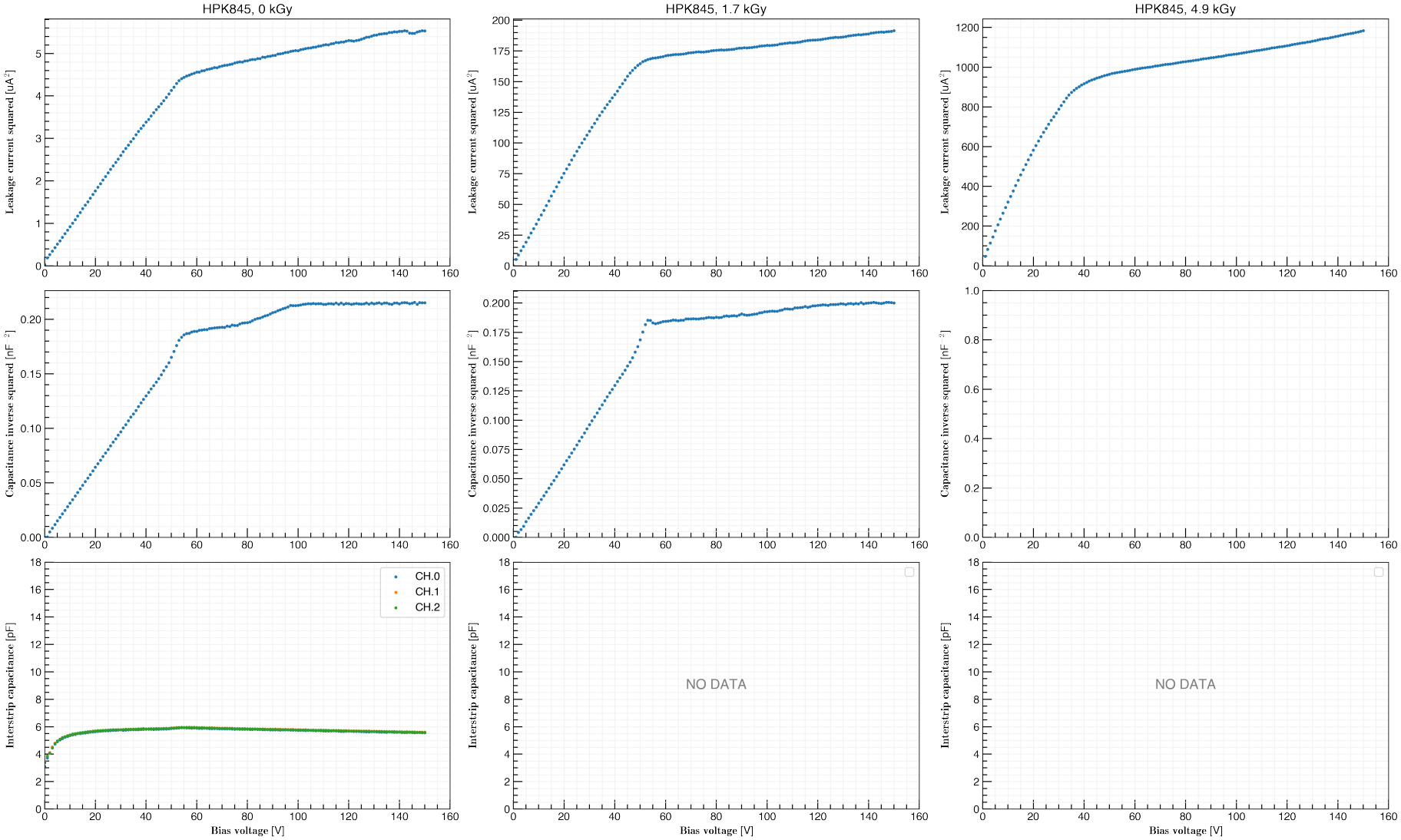

Figure 5.11: The IV, CV, $C_{int}V$ results of large845 0 kGy $\sim$ 4.9 kGy

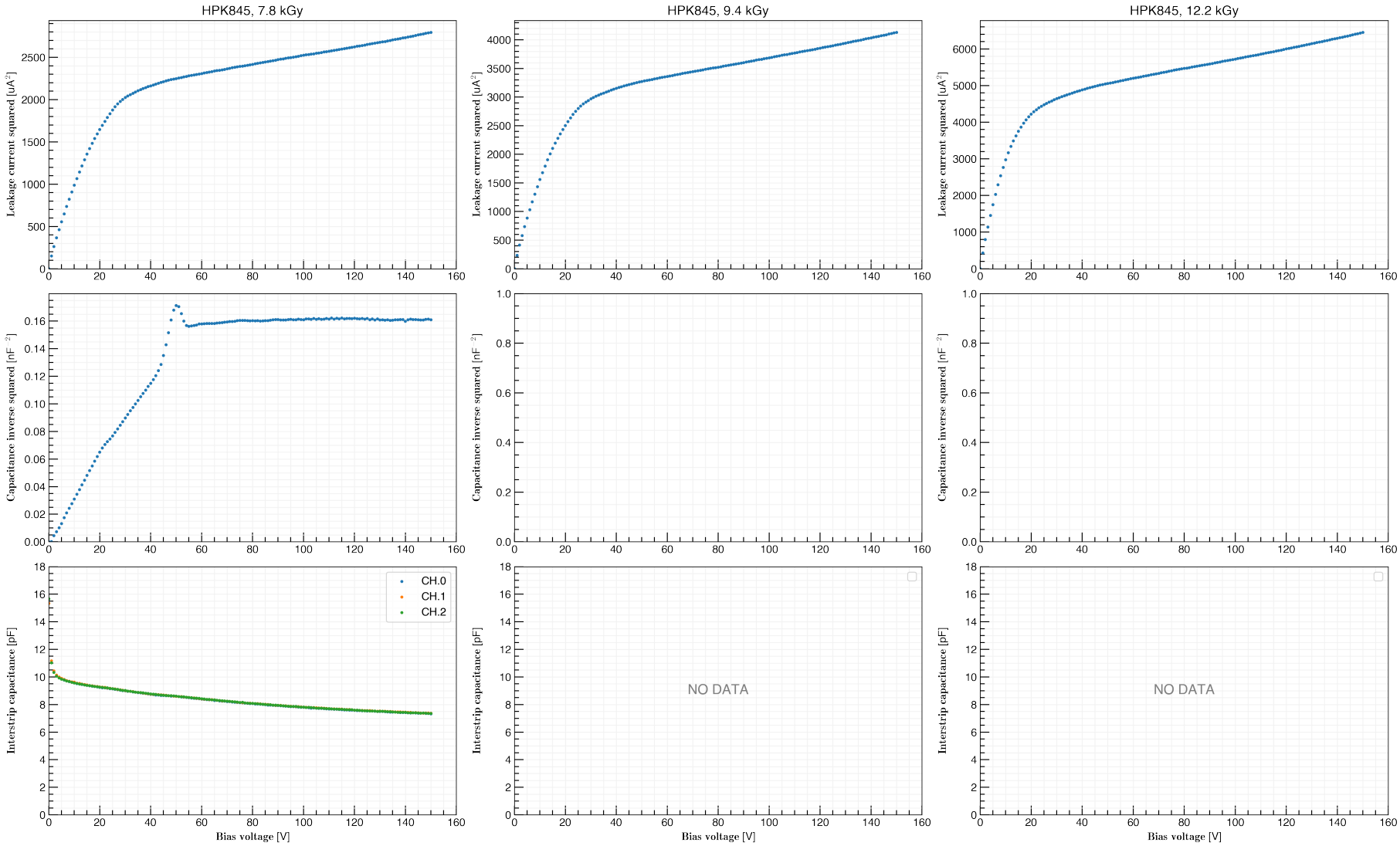

Figure 5.12: The IV, CV, $C_{int}V$ results of large845 7.8 kGy $\sim$ 12.2 kGy

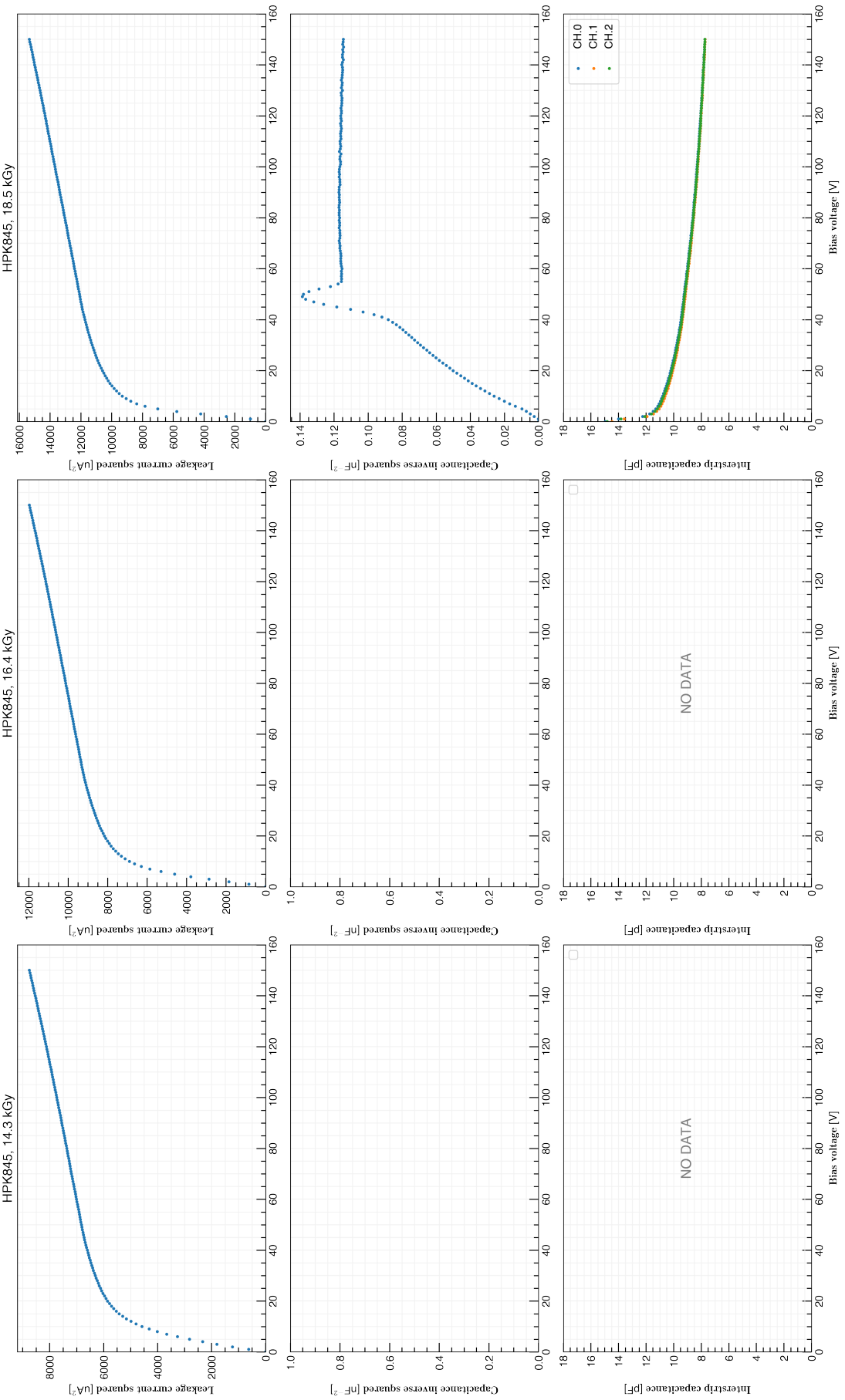

Figure 5.13: The IV, CV, $C_{int}V$ results of large845 14.3 kGy ~ 18.5 kGy

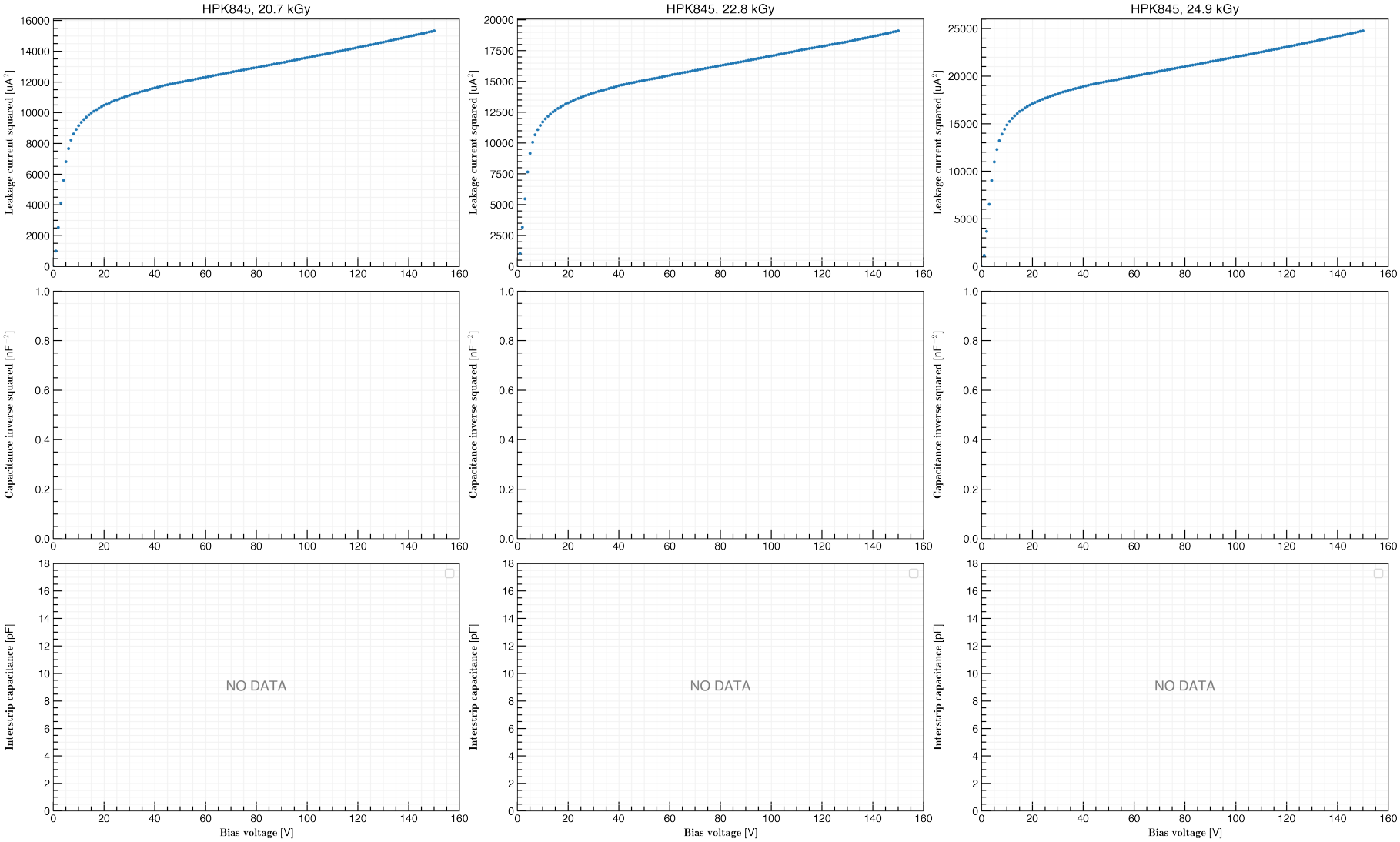

Figure 5.14: The IV, CV, $C_{int}V$ results of large845 20.7 kGy $\sim$ 24.9 kGy

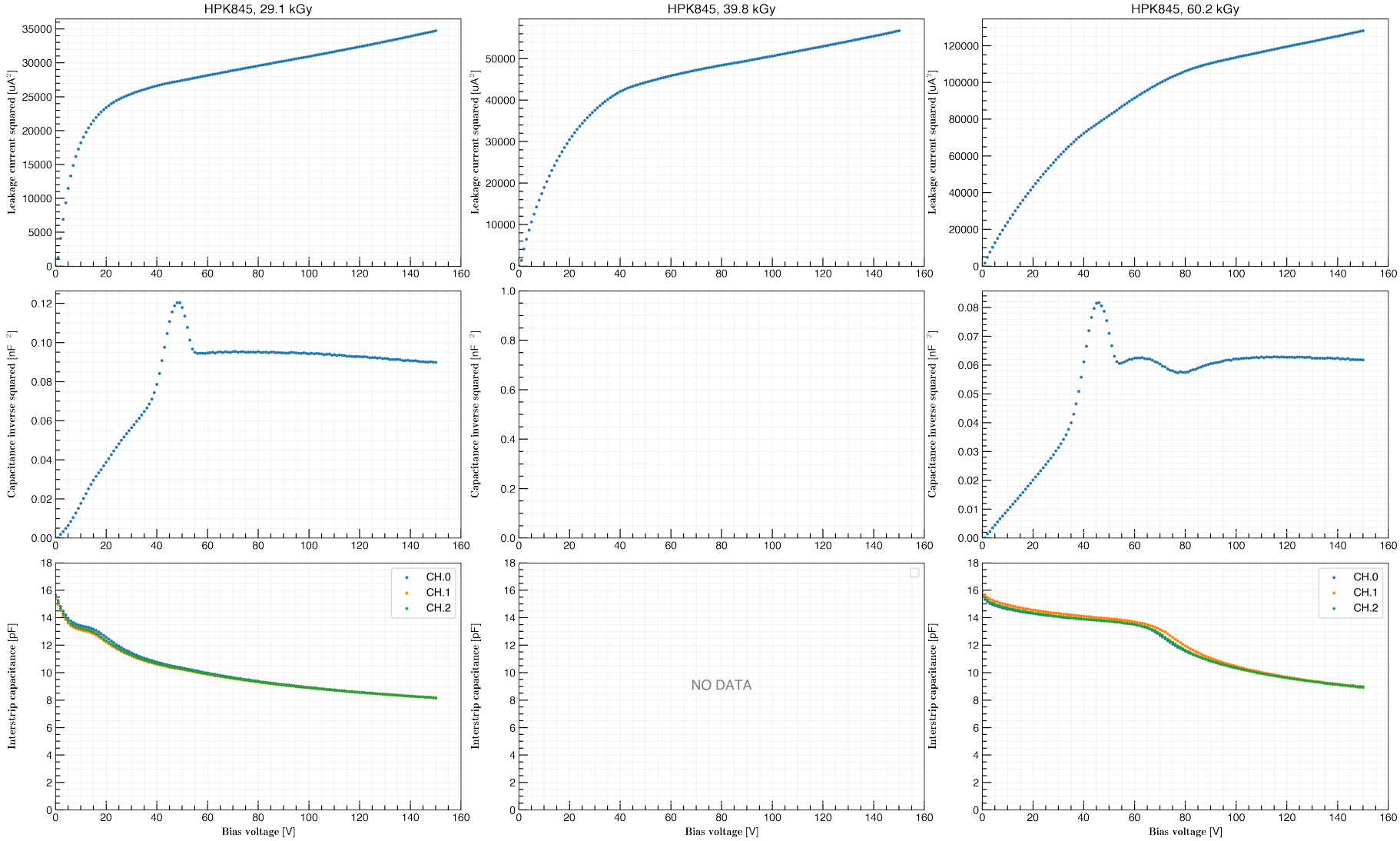

Figure 5.15: The IV, CV, $C_{int}V$ results of large845 29.1 kGy $\sim$ 60.2 kGy

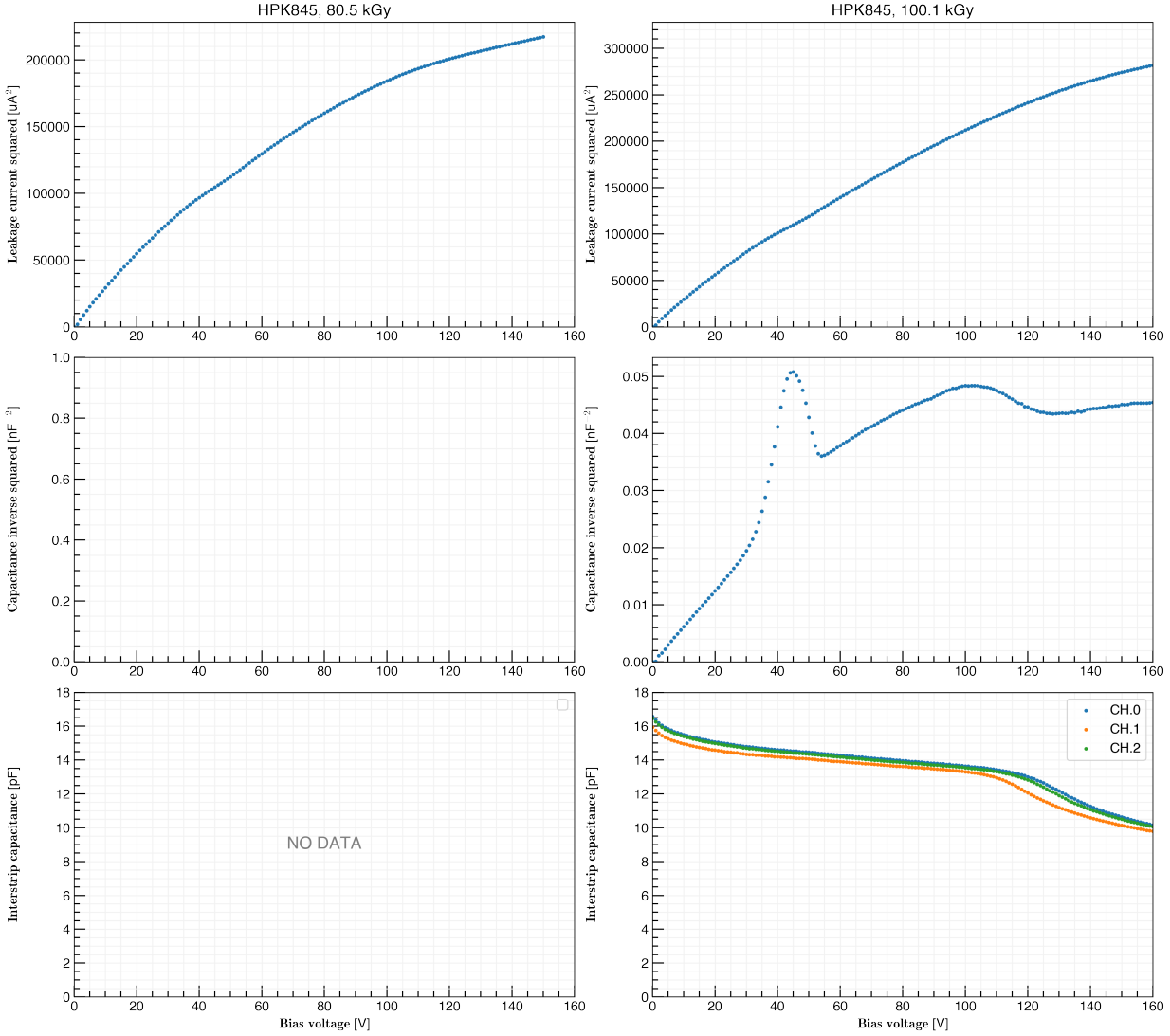
HPK845, 80.5 kGy
HPK845, 100.1 kGy
Leakage current squared [uA²]
Capacitance inverse squared [nF⁻²]
Interstrip capacitance [pF]
NO DATA
CH.0
CH.1
CH.2
Bias voltage [V]

5.3 Analyis and Disscution of IV, CV, $C_{int}V$ results

5.3.1 Definition of the full depletion voltage

As seen in Fig. 5.7, the irradiation changes the shoulder position of the IV curve, that is, the change in V_{FD} can be confirmed. This change indicates that type inversion is occurring. In this section, in order to confirm the behavior of type inversion more precisely, we define the V_{FD} quantitatively as much as possible and check the relationship between the V_{FD} and the irradiation dose. This allows us to see at which irradiation dose type inversion occurs, and then by how much the V_{FD} varies with irradiation dose.

First, as seen in Eq. 3.10, I^2 is theoretically considered to increase proportionally to the voltage before the applied voltage reaches V_{FD} , and not much after it reaches V_{FD} . From this point of view, we believe that there is an inevitable change in the slope of the increase in I^2, and we consider this from the derivative of I^2V. The central difference method was used basically to compute the derivative $f'(x)$ and forward difference or backward difference was used on the edge of data.;

$$f'(x) \approx \begin{cases} \dfrac{f(x+h) - f(x-h)}{2h}, & (x \neq x_{\min}, x_{\max}) \\ \dfrac{f(x_{\min}+h) - f(x_{\min})}{h}, & (x = x_{\min}) \\ \dfrac{f(x_{\max}) - f(x_{\max}-h)}{h}, & (x = x_{\max}) \end{cases} \tag{5.1}$$

$f(x)$: raw data of IV, h: voltage step; 1 V. An example of the calculated result on each dose is from Fig. 5.18 to Fig. 5.21, from top to bottom, they are the results of the zero-order derivative, first-order derivative, and second-order derivative of IV, and the bottom figure is $\mathrm{d}\log I^2/\mathrm{d}V$ (described later).

The results confirm that there is a valley-like structure in all second-order derivative results. The minimum of the valley and the shoulder of the IV curve visually coincide in most of the irradiated dose regions. Also, a structure similar to that shown in Fig. 5.17 appears in the IV curve and its derivatives; the Step-like structure in the first derivative visually coincides with the minimum of the second-order derivative and the shoulder of the IV curve. Thus, the Step-like structure in the first derivative and the minima of the valleys in the second derivative appear to be good indicators.

However, starting at 12.6 kGy, the position of the minimum of the valley of the second-order derivative gradually begins to deviate from the position of the shoulder of the IV curve that we can visually confirm and the Step-like structure in the first derivative become hard to observe. This trend continues until 27.3 kGy. This region has a low V_{FD} and it is considered that the value of the first derivative changes immediately and abruptly starting from 0V, and it hides the Step-like transition structure seen in Fig 5.17. The second-order derivative valley associated with this structure has also shifted accordingly. Therefore, we need to consider methods other than defining V_{FD} from the Step-like structure of the first derivative or the minima of the second derivative troughs for regions with low V_{FD} , especially for regions where the second derivative minima is < 25 V.

As a solution for the region of the second derivative minima is < 25 V, we focused on the slope of the IV curve at V_{FD} . The slope here is not the first derivative of the IV curve, but it

is the first derivative of the IV curve scaled by $1/I^2$;

$$\frac{1}{I^2}\frac{\mathrm{d}I^2}{\mathrm{d}V} = \frac{\mathrm{d}\log I^2}{\mathrm{d}V} \quad , \tag{5.2}$$

since I^2 increases in proportion to the irradiation dose, normalizing the slope of the IV curve by this value allows for comparison across different irradiation doses.

Fig. 5.7 shows that the slope of the IV curve is almost constant just after the shoulder. As V_{FD} becomes smaller, the angle between I^2 and the horizontal axis increases until it reaches V_{FD} $\dot{\mathrm{T}}$his means that the slope at V_{FD} is also expected to increase as V_{FD} becomes smaller. Based on this fact, we took the method of finding the relationship between the slope and V_{FD} in the region where the minima of the second-order derivatives are greater than 25 V, i.e., where V_{FD} coincides with the minima of the second-order derivatives, then extrapolating it to the region where the minima of the second-order derivative are less than 25 V (unclear region). Since there is no difference in the behavior of each sensor, data from multiple sensors were used for fitting and extrapolation. The figure is shown in Fig. 5.22. using linear function fitting and extrapolating to the unclear region resulted in the slope of ~ 0.01 in the unclear region. In this time, $\mathrm{d}\log I^2/\mathrm{d}V$ of the IV curve was calculated from Eq. 5.2 (The Results are included in from Fig. 5.18 to Fig. 5.21), and the place where the value of $\mathrm{d}\log I^2/\mathrm{d}V$ is 0.01 is defined as V_{FD} .

To summarize our definition of V_{FD} ,

1. Calculate $\mathrm{d}I^2/\mathrm{d}V$ and find minima.
2. if minima ≥ 25, Define V_{FD} at the position of the minima.
3. if minima < 25, Calculate $\mathrm{d}\log I^2/\mathrm{d}V$ and find a position where the value equal 0.01, and we define V_{FD} at that position.

The defined V_{FD} results are thus included as green vertical lines in the top figure in Fig. 5.18 through Fig. 5.21. It can be also confirmed that it matches the visual shoulder well.

The discussion that follows uses this definition of V_{FD} .

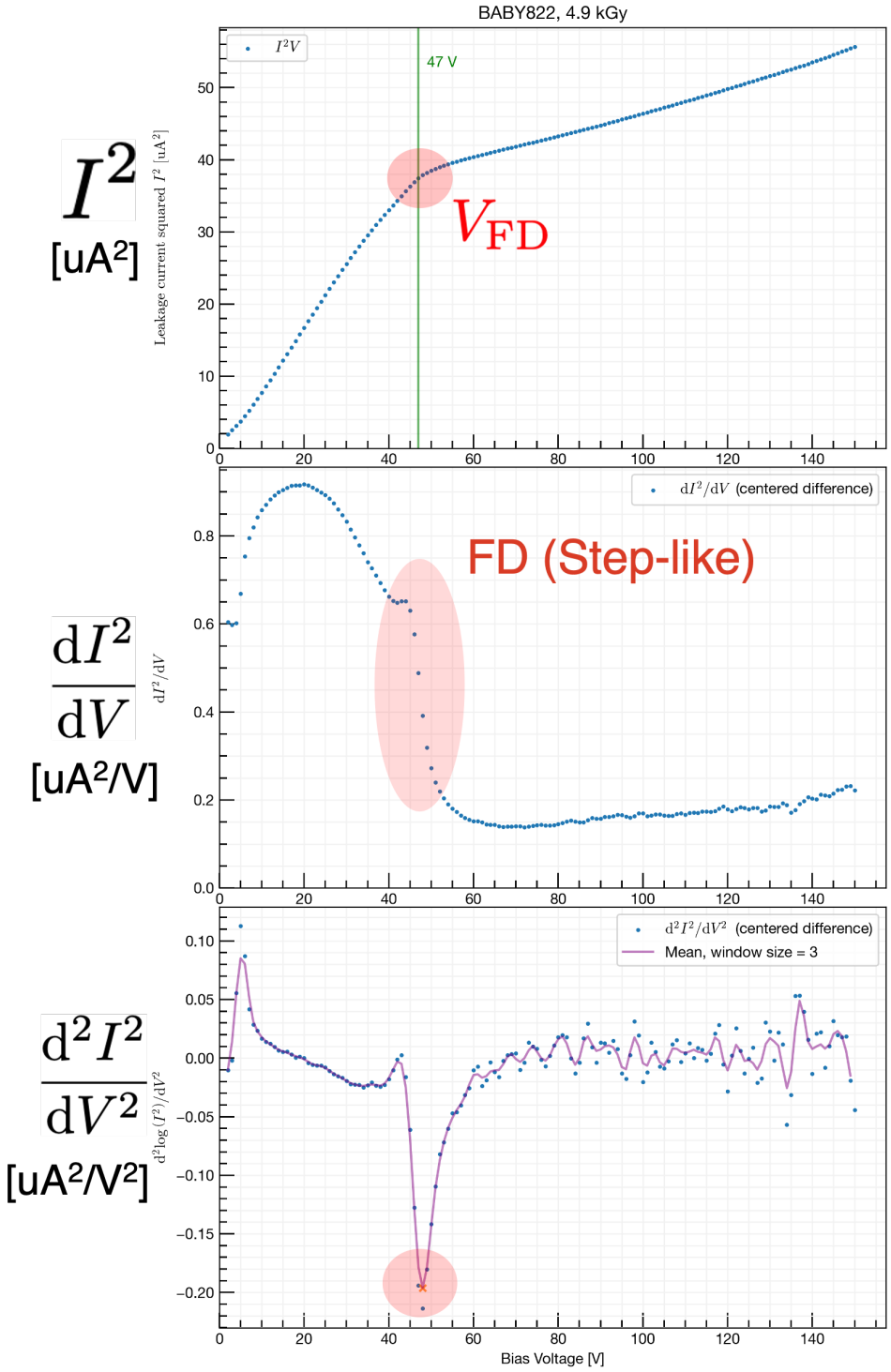

Figure 5.17: Structures related to V_{FD} that appear in the plot of IV and its derivatives

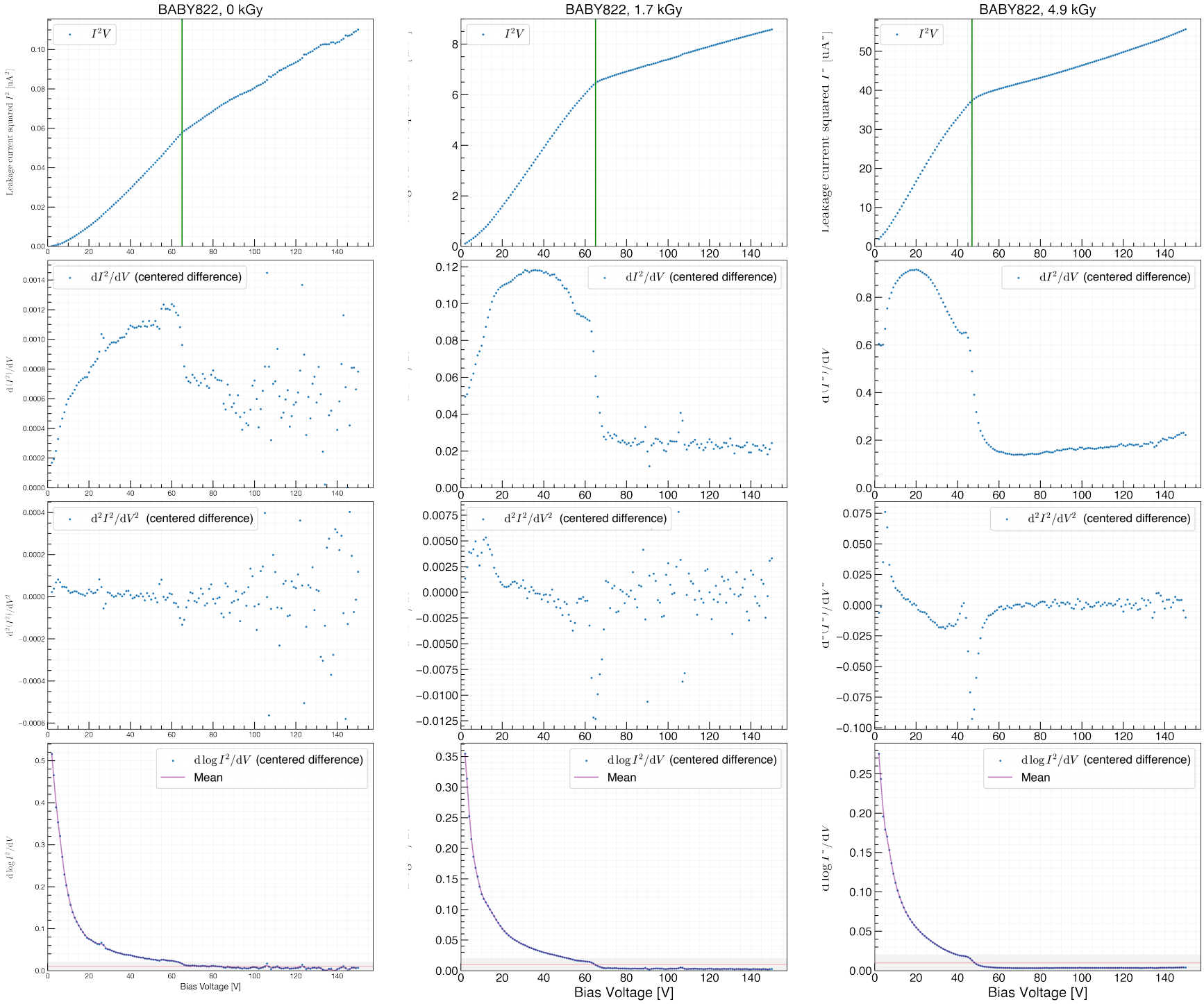

Figure 5.18: Results of the differentiation of IV curve, 0 kGy $\sim$ 4.9 kGy

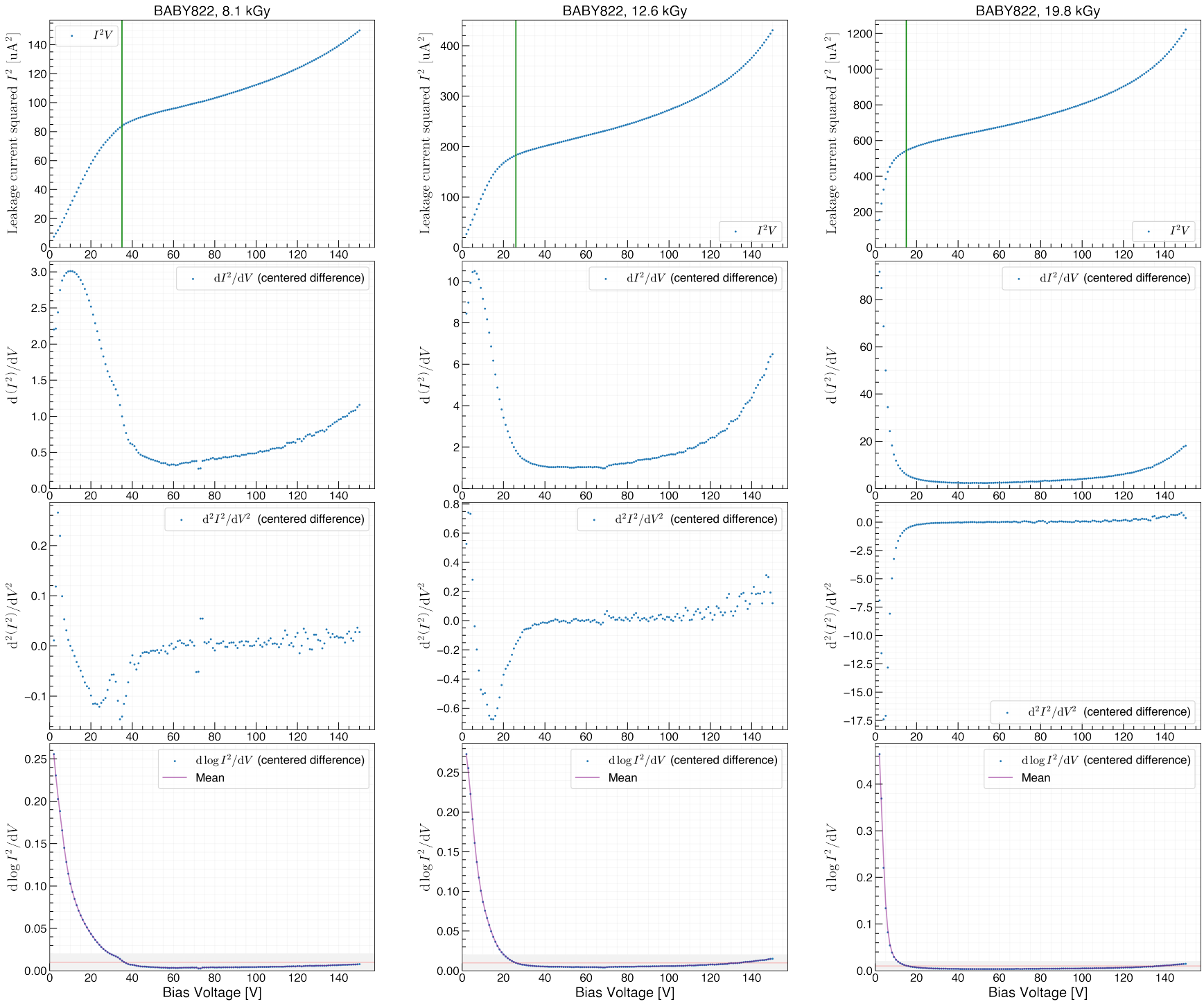

Figure 5.19: Results of the differentiation of IV curve, 8.1 kGy $\sim$ 19.8 kGy

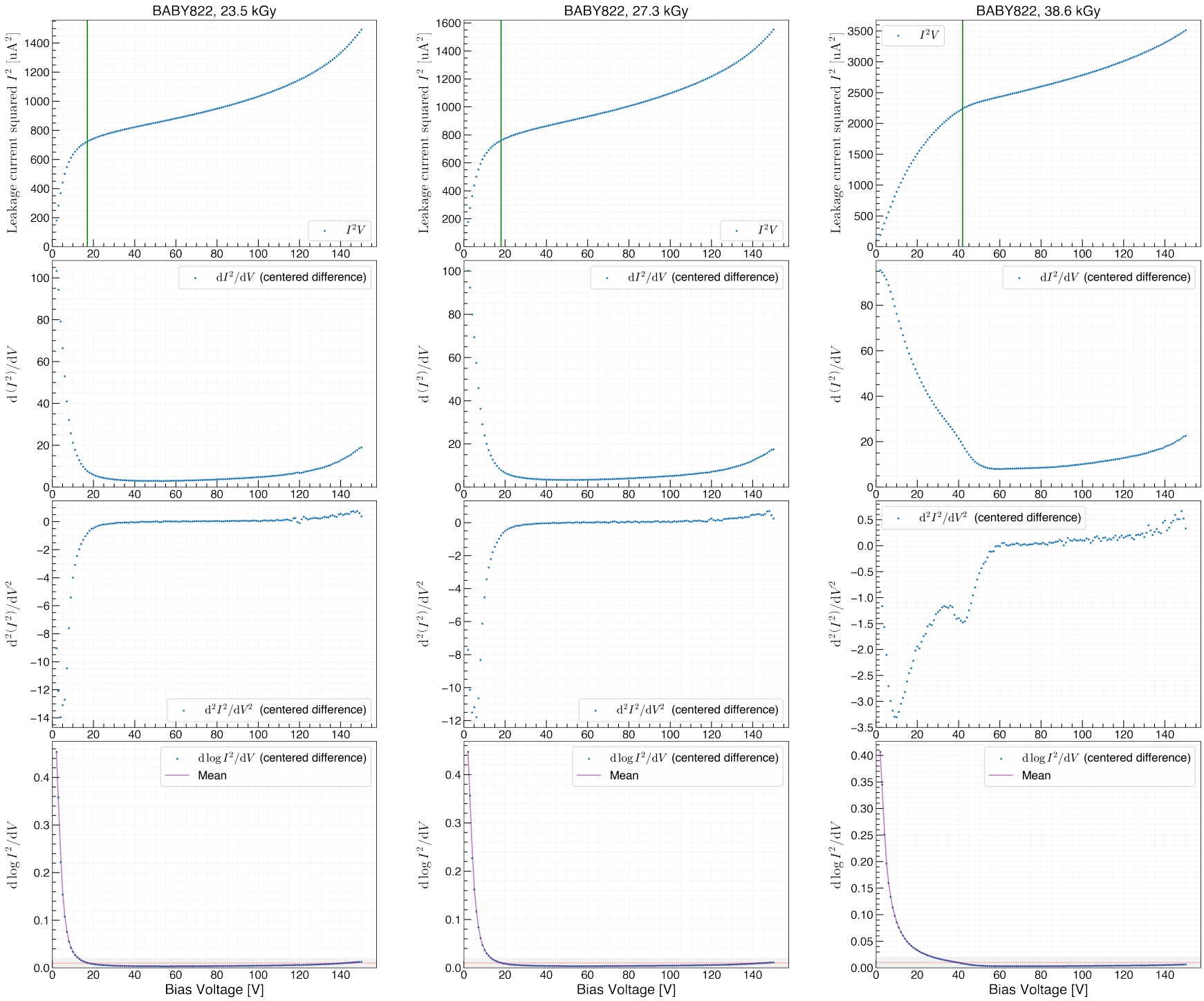

Figure 5.20: Results of the differentiation of IV curve, 23.5 kGy $\sim$ 38.6 kGy

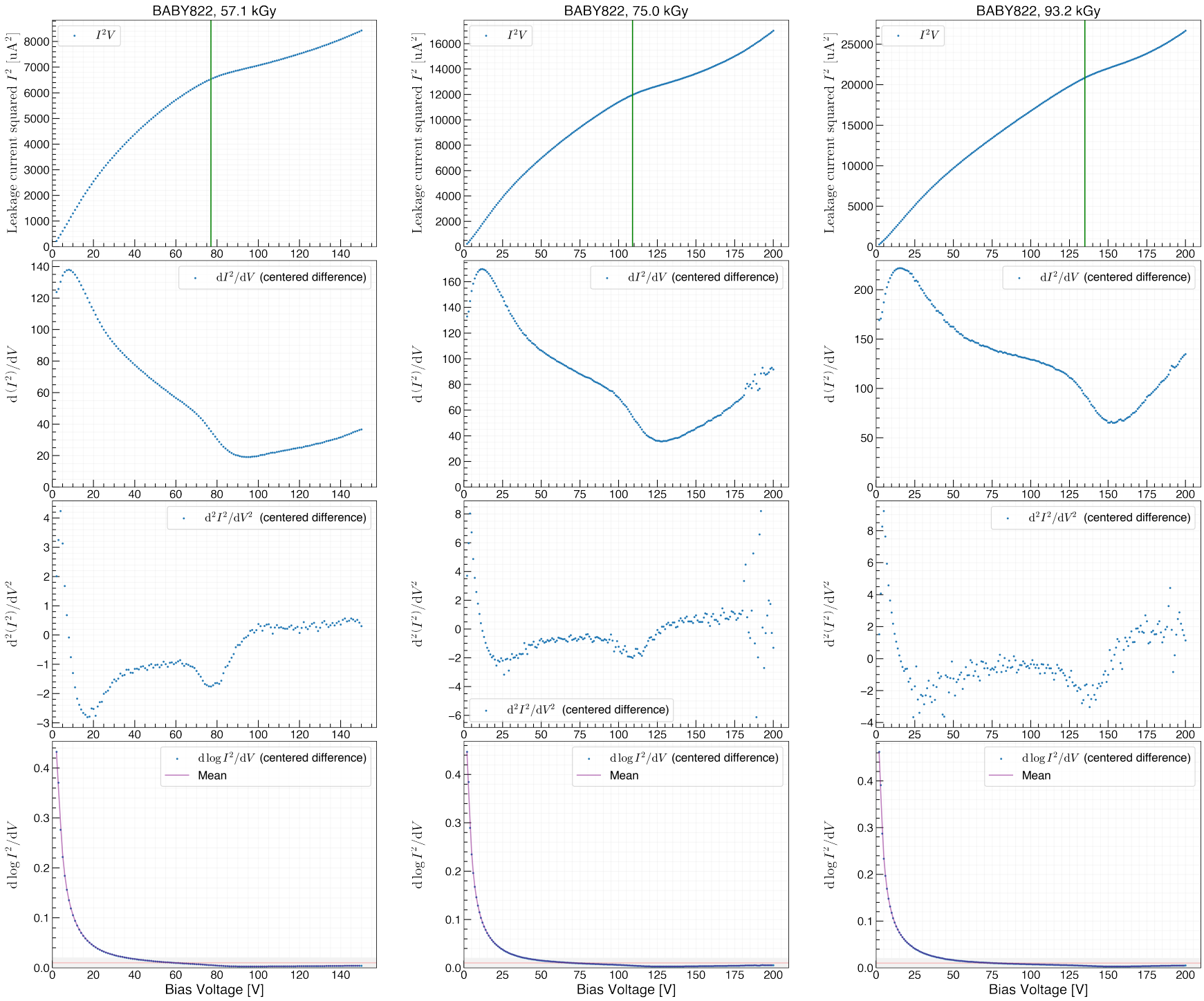

Figure 5.21: Results of the differentiation of IV curve, 57.1 kGy ∼ 93.2 kGy

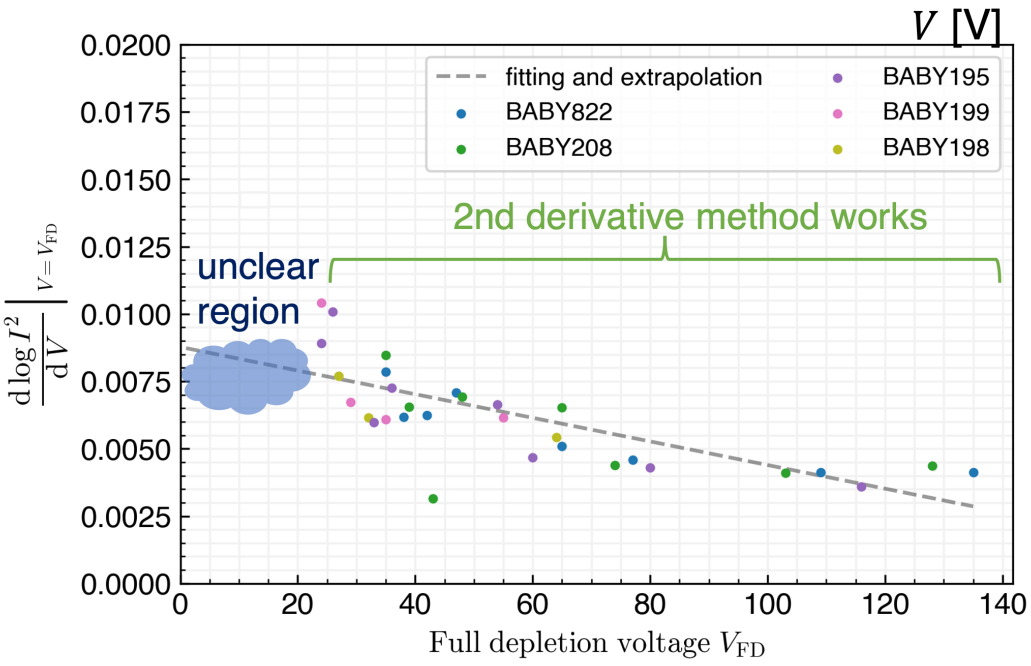

Figure 5.22: extrapolation

5.4 Analysis of the type inversion

5.4.1 The type inversion results just after irradiation

Using the V_{FD} defined in the previous section, Fig. 5.23 plots the relationship between V_{FD} and radiation dose. From the result, looking at mini822 as an example, we can observe a gradual decrease in V_{FD} up to near 20 kGy, and then an increase again after that. This behavior can be considered as exactly the behavior of type inversion; up to 20 kGy, the sensor bulk was n-type, but then it changed to p-type. Because As mentioned in Sec. 3.5.1, N_{eff} decreases monotonically with irradiation dose, and type inversion occurs when $N_{\mathrm{eff}} = 0$. As $|N_{\mathrm{eff}}|$ goes up again after a further decrease, V_{FD} follows this trend, decreasing until before the type inversion and then increasing.

Looking at the other sensors, it can be seen that the minimum value of V_{FD} deviates slightly from sensor to sensor, but in general the behavior is the same.

We compared the value of V_{FD} to the supply voltage (upper limit of 200 V). The innermost SVD will receive a cumulative radiation dose of 20 kGy over 10 years, and at this dose, V_{FD} was observed to be between 15 ∼20 kGy (equivalent neutron fluence $4.5 \sim 6.0 \times 10^{12}$ $\mathrm{n_{eq}/cm^2}$), which is below the upper limit of the supply voltage. Even when the SVD received a dose of 80 kGy, which is four times the cumulative dose for 10 years, V_{FD} did not exceed 150 V, remaining below the supply voltage limit.

In summary, from this irradiation test, we confirmed the type inversion of the SVD sensor will occur at an irradiation dose of 15 ∼ 20 kGy. In addition, even when the SVD received a radiation dose of 80 kGy, which is four times the cumulative dose for 10 years (a safety factor of 4), V_{FD} does not exceed the allowable range of voltage supplied to the SVD.

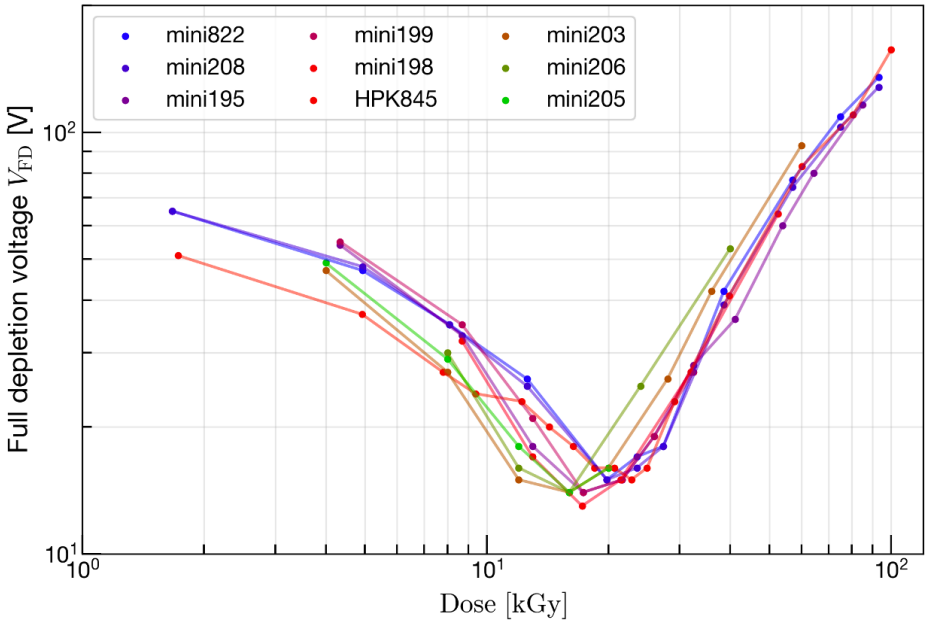

Figure 5.23: The result of V_{FD} changes just after irradiation. This result can be interpreted as the appearance of the type inversion occurring at $15 \sim 20$ kGy. HPK845 means large845

5.4.2 The type inversion with annealing effect

The type inversion we have discussed so far is the result immediately after irradiation, but the annealing effect can repair radiation damage, causing changes in V_{FD} over time. Fig. 5.24 shows the temporal evolution of V_{FD} to see the annealing effect. The annealing effect is considered to be completed at 2×10^2 hours ($\approx$ 8 days) from Fig. 5.24 since there is no change in V_{FD} for most of the sensors after 200 hours. In the figure, it can be seen that the V_{FD} gradually decreases for sensors with an initial point V_{FD} greater than 35 V, while for sensors lower than 35 V, the V_{FD} increases (mini197, 199, 205)* or does not change much.

The primary aim of Fig. 5.25 is to examine how the type inversion changes with the annealing effect, as shown by the plot of V_{FD} versus irradiation dose for various sensors. The data for this analysis were collected after 1×10^3 hours from the irradiation test. The valley-like structure in this figure corresponds to the type inversion behavior and indicates that the annealing effect restores radiation damage to the sensor. This causes the position where type inversion occurs to shift to a higher dose; it changed from $15 \sim 20$ kGy to $50 \sim 80$ kGy with the annealing effect. Furthermore, we can also confirm that the V_{FD} does not exceed 100 V on the sample 100 kGy irradiated. Therefore, we can expect that we can apply a bias voltage sufficiently to exceed the V_{FD} with 2×10^2 hours ~ 8 days (room temperature) annealing effect even if 100 kGy was irradiated.

*The rising voltage suggests that the annealing process has been completed and the reverse annealing process has begun before the data for the first point was collected. Further measurements will be taken to determine if the voltage continues to increase, which would confirm this conclusion

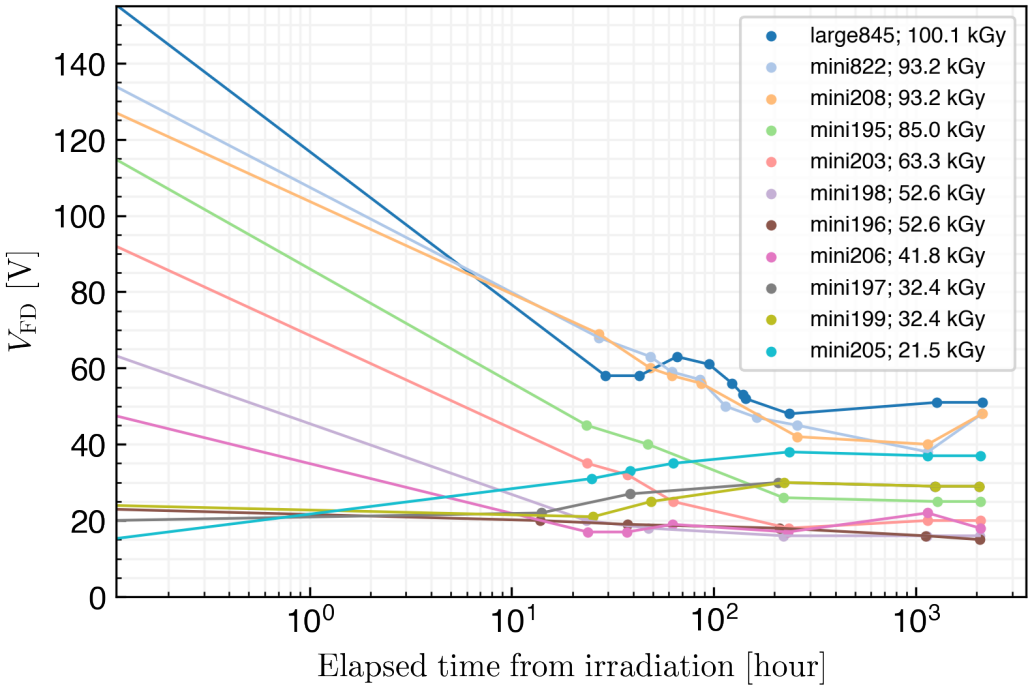

Figure 5.24: V_{FD} vs elapsed time

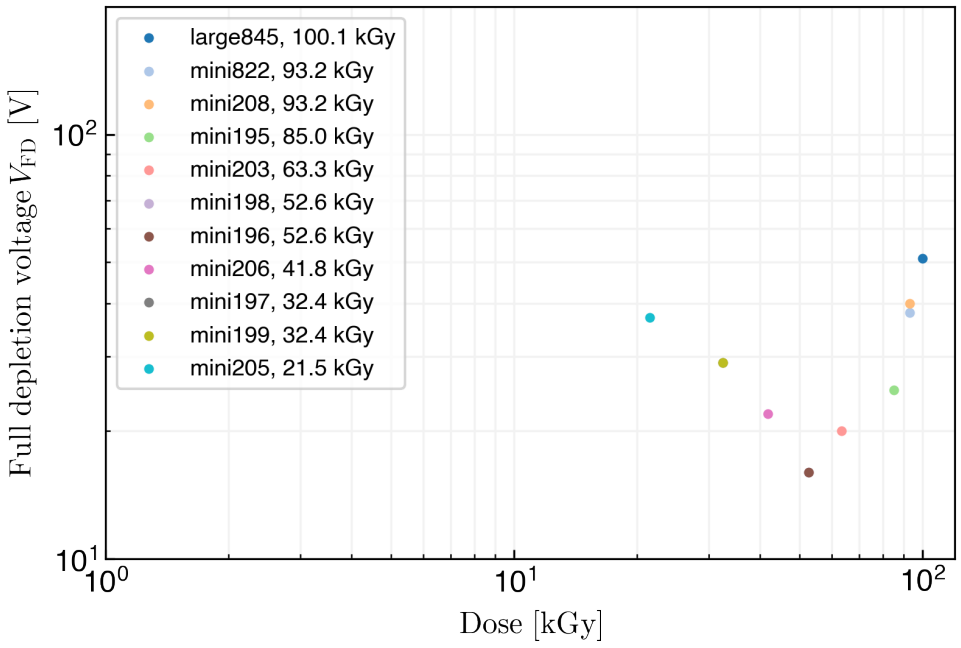

Figure 5.25: The result of type inversion with annealing effect (after 1×10^3 hours)

5.5 Analysis of leakage current increase

5.5.1 The damage factor and noise just after irradiation

The fact that the leakage current increases in proportion to the irradiation dose was explained in Sec. (4.TBD). First, we plotted the leakage current vs. irradiation dose at V_{FD} for the mini sensor. The figure is shown in Fig. 5.26.

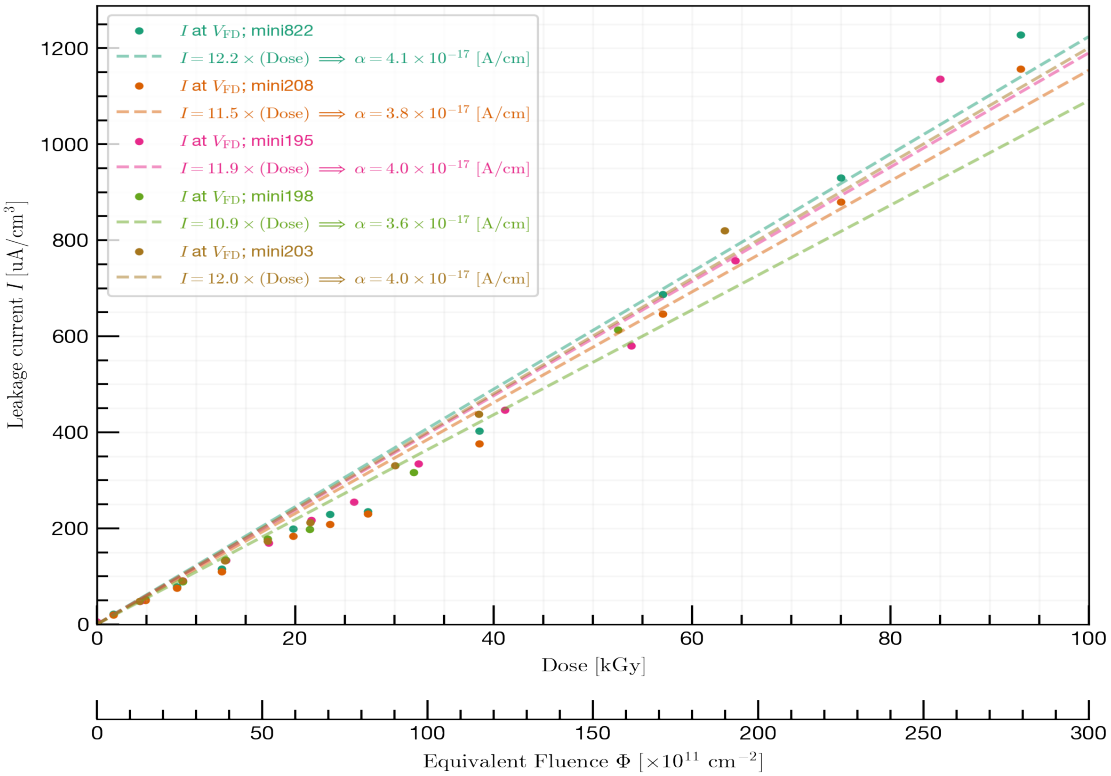

Figure 5.26: The leakage current at V_{FD} per sensor volume vs. irradiated dose, the result just after irradiations

We performed a linear function fitting the results by considering it to be an equation; $I/V = \alpha\Phi_{\mathrm{fluence}}$ where $\Phi_{\mathrm{fluence}}\,[\mathrm{cm}^{-2}]$ is equivalent neutron fluence which we defined to be $3 \times 10^{11}\,[\mathrm{cm}^{-2}] = 1\,[\mathrm{kGy}]$, V is sensor volume. The calculated damages factors are summarized in Table. 5.1. Now that we have calculated the damage factor, which is a proportional constant,

Table 5.1: The damages factor of sensor just after irradiation

sensor	damage factor α [A/cm]	slope [µA/cm^2/Mrad]	temperature [°C]
mini822	4.1×10^{-17}	3.9	17.0 ± 0.2
mini208	3.8×10^{-17}	3.7	17.0 ± 0.2
mini195	4.0×10^{-17}	3.8	17.0 ± 0.2
mini198	3.6×10^{-17}	3.5	17.0 ± 0.2
mini203	4.3×10^{-17}	3.8	17.0 ± 0.2

we can estimate how much the leakage current increases with irradiation dose. The question for the SVD is whether the increased current will exceed the allowable current (10 mA) of the power supply to the SVD. A power supply module is the one responsible for an area equivalent to one small sensor (active area: $3.84 \times 12.29\,\mathrm{cm}^2$) on the innermost layer. Therefore, assuming the sensor area to be that area, and using a damage factor of 4.1×10^{-17} in the calculations, it was obtained that irradiation doses up to 75 kGy ($\approx 2.3 \times 10^{13}\,\mathrm{n_{eq}/cm^2}$) would not exceed 10 mA. This dose amount is equivalent to 3.75 times (safety factor 3.75) the 10-year cumulative radiation dose received by the innermost SVD.

Comparison of the results of the slopes (table 5.1) from our measurement with the results obtained from the SVD operation is shown in Fig. 5.27. This figure shows that our measure-

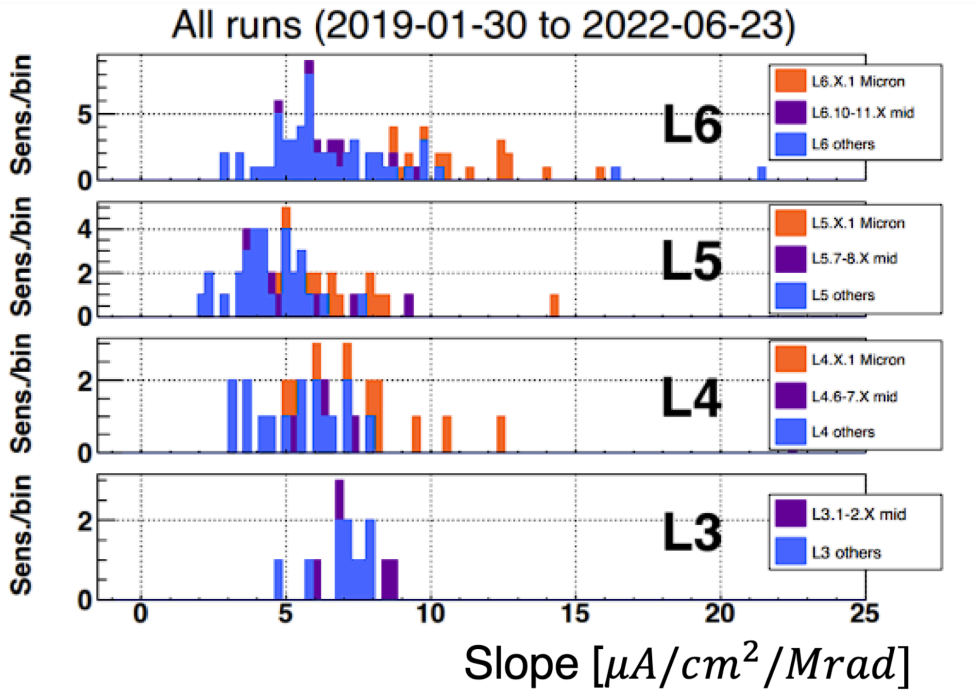

Figure 5.27: The histogram of the slope of leakage current and irradiation dose from operating SVD modules [12]

ments resulted in smaller values, but they were relatively close to the values of the operating SVD modules. The discrepancies in the measurements could be caused by differences in the accuracy of the radiation dose estimates in the operating SVD and the ambient temperature.

Since the leakage current is small before irradiation, the noise contribution from the leakage current is small. However, since the leakage current increases with irradiation dose, it is necessary to estimate how much the noise increases with irradiation dose. Thus, the next step is to determine how much the noise (ENC_I) current flowing into APV25 increases with increasing leakage current. The following Eq. 5.3 is used to calculate the noise from the leakage current;

$$\mathrm{ENC}_I = \frac{\mathfrak{e}}{2}\sqrt{\frac{i_{\mathrm{leak}}\, t_{\mathrm{integ.}}}{q_e}} \quad , \tag{5.3}$$

$\mathfrak{e}$: Euler's number, $t_{\text{integ.}}$: shaping time of APV25; 50 ns [11], q_e: elementary charge. Here, for comparison and to consider the situation of the innermost SVD, the leakage current of each irradiated sensor sample is scaled to the volume of the innermost SVD small sensor.

$$i_{\text{leak}} = I_{\text{leak}} \times \frac{V'}{V} \times \frac{1}{\#\text{P RO-Strips}_{\text{small}}} \quad , \tag{5.4}$$

V': the volume of the innermost SVD small sensor, V: irradiated volume of each sensor, #P RO-Strips: the number of P side readout strips of the small sensor. The result is shown as Fig. 5.28

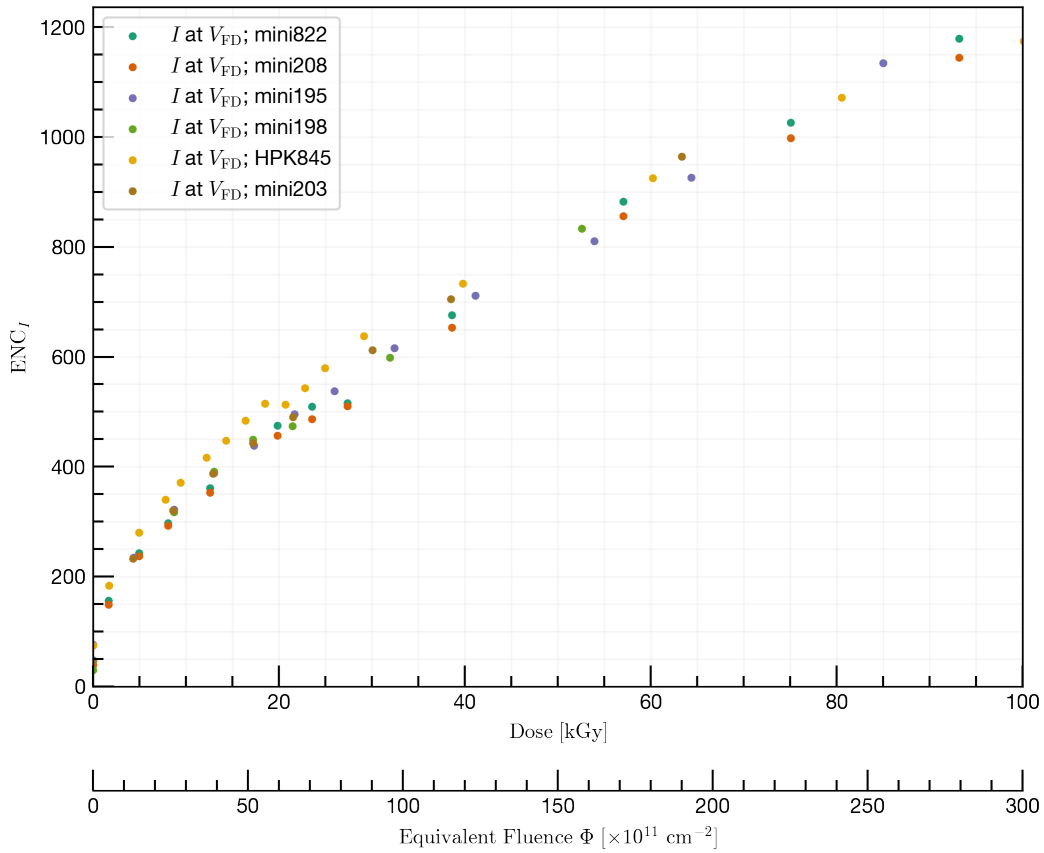

Figure 5.28: Calculated ENC_I from leakage current scaled to SVD innermost layer small sensor. HPK845 represents large845

On the other hand, noise ENC_C from interstrip capacitance can be calculated from interstrip capacitance of large845 using $A+B\times C$ that C is capacitance, A and B are ASIC-specific values. These values for our ASIC, APV25 are already examined and reported on [20]; it is Eq. 5.5, the calculated result of large845 using Eq. 5.5 is shown in Fig. 5.29.

$$\text{ENC}_C = 270 + 38 \times C \tag{5.5}$$

Comparing these two results, We can confirm that the noise source affecting the APV25 is the noise due to the interstrip capacitance of the SVD sensor when not irradiated and in low

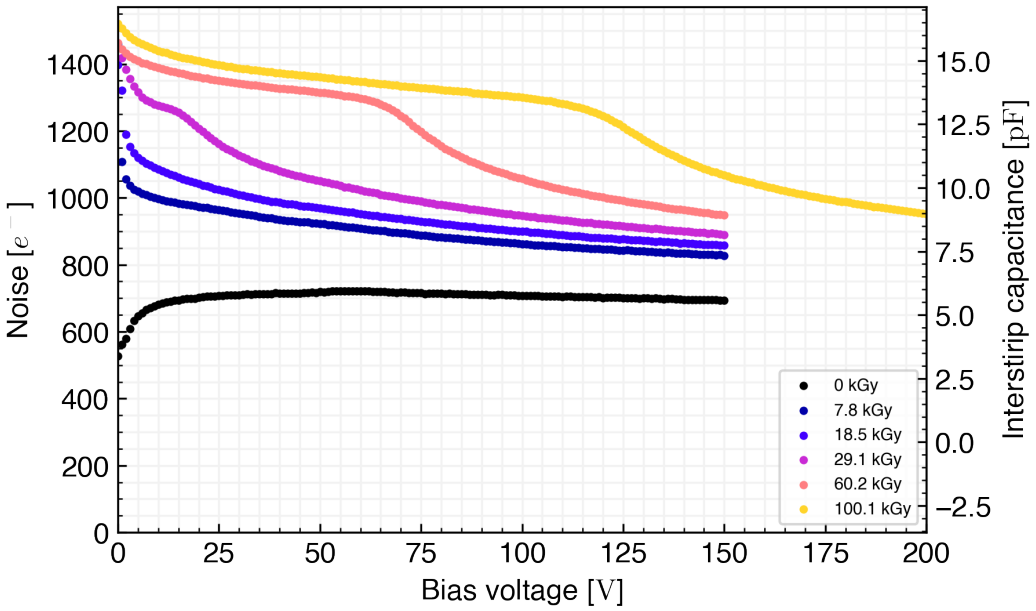

Figure 5.29: The noise ENC_C from interstrip capacitance of the large845

radiation environments, but the noise ENC_I due to leakage current increases to the comparable level or more after irradiation.

Assuming further that the noise in ENC_I and ENC_C is occupied in the ASIC external noise ENC, ENC can be calculated from ENC_I and ENC_C as a quadratic sum;

$$\mathrm{ENC} = \sqrt{\mathrm{ENC}_I^2 + \mathrm{ENC}_C^2} \tag{5.6}$$

The calculated result of large845 is Fig. 5.30. The results show that noise increases 1.4-fold from pre-irradiation to 18.5 kGy irradiation and approximately doubles with 60 kGy irradiation. Although the increase in noise from interstrip capacitance alone could be suppressed to some extent by applying more voltage, the addition of leakage currents reduces the noise reduction effect.

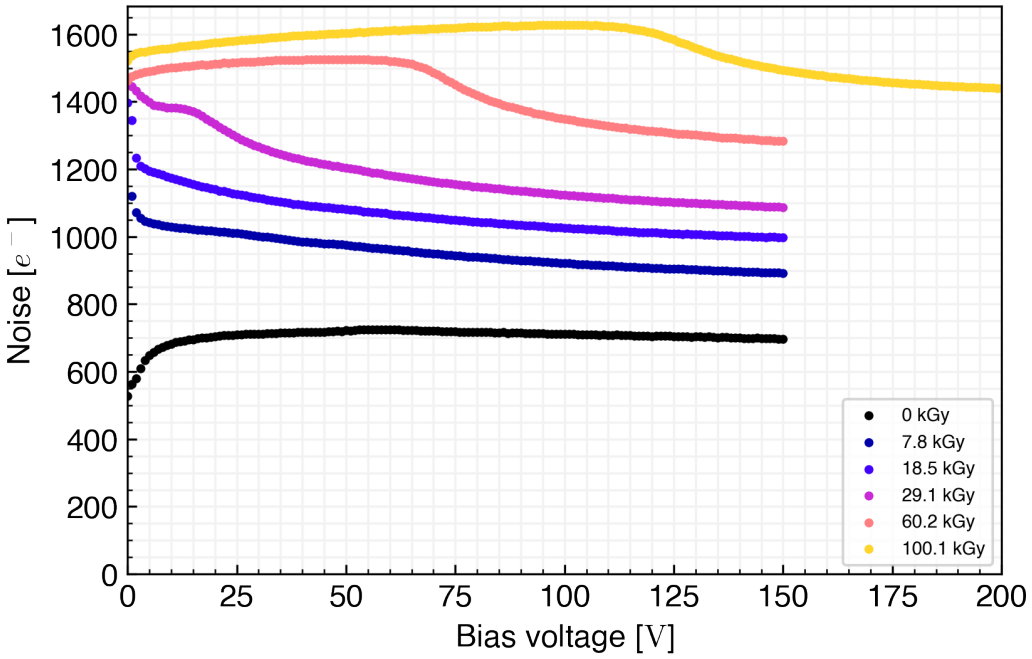

Figure 5.30: Noise ENC calculated from the quadratic sum of leakage current and interstrip capacitance of the large845, the results just after irradiation

5.5.2 The damage factor and noise of with anneal effect

To see changes in the damage factor with annealing effect as in Sec. 5.25. The data at 1×10^3 hours are presented here; there was no change compared to the data at 2×10^3 hours. It is shown in Fig. 5.31 and the damage factor is calculated by fitting points between different sensors.

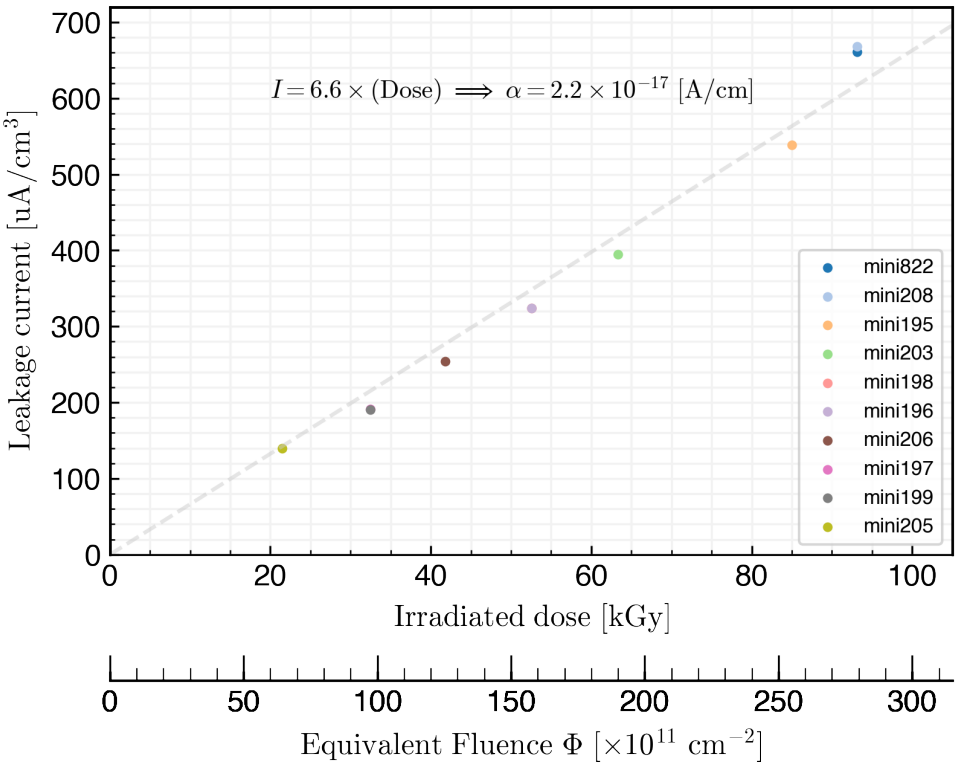

Figure 5.31: Leakage current vs dose with annealing effect

The results show that the annealing effect reduced the damage factor by nearly half; the radiation damage increased the leakage current, but the annealing effect restored the radiation damage and reduced the increased leakage current.

Table 5.2: The damages factors with other studies

sensor	damage source	α [$\times 10^{-17}$ A/cm]	T_1 *1	t *2	T_2 *3
Our result w/o annealing effect	90 MeV e^-	4 (5)	17.0 ± 0.2 (20)	—	—
with annealing effect	90 MeV e^-	2.2 (1.6)	$24.0^{+0.2}_{-0.3}$ (20)	1×10^3	$17 \sim 27$
RD48, Rose collab. [13]	24 GeV p	(3.99 ± 0.03)	20.0	1.3	60
BaBar SVT [18] [21]	900 MeV e^-	2.7 *4	23	—	—
ATLAS SCT [8]	24 GeV p	0.23 (6.01)	-9 (20)	—	—

*1 T_1 : measurement temperature [°C]
*2 t: elapsed time [hours]
*3 T_2 : storage temperature [°C]
*4 There is a two-month interruption during the irradiation period. Annealing effects cannot be neglected.

The results with and without annealing effects are summarized in Table 5.2, and since there have been many investigations into the damage factor of silicon sensors, we add some results from other studies to the table. In comparison, our results are close to the other results.

Here ENC was calculated from the leakage current as in Fig.5.28. As a reference, the results

of the large845 sensor without the annealing effect are plotted. From this figure, it does not appear that annealing reduces noise much at 20 kGy, but at higher doses, for example around 60 kGy, noise can be reduced by about $200e^-$. Next, look at how the C_{int} V and noise ENC_C

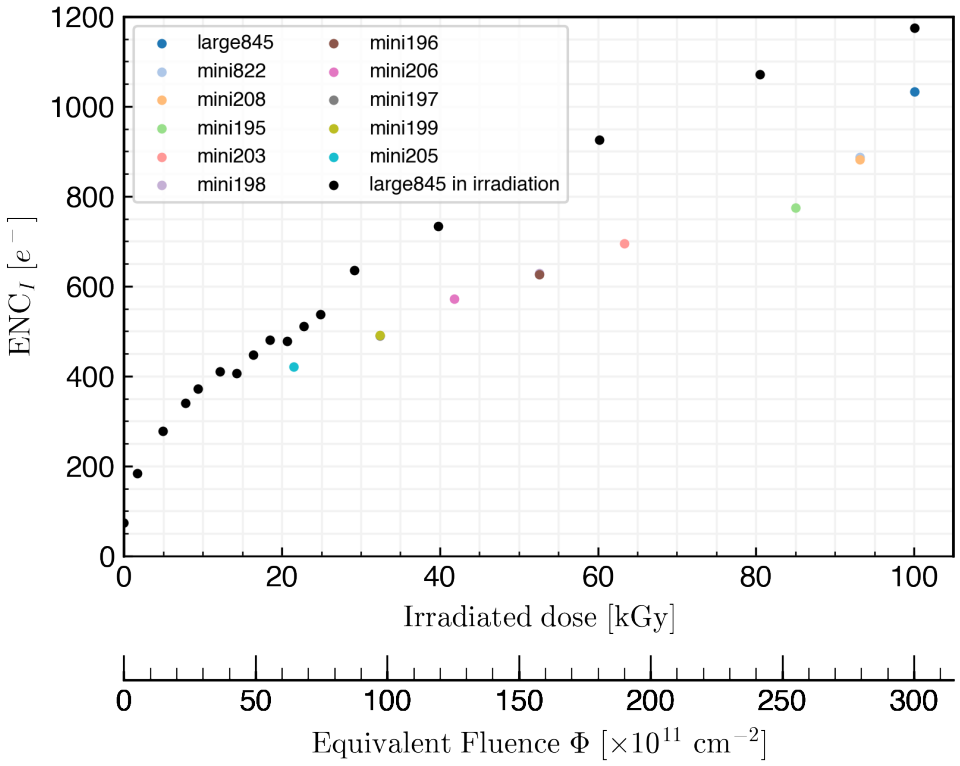

Figure 5.32: The ENC_I at V_{FD} vs dose with the annealing effect (after 1000 hours)

of the large845 have changed due to the annealing effect. The results are shown in Fig 5.32 Comparing C_{int} immediately after irradiation and after 1×10^3 hours, it can be confirmed that C_{int} has indeed gone down. On the other hand, after another 1×10^3 hours, the C_{int} at 2×10^3 hours is lower in the low voltage region, but after 30 V, the C_{int} at 2×10^3 hours is higher. This behavior also can be seen in other C_{int} measurement channels. We can confirm the position of the curved mountain-like structure and V_{FD} position coincide. Next, we should confirm the change of ENC due to the annealing effect by taking a quadratic sum of ENC_I and ENC_C as in Fig. 5.30.

It can be seen that ENC is reduced by about $150 \sim 250\, e^-$ due to the annealing effect. On the other hand, in the region of higher voltage than V_{FD} , there is no significant difference between 1×10^3 hours and 2×10^3 hours.

Also, although 2×10^3 hours is indeed lower ENC_C at lower voltages than V_{FD} this does not mean that SVD should be operated at lower voltages than V_{FD} but other factors such as charge collection efficiency should be checked.

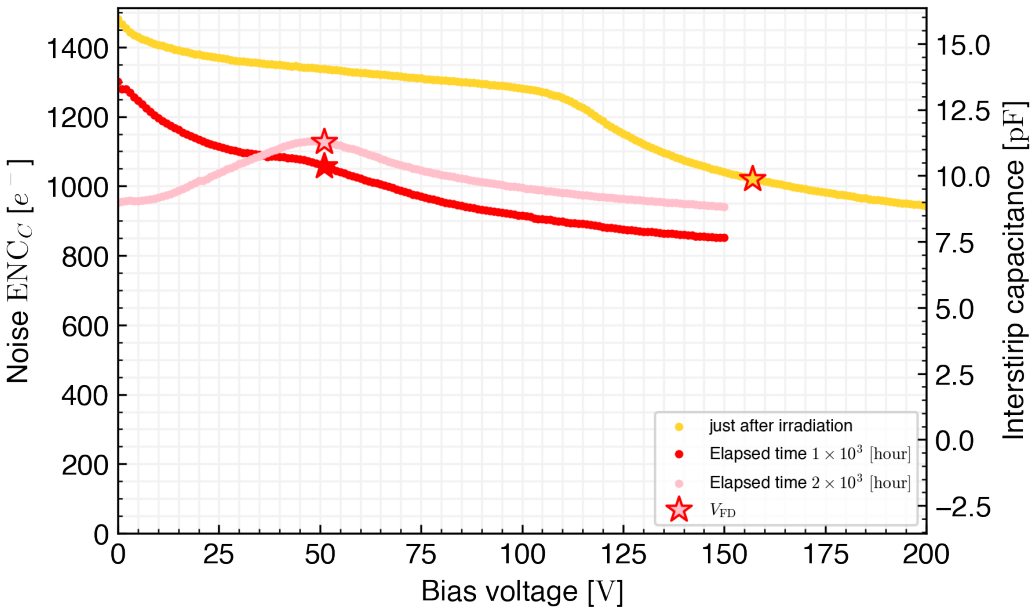

Figure 5.33: The $C_{int}V$ (right vertical axis) and ENC$_C$ (left vertical axis) of large845 changes with annealing effect

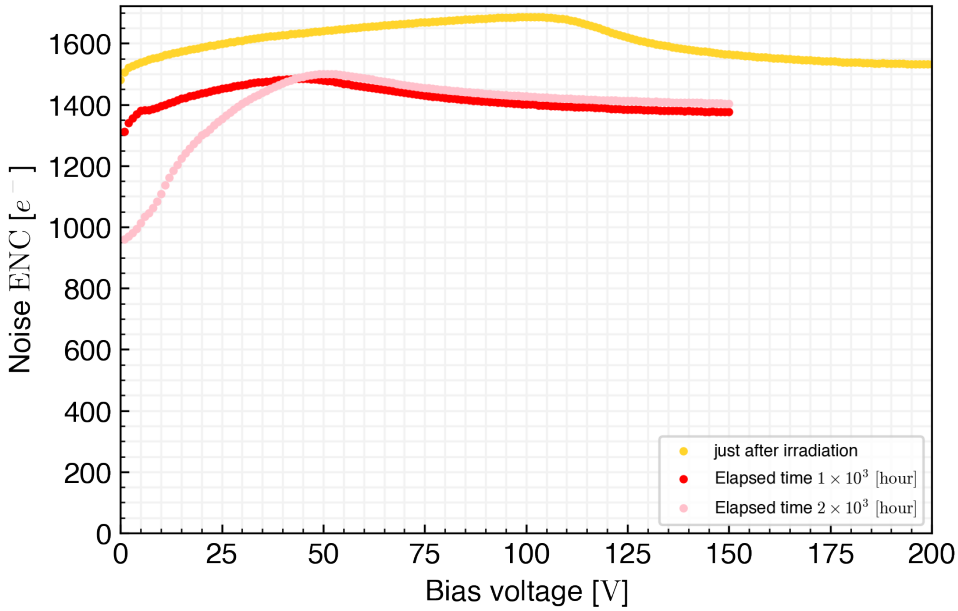

Figure 5.34: Noise ENC calculated from the quadratic sum of leakage current and interstrip capacitance of the large845 with annealing effect

Chapter 6

Measurement of Noise and Charge collection efficiency change

Here we discuss the changes in noise taken by the readout ASIC and charge collection efficiency due to radiation damage. Sec. 6.1 and Sec. 6.2 describe the setup for irradiation and the setup for charge collection using a beta source, and Sec. 6.3 describes the procedure for obtaining correction data and charge collection data. Sec. 6.4 describes the changes in the measurement results of the correction data including noise, and Sec. 6.5 describes the changes in the actual charge collection performed using the beta source, and discussion on Charge collection efficiency. Here, data acquisition is performed using the Sub-assembly module, Backward (SBW), which is a readable module that connects the DSSD and readout ASICs. Refer to Fig. 2.4

6.1 Irradiation system for SBW module

To measure the noise and the Charge Collection Efficiency (CCE), it is necessary to have aa readout ASIC (APV25) connected to the sensor and acquire the raw signal output from it. Therefore, to investigate changes in the noise and the CCE before and after irradiation, it is necessary to irradiate the module to which the APV25 and sensor are connected. We prepared the SBW module for irradiation. Irradiation of the SBW module (hereinafter called SBW) was done in parallel with the large845 sensor as shown in Fig. 6.1. For the beam hole, the large845 sensor was set on the first layer and the SBW is the second layer. The large845 sensor and SBW have the same geometry of the sensor part and the same irradiation time, so the given irradiation dose is the same 100.1 kGy and the same irradiated area; a 16 mm wide area along the Pstrip at the center of the sensor. Therefore, The central Pstrips were irradiated uniformly and all N side strips were irradiated non-uniformly. N side of the sensor facing the beam hole.

In addition, during the irradiation test, we did not perform any measurements and did not apply any bias voltage on the SBW module, only irradiation to the SBW module.

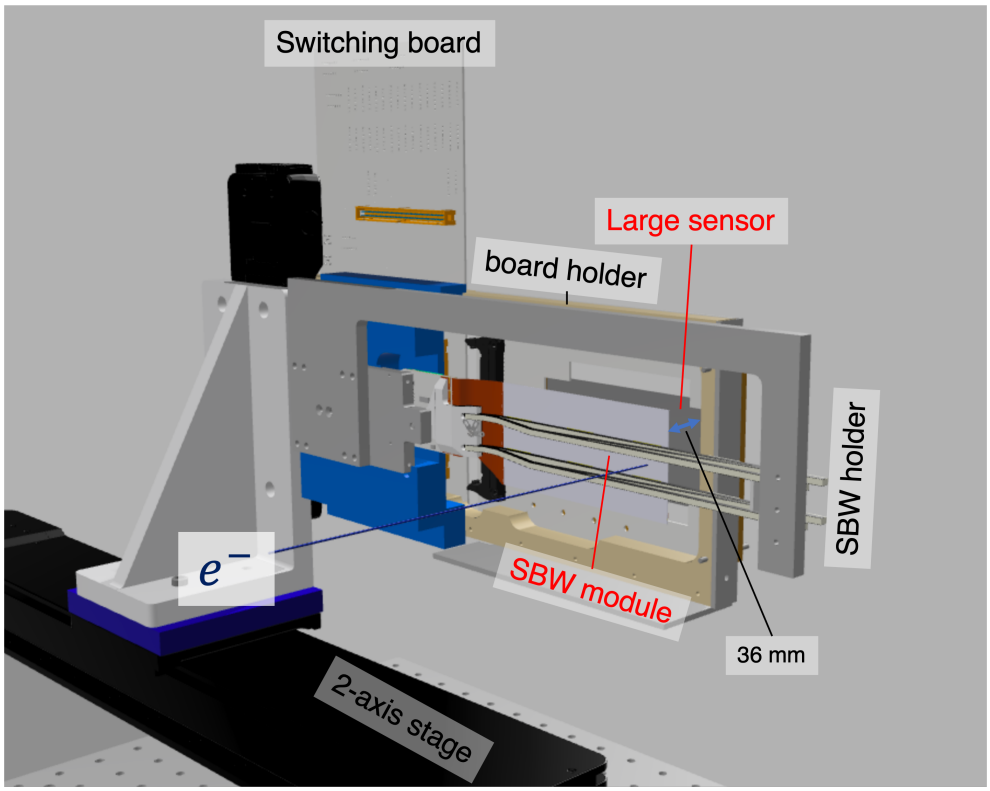

Figure 6.1: The irradiation system for SBW module

6.2 The measurement setup of Charge collection efficiency and noise

To obtain the data output from the SBW before and after irradiation, the system shown in Fig. 6.2 is prepared. The APV25s on the N and P sides of the SBW are connected to the corresponding junction board ports by hybrid cables, and through this junction board, they are connected to a Flash Analog to Digital Converter (FADC). The FADC converts analog signals to digital signals, which are output as digital signals to a readout PC at the latter stage.

The power supply that supplies the drive voltage (LV) of the APV25 and bias voltage (HV) to the sensor is also connected to the SBW via the junction board. The SBW is placed inside a light-shielding box.

With the setup up to this point, we can obtain samples of the pedestal, noise, and calibration curves.

Pedestal Samples the average of raw signals of each strip without the sensor hit [2]; the signal offset. unit:[ADC].

Noise The root mean square of raw signals subtracted by the pedestal of each strip. unit:[ADC].

Calibration curve 1 MIP ($24000e^-$) signal is input to the chip using an internal calibration circuit inside the APV25 chip. The peak height (Cal PEAK) and width of the approximate ideal RC-CR waveform output can be obtained. 1 [ADC] to [e^-] can be converted

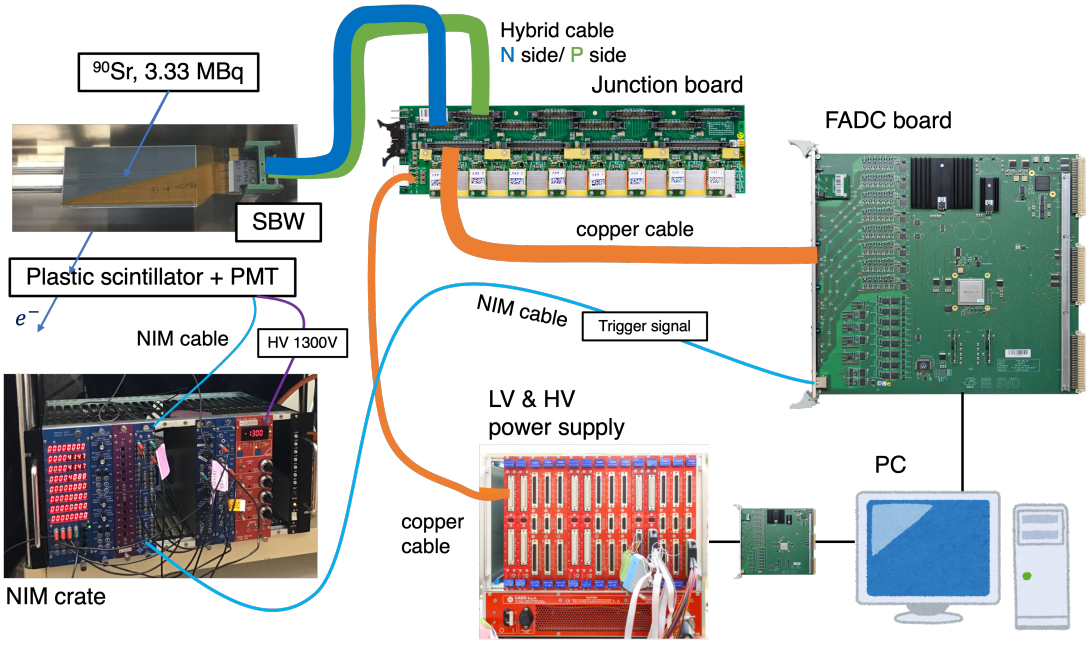

Figure 6.2: The overview of the measurement setup of SBW module

using Cal PEAK;

$$\frac{[e^-]}{[\mathrm{ADC}]} = \frac{1\ \mathrm{MIP} = 24000\,[e^-]}{\text{Cal PEAK}\,[\mathrm{ADC}]}$$

It is mainly related to the value of the interstrip capacitance.

Information on these basic properties of the APV25 is used to calibrate the signals from the sensors.

Next, we describe the setup for the CCE measurement. In addition to the setup described so far, we added a beta-ray source ^{90}Sr (3.33 MBq) to generate charge in the SBW and a system that detects charges when the beta-ray passes through the SBW and triggers the FADC board. The system that detects and sends a trigger signal when the beta-rays pass consists of a plastic scintillator and a Photomultiplier Tube (PMT), which converts the scintillation light emitted from the scintillator into an electrical signal when beta-ray passes through the scintillator, fixed in a holder as shown in Fig. 6.3. During the measurement, 1300 V is applied to the PMT using a separately provided power supply, and the obtained signal is input to the NIM crate through the NIM cable. Since the rate of the signal put into the NIM crate was too high and unacceptable for the FADC as a trigger signal, the rate was adjusted to about 150 Hz in the NIM crate by taking the coincidence of the input signal and the signal width widened to 300 ns by a gate generator in the coincidence module. When the FADC receives this trigger signal, the signal stored in the ring buffer of the APV25 is sent to the FADC, processed by the FADC as a measurement signal, and the data is sent to the PC.

The holder holding the ^{90}Sr and scintillator can be positioned in the two positions (center, edge) shown in Fig. 6.4 concerning the SBW. The geometry relationship of scintillator-SBW-^{90}Sr is written in Fig. 6.5. To confirm the uncertainty to the path length of SBW that comes from its geometry, the area of the scintillator is $w^2 \approx 10 \times 10\,\mathrm{mm}^2$, The window of ^{90}Sr source is 10 mm diameter circle. Distance between them is $L = 70\,\mathrm{mm}$. Since it is not known

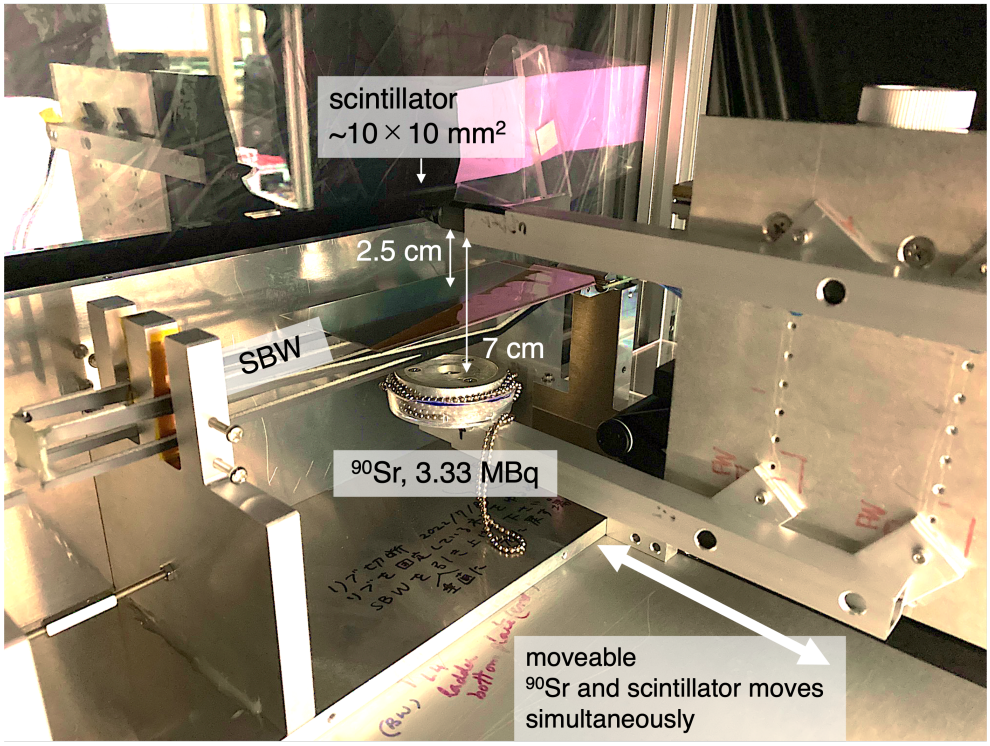

Figure 6.3: The placement of SBW and ^{90}Sr in the light-shielding box

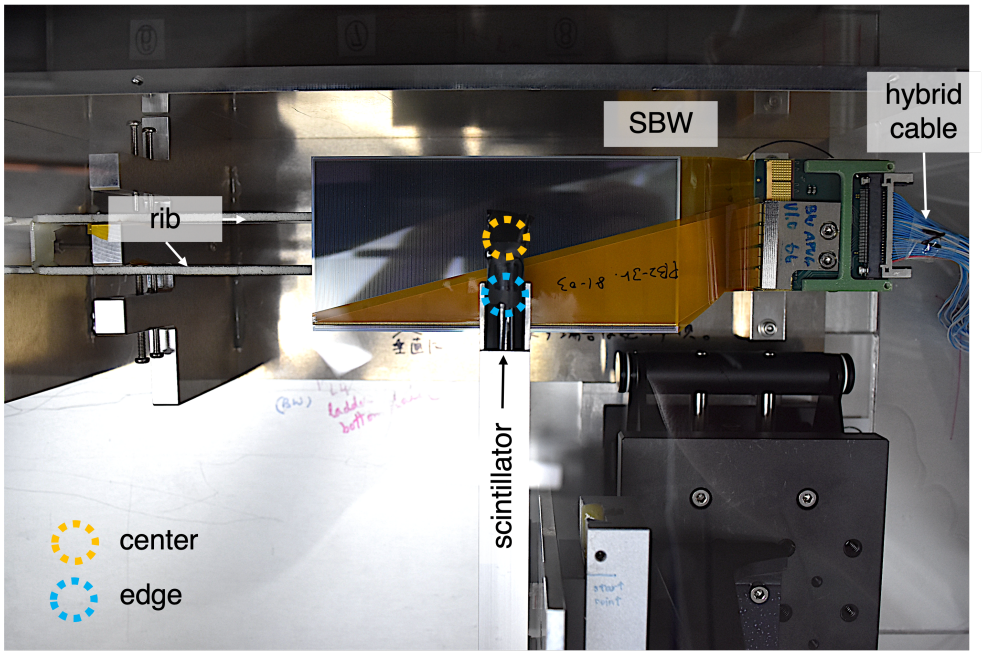

Figure 6.4: The placement of SBW and ^{90}Sr (top view)

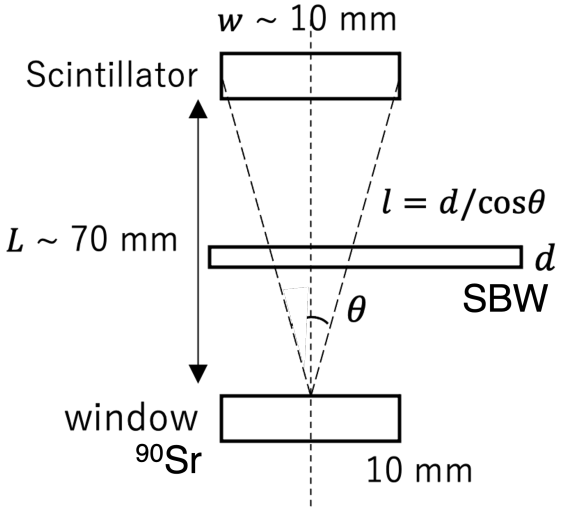

Figure 6.5: Geometry relationship of scintillator-SBW-^{90}Sr

whether ^{90}Sr is actually somewhere in the Sr source window, the calculation is based on the assumption that this is where the maximum peek angle ($\theta = \arctan(w/L) = 0.142$) to the scintillator is located. The path length l that maximizes the path length in SBW with this setting is $l = d\cos(\theta) \approx 0.99$. Therefore, the upper bound of uncertainty for this geometry is $(l - d)/d = 0.01$, which is negligible.

6.3 Measurement procedure of calibration data and charge collection

1. Take a calibration run without an irradiation source at several HV steps; 0.2 to 100 in 10 V increments for this time. Calibration run: (ADC delay, FIR only for HV = 0.2 V), pedestal, noise, internal calibration (Cal PEAK), performed in this order.

   ADC delay find the optimum delay time of the FADC system concerning the timing of sampling clock frequency (31.75 MHz for this time). This value will not be affected by the HV changes, it is done only for the first measurement (HV = 0.2 V)

   FIR Finite Impulse Response, obtain the coefficient of a digital filter; FIR filter to compensate the distortion in the frequency dependence function loss of cable and suppress the effect of reflection in the cable due to the impedance changes. It will occur in the transmission between APV25 and FADC. Same as ADC Delay, only performed for the first time (HV = 0.2 V)

   Pedestal, Noise, Internal calibration As mentioned in the previous section. (Internal calibration refers to calibration curve), performed every HV step.

2. Set the radiation source and trigger system as shown in Figure fig 6.3 and make the trigger signal can be input to the FADC. Here, since the timing of the trigger and the timing of the acquired waveform may differ, the latency time of APV25 should adjust so that the beta ray hit can be included in the data frame.

3. Check the hit map and adjust the relative positions of the sensor and scintillator with ^{90}Sr . Take data at HV steps; 0.2 to 100 in 10 V increments for this time, and the

calibration data for the respective corresponding voltages obtained in step.1 is applied to the measurement data.

6.4 The result of measurement without ^{90}Sr before and after irradiation test

Changes in data for the calibration data without source are shown here. The estimated V_{FD} of SBW: 53 V (before), 51 V (after). These values were estimated in the same way as for the large845 sensor. The measurements in this section and the next section were taken after 1×10^3 hours after irradiation, so the results include the annealing effect.

Fig. 6.6 shows the noise of SBW changes before and after irradiation. The P side strips between $250 \sim 500$ show higher noise than before irradiation. This area coincides with the irradiated area, suggesting that the noise increased by $\approx 400\,[e^-]$ due to the radiation damage.

On the other hand, on the N side, noise is generally lower after irradiation in the region of $V < V_{\mathrm{FD}}$, and conversely higher before irradiation in $V > V_{\mathrm{FD}}$. In addition, for $V > V_{\mathrm{FD}}$, both sides plateau with respect to V, irrespectively to whether it is before or after irradiation, refer to Fig. 6.7 which picked up one strip to see the noise vs. bias voltage. When compared to the region of the plateau, the after irradiation region is $300\,e^-$ higher.

We can observe that one of the N side strips has a very large noise after irradiation, which was not observed before. We suspect a pinhole is occurring in that strip and are currently investigating. A pinhole is a breakage of the AC decoupling capacitor between the implant and the readout strip aluminum inside the sensor bulk, it leads to some unexpected current flow into the APV25 and the amplifier possibly cannot work correctly; becomes a single defective strip on the sensor.

Make a comparison with the ENC calculated from the leakage current and the interstrip capacitance of the large845 as the previous chapter calculation. The before and after results for both SBW and large845 are summarized in Fig. 6.8. Although the two sensors are different, they use the same type of large sensor, so their properties and behavior are expected to be similar. The figure illustrates that the noise measured before and after irradiation is close to the large 845 noise calculated using leak current and $\mathrm{C_{int}}$. The leak current and $\mathrm{C_{int}}$are expected the primary causes of the noise. The discrepancy between the calculated noise of large845 and the noise measured by SBW is not only due to the fact that the two sensors are different. The difference between the two values may be due to the fact that the large845's noise includes not only interstrip capacitance but also parasitic capacitance and resistance from other parts (pitch adapter, etc.), whereas the large845's measurement does not consider these effects except the leakage current and the $\mathrm{C_{int}}$. The difference between the two values is possibly due to this fact.

On the other hand, there is no change in the pedestal as shown in Fig. 6.9. The pedestal is due to the DC offset on the APV25 input, which is not changed by radiation damage, as expected. The results of the Cal PEAK change are summarized in Fig. 6.10. The Cal PEAK on the P side has a slightly lower value after irradiation when $V < V_{\mathrm{FD}}$, but by increasing the voltage, it approaches the value before irradiation. Especially when $V > V_{\mathrm{FD}}$, there is no significant difference in value. For Cal PEAK on the N side, when $V < V_{\mathrm{FD}}$, the value after irradiation is slightly higher than the value before irradiation, but by increasing the voltage in the same way as on the P side, the value approaches the value before irradiation.

We will primarily focus on the results of the Noise and Cal PEAK measurements. We first

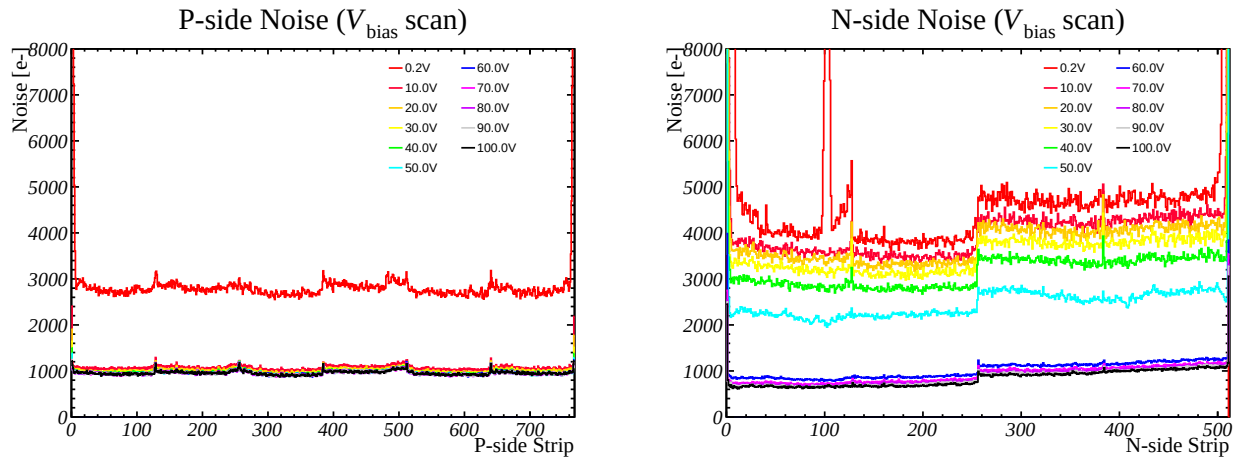

(a) before

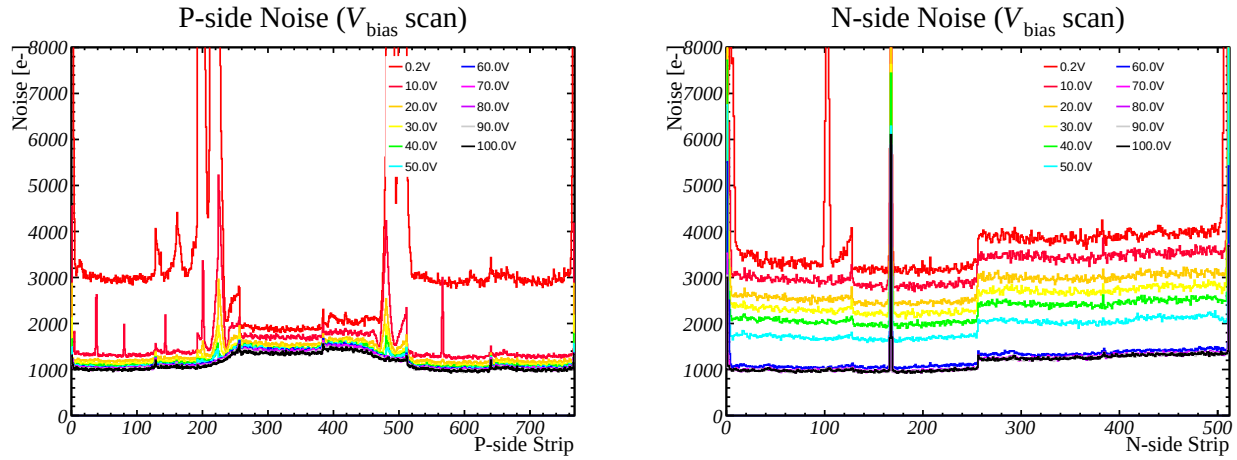

(b) after

Figure 6.6: The Noise changes; P strips (left), N strips (right). Colored with applied HV bias voltage.

begin, to examine the results obtained before irradiation, when the depletion layer spreads from the P-side to the N-side of the sensor. At this stage, the P-side strip is prone to depleted around the interstrip at low bias voltages, regardless of the V_{FD} . As a result, we expect the noise and Cal PEAK values on the P side to plateau at low bias voltages. In contrast, the depletion layer does not reach the N side strip until the applied bias voltage equals the V_{FD} . Therefore, the Noise and Cal PEAK values on the N side are expected to plateau at $V = V_{\mathrm{FD}}$. Our observations are consistent with these expectations. Specifically, we found that on the P side, the Noise and Cal PEAK values plateaued at bias voltages of 10V and above. On the N side, we observed that these values plateaued at a bias voltage of 60 V, which is above the V_{FD} value.

The IV measurement of irradiated SBW suggests that the type inversion has occurred in the SBW irradiated region after irradiation, i.e., the depletion layer is spreading from the N side to the P side as the N type bulk becomes P type. Therefore, we expect that the Noise

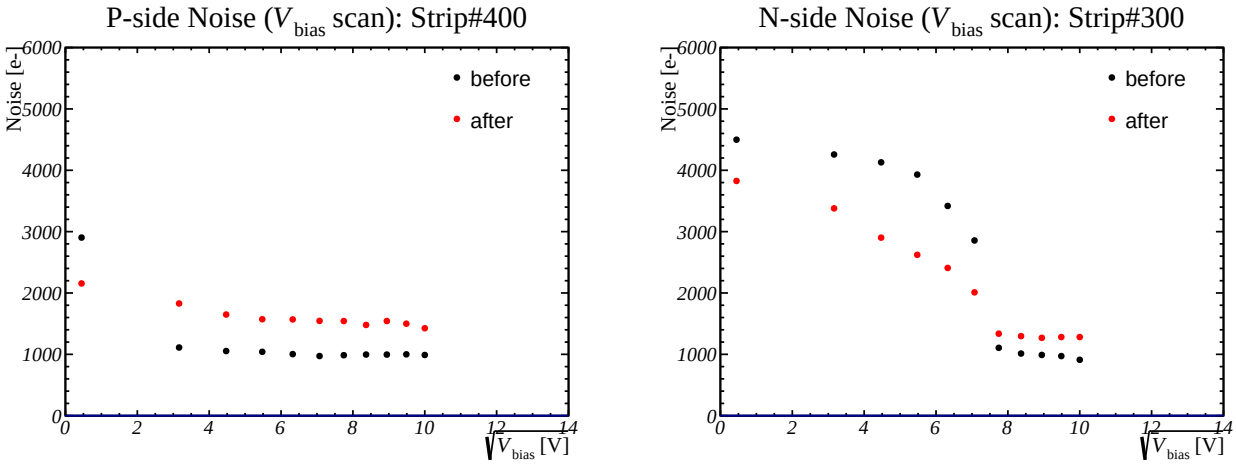

Figure 6.7: The comparison of the noise of one picked-up strip from the irradiated region before and after the irradiation.

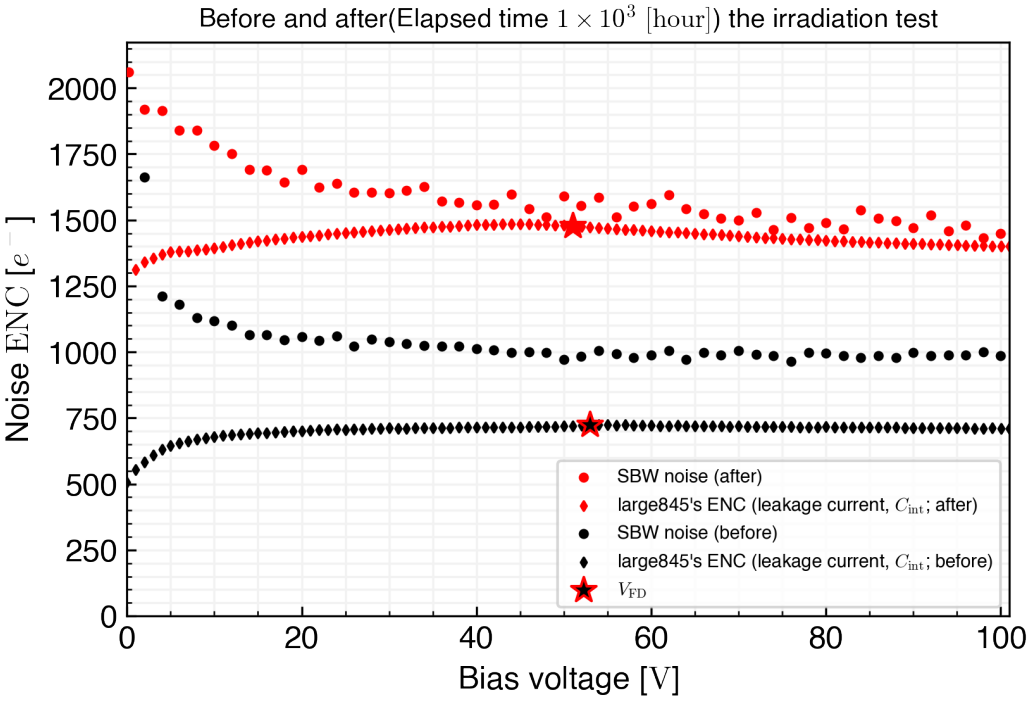

Figure 6.8: The comparison of ENC calculated from Large845 leakage current and C_{int}, and ENC measured at SBW

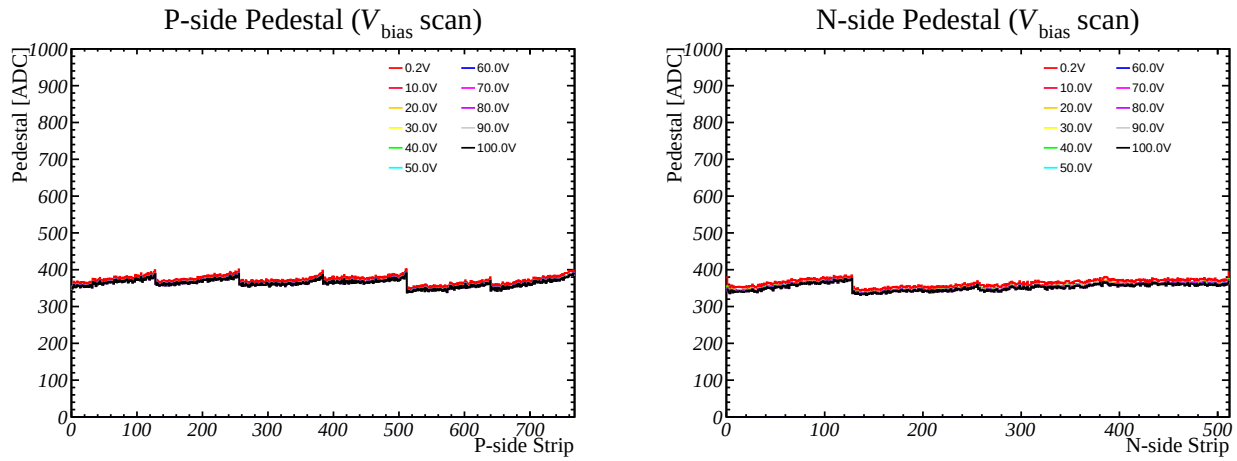

(a) before

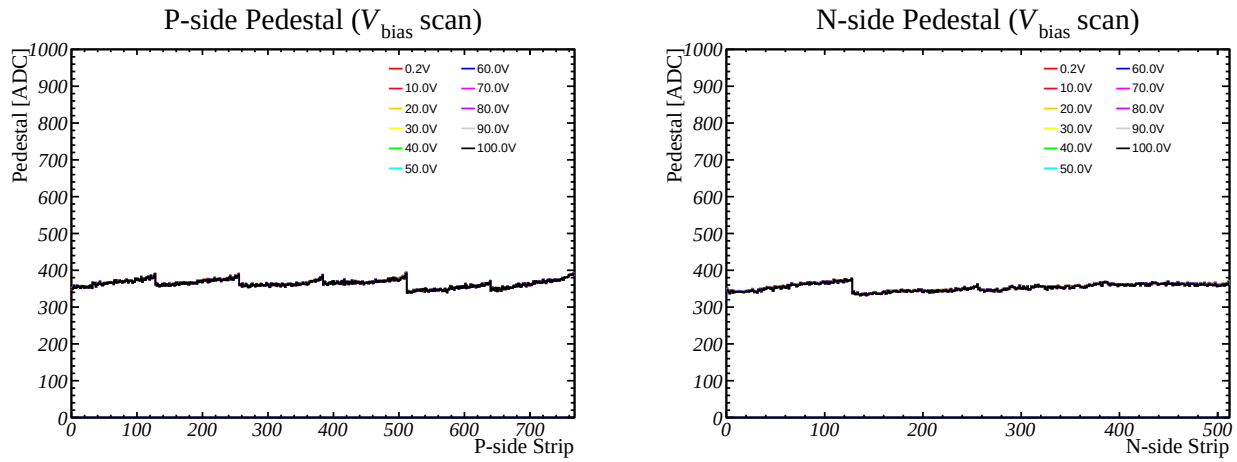

(b) after

Figure 6.9: The pedestal changes

and Cal PEAK values on the N side will plateau immediately, while on the P side they will plateau at V=Vfd. However, it is worth noting that in this study, only a portion of the N side strip was irradiated, so the type inversion only occurred in that portion while the unirradiated portion remained unchanged. This means that the observations regarding the N side described above are impossible to be seen.

Examination of the Noise vs bias voltage results after irradiation revealed an unexpected trend on the P side, where there was no discernible structure related to the V_{FD} . Instead, the values are expected to gradually decrease and approach the plateau from the outset. On the N side, the plateau was observed at the same location as before irradiation, which we attribute to the influence of the unirradiated region.

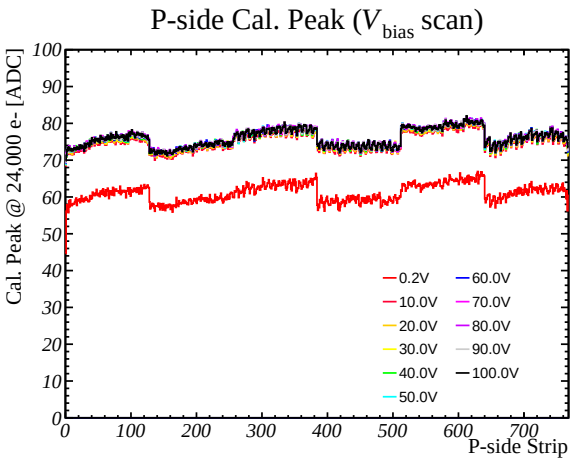

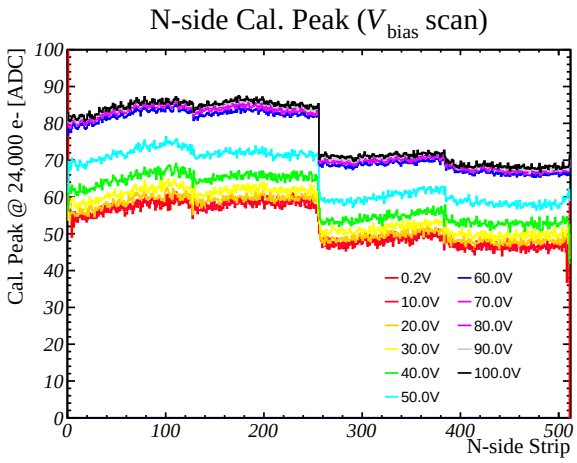

(a) before

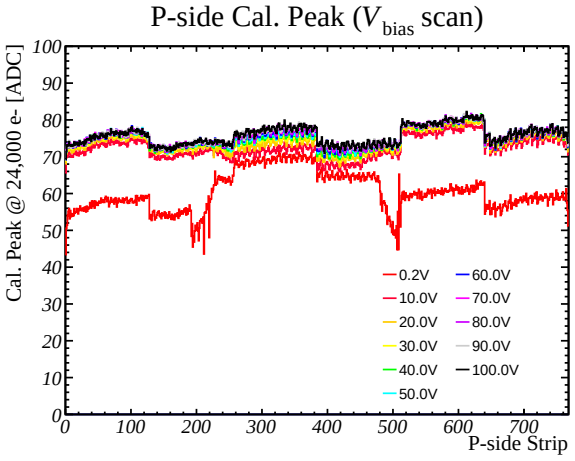

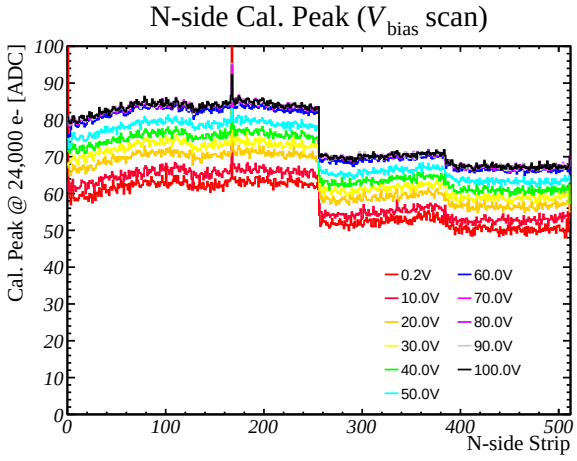

(b) after

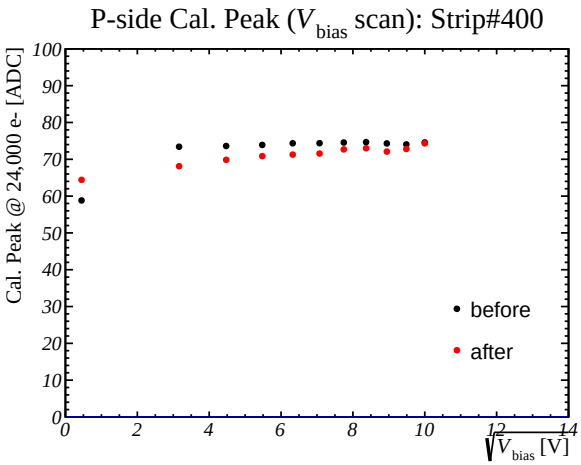

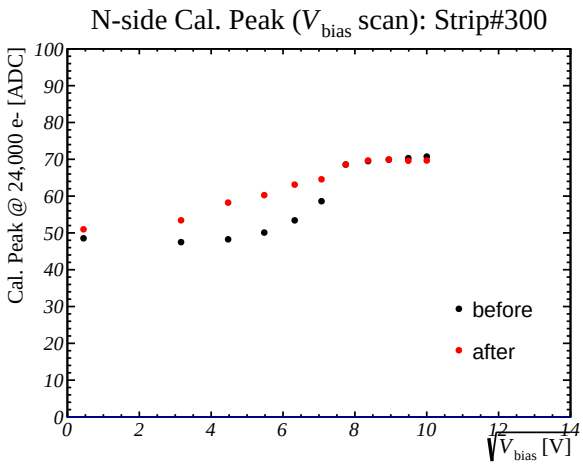

(c) Picked one strip up from irradiated region

Figure 6.10: The CalPEAK changes

6.5 Charge collection measurement

6.5.1 Particle traversed position finding algorithm (Cluster finding algorithm)

The word 'Cluster' is used for the hit of the beta passage; the Cluster finding algorithm is equivalent to searching for the signal due to the beta ray passage. The following is a description of this finding algorithm. First, to discriminate between noise and signal, we look for a strip with Signal-to-Noise Ratio (SNR) > 5; where the strip signal is 5 times the strip noise (called cluster seed). Then, we search for left and right from an adjacent strip of the seed to find strips with SNR > 3 or higher. An event that meets this condition is called one cluster, and the number of strips plus one seed strip define as the cluster size. Fig. 6.11 is an illustration of cluster size. This algorithm is also used for Belle II SVD official clustering.

In addition, Cluster charge is defined as the total amount of charge of the cluster, and Cluster SNR is defined as Cluster SNR $\equiv$ (Cluster charge $[e^-]$)/($\sqrt{\sum_{i\in\text{cluster}} \text{Noise}_i{}^2}\,[e^-]$).

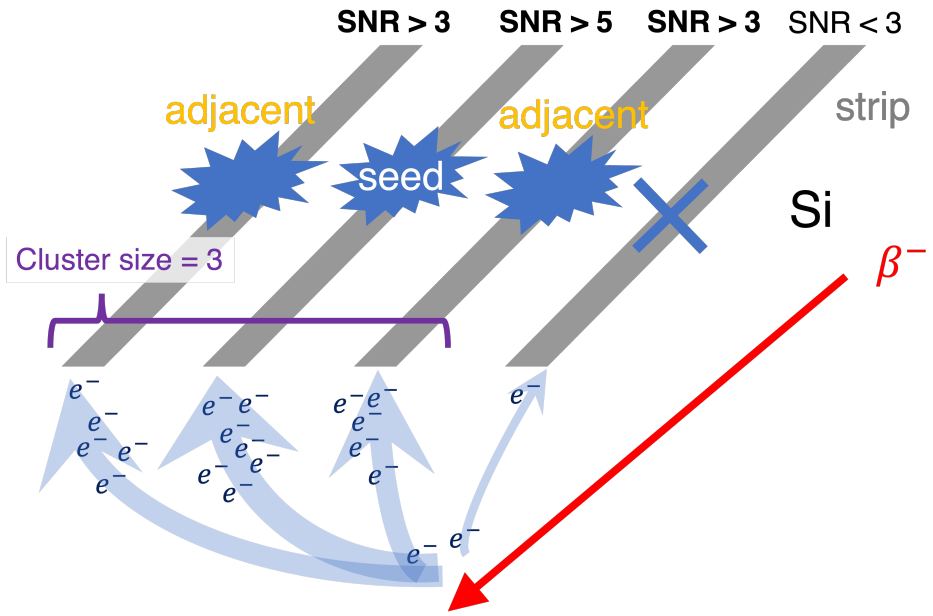

Figure 6.11: The image of Cluster finding, cluster size is 3 in this case

6.5.2 Result of measurement with ^{90}Sr before and after irradiation test

Next, we present the measurement results for the cluster event using ^{90}Sr as the β ray source. The data were collected using a sample size of 2.6 million events at a nominal bias voltage of 100 V, and 300 thousand events were acquired at each 10 V increment from 0.2 V to 100 V for the before irradiation and up to 160 V for the after irradiation. Since the counting distribution of the number of events can be assumed to be Poisson distribution, the error can be considered as $\sqrt{\text{Number of events}}$, and in this case, since Number of events $\gg \sqrt{\text{Number of events}}$, the error in the number of events can be ignored. The following figures without descriptions of voltages are measured at nominal voltage; 2.6 million events. First, To review the hit positions

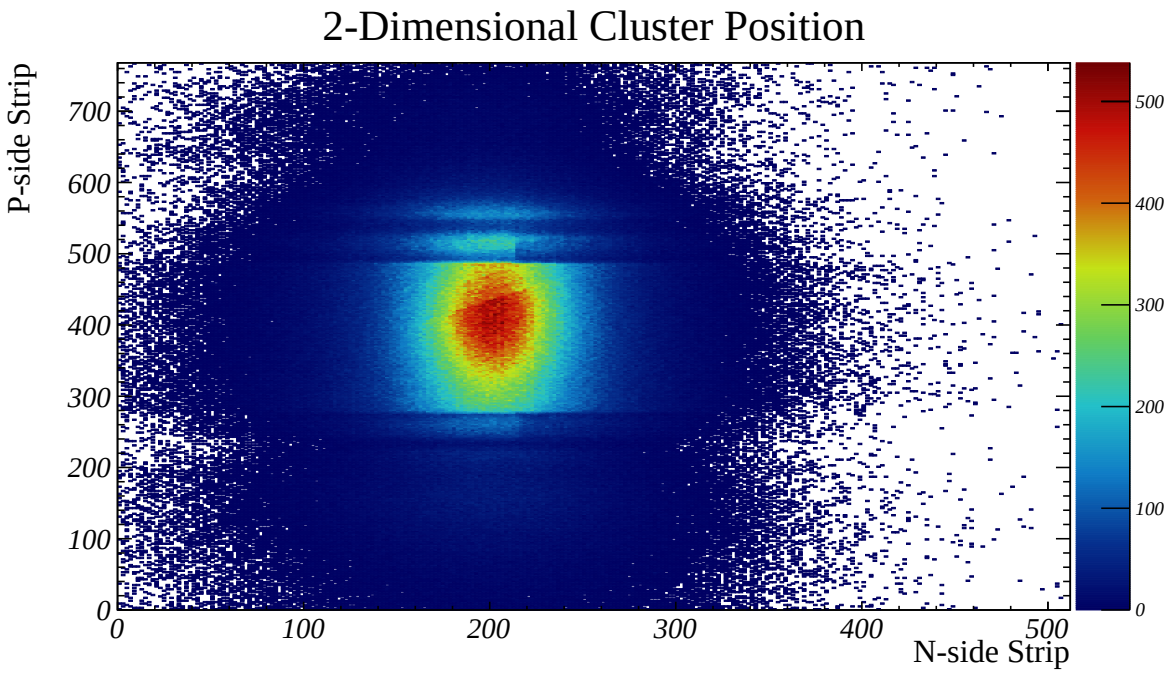

(a) before irradiation

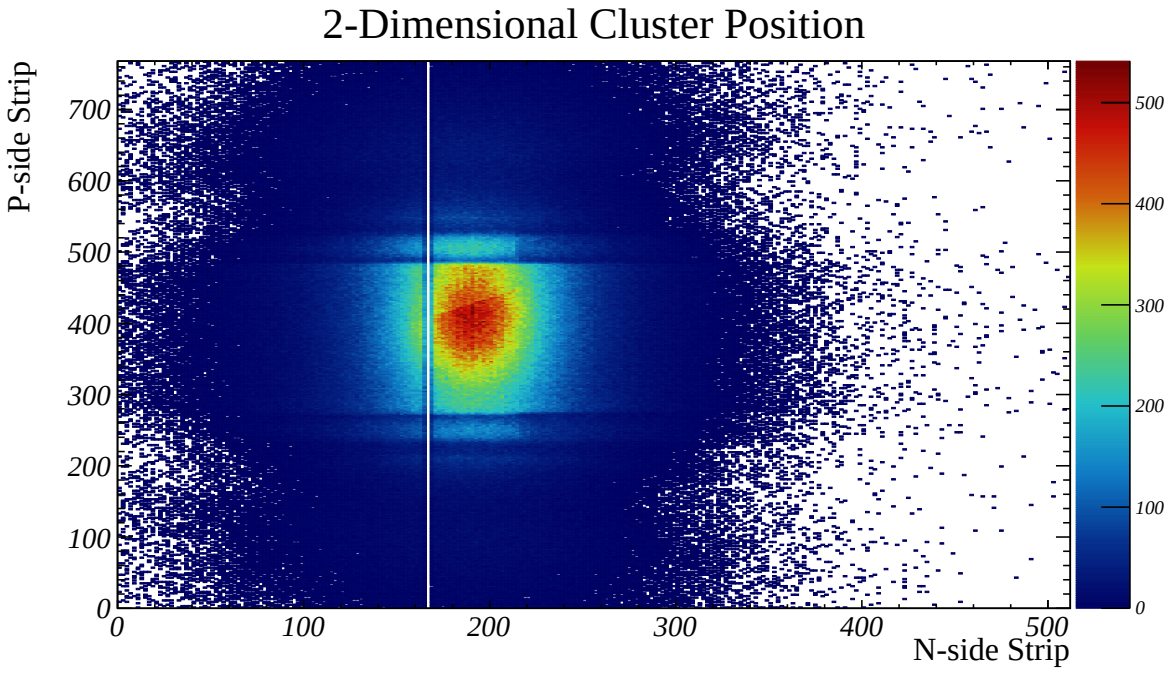

(b) after irradiation

Figure 6.12: 2-D Cluster position (hit position) map with β^- ray. Axis unit: strip number. Colored with the hit count

and entries at the location before and after irradiation, shown in Fig. 6.12. Using the collected charge Q_i and strip position x_i of each strip as in the center-of-gravity method, we define the hit position as

$$\text{hit postion} = \frac{\sum_{i\in(\#\text{strips})} x_i Q_i}{\sum_{j\in(\#\text{strips})} Q_j} \quad . \tag{6.1}$$

The location where the hit count is high coincides with the location where the source is placed. In the after irradiation results, there is a single white line present, which is considered to be the pinhole mentioned in the previous section. Data cannot be obtained from this strip due to the suspected presence of a pinhole. Furthermore, both before and after irradiation, there are horizontal lines indicative of low-count areas in the $200 \sim 300$ and $500 \sim 600$ regions. This part corresponds to the ribs that support the large sensor of the SBW (see Fig. 6.13).

The rib is made of polymeric foam (AIREX R82.60) sandwiched by a carbon fiber sheets. The black part of the rib in Fig. 6.13 corresponds to the carbon fiber sheet. Check the number

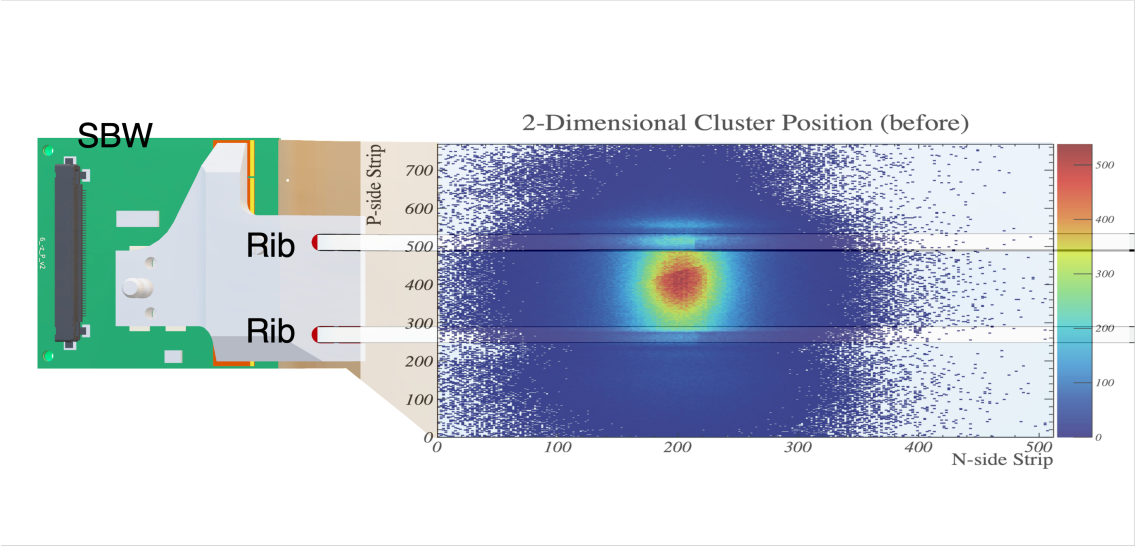

Figure 6.13: SBW 3D model and hit position map overlay

of clusters. Here, all clusters, the clusters on the N and P sides alone are plotted in Fig. 6.14.

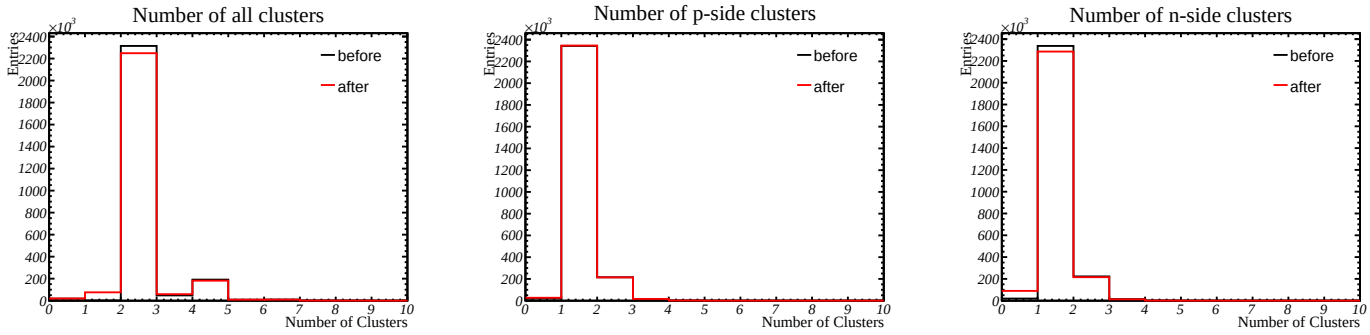

Figure 6.14: number of clusters changes before and after irradiation

Let $i, j = 0, 1, 2, \ldots,\ \ k = 1, 2, \ldots$ be the number of clusters respectively, the relationship between the hit entries of all clusters all_k, P clusters p_i, and N clusters n_j can be expressed as follows;

$$\mathrm{all}_k = \sum_{k=i+j} n_i + p_j, \quad n_i + p_j \neq 0 \tag{6.2}$$

The results show that the entries are dominant at $i, j = 1, 2$ before and after irradiation. $i, j = 2$ is possible because two particles passed through at the same time in the same data frame.

The number of cluster distributions on the P side did not change before and after irradiation, but on the N side, n_0 increased slightly and n_1 decreased by 500 [entries]. Since this change in entries occurs only on the N side, it can be attributed to the aforementioned pinhole issue. In conjunction with this, as N_1 decreased, all_1 increased and all_2 decreased.

Next, now that the number of clusters has been confirmed, we check the distribution of their cluster size. The cluster size distribution change of each side of the sensor is shown in Fig. 6.15.

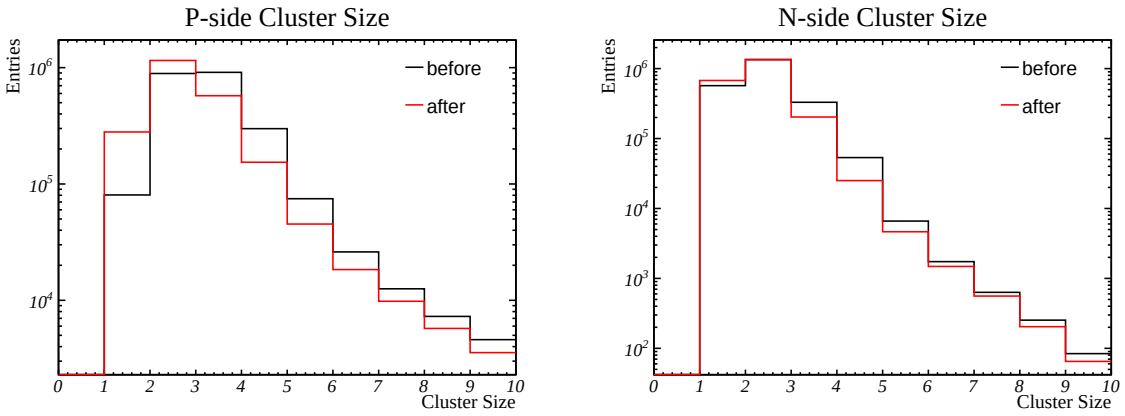

Figure 6.15: Cluster size changes before and after irradiation

The results show that the number of clusters with cluster size ≥ 3 on both sides is decreasing. This trend is more pronounced on the P side, while the number of clusters with cluster size $= 1$ and 2 is conversely increasing.

This trend of the cluster size distribution can be confirmed by focusing on the irradiated area and the area with the highest β rays hit entries; the area where the vertical incidence of beta rays can be expected, to exclude the effect from the non-irradiated area. See Fig. 6.16, the selected area: ; P side strip $\in$ [368, 432), N side strip $\in$ [160, 240).

Since there is no significant difference in the total number of clusters, it simply means that the number of clusters with large cluster size is decreasing. There are two possible reasons for this;

1. The decrease in CCE of each strip has reduced the number of adjacent strips that match the cluster finding algorithm.

2. The increase in noise for each strip no longer satisfies the SNR > 3 that the cluster finding algorithm imposes on adjacent strips.

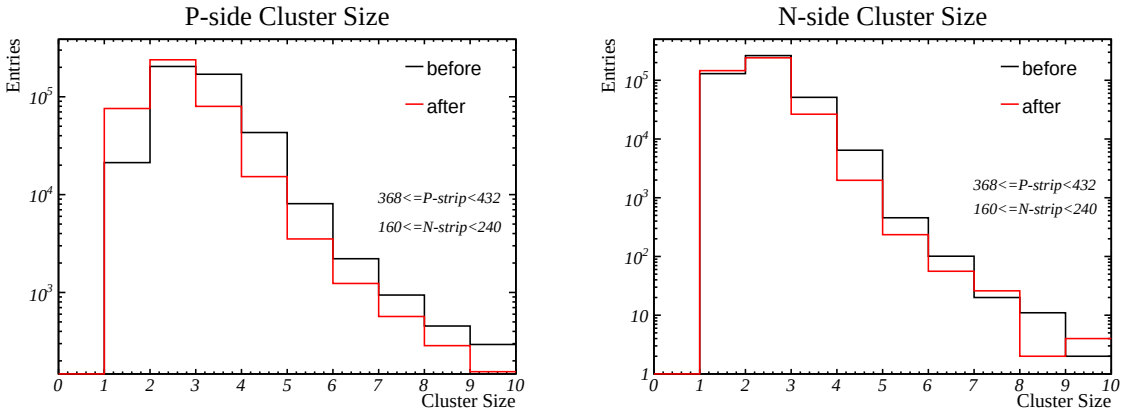

Figure 6.16: Cluster size in selected region changes before and after irradiation

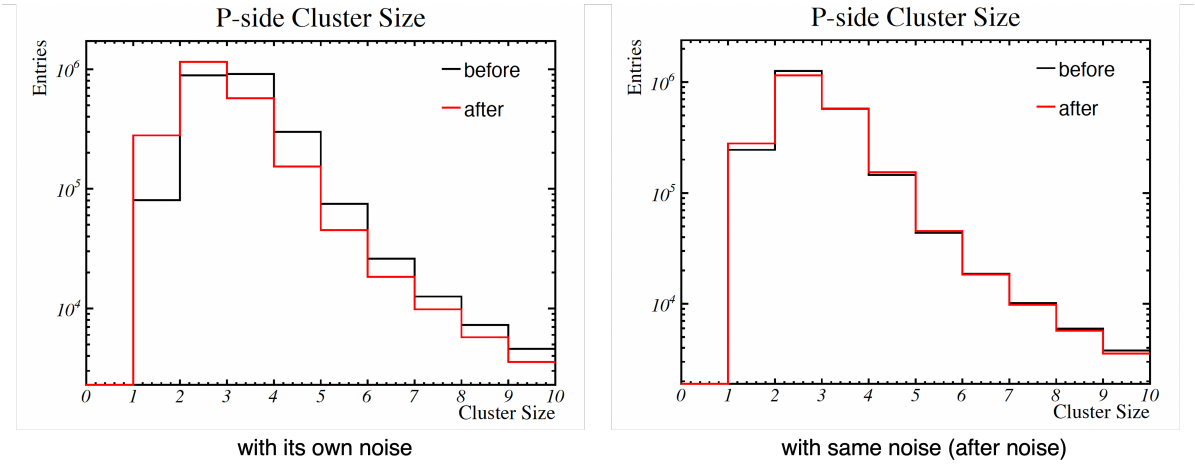

Figure 6.17: The cluster size of P side changes, the result of after Irradiation with after irradiation noise data (left, as shown in the previous figure), assuming same noise calibration data; after irradiation noise data (right; both use same noise)

The increase in the noise has already been seen in Fig. 6.6. To check how much the cluster size is reduced by this increase in noise, we assume that the noise before irradiation is the same as the noise after irradiation and calculate the cluster size again; using the same noise calibration data to compare. The result of the P side is shown in Fig. 6.17.

The results indicate that altering the noise to the noise data before irradiation significantly diminished the difference in cluster size distribution between before and after irradiation. This also can be confirmed in the selected area of the SBW. In addition, it suggests that there is possibly no change significant in the CCE.

On the other hand, it is difficult to discuss the N side at this time because it is non-uniformly irradiated on the N side strips and a pinhole issue is suspected.

Since the cluster size of one, two and three are dominant in the cluster size distribution, we examined the cluster charge (collected charge) distribution included in each cluster size (1, 2, all cluster sizes). The distribution changes are shown in Fig. 6.18. Here we focus on the

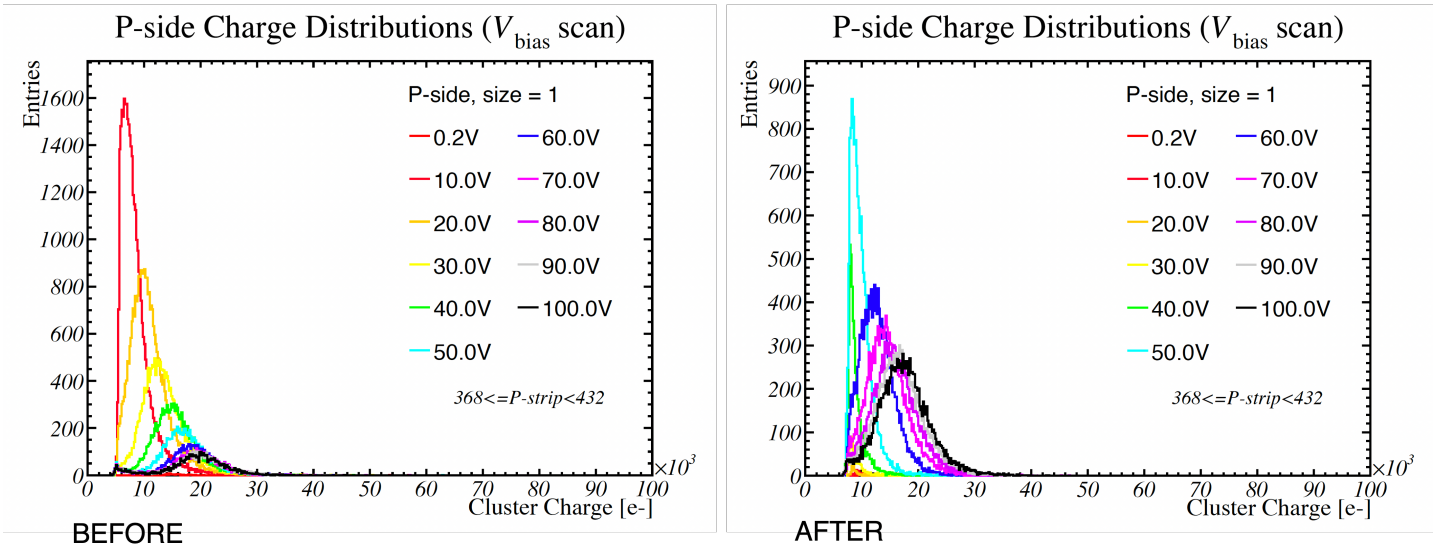

Figure 6.19: The cluster charge distribution of P side in the selected area with difference voltages before (left) and after (right) irradiation (cluster size = 1)

aforementioned selected. The distribution of the sensor as a whole is close.

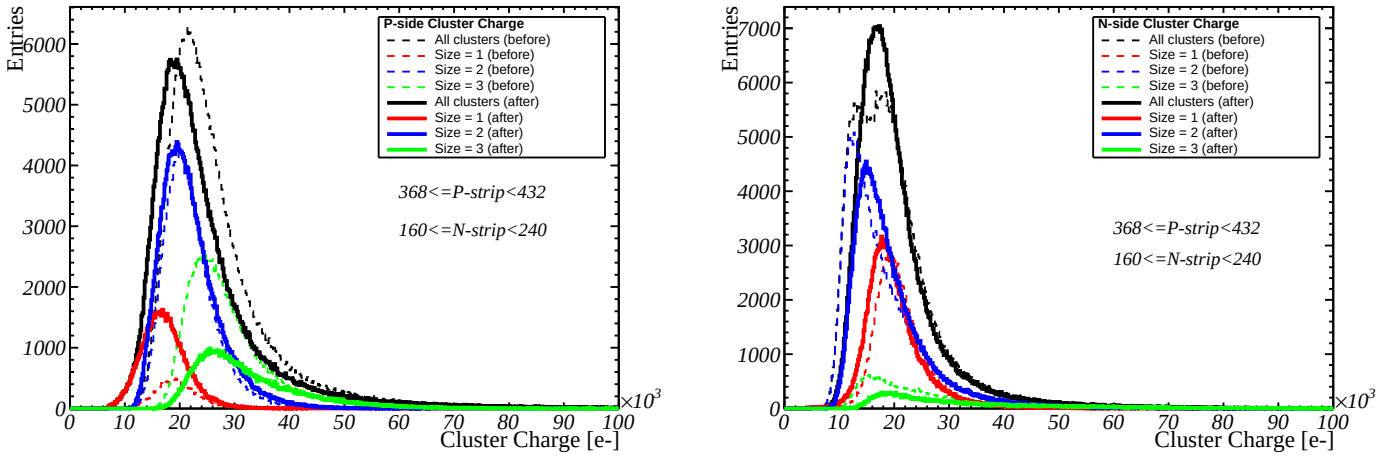

Figure 6.18: The cluster charge distribution in each cluster size before (dashed line) and after irradiation (solid line), left: P side, right: N side, selected area: P side strip $\in$ [368, 432), N side strip $\in$ [160, 240)

All peaks of cluster charge distribution are near 20 ke^-, The peak of the distribution with cluster size = 1 on both the N and the P sides decreased after irradiation, from 19 ke^- to 17 ke^- for the P side, from 19 ke^- to 18 ke^- for the N side. While the peak of the distribution of the N side with cluster size $\geq$ 2 became higher after irradiation.

The following shows the cluster charge distribution measured at different voltages. Correction data measured at the same voltage independently before and after irradiation are used to

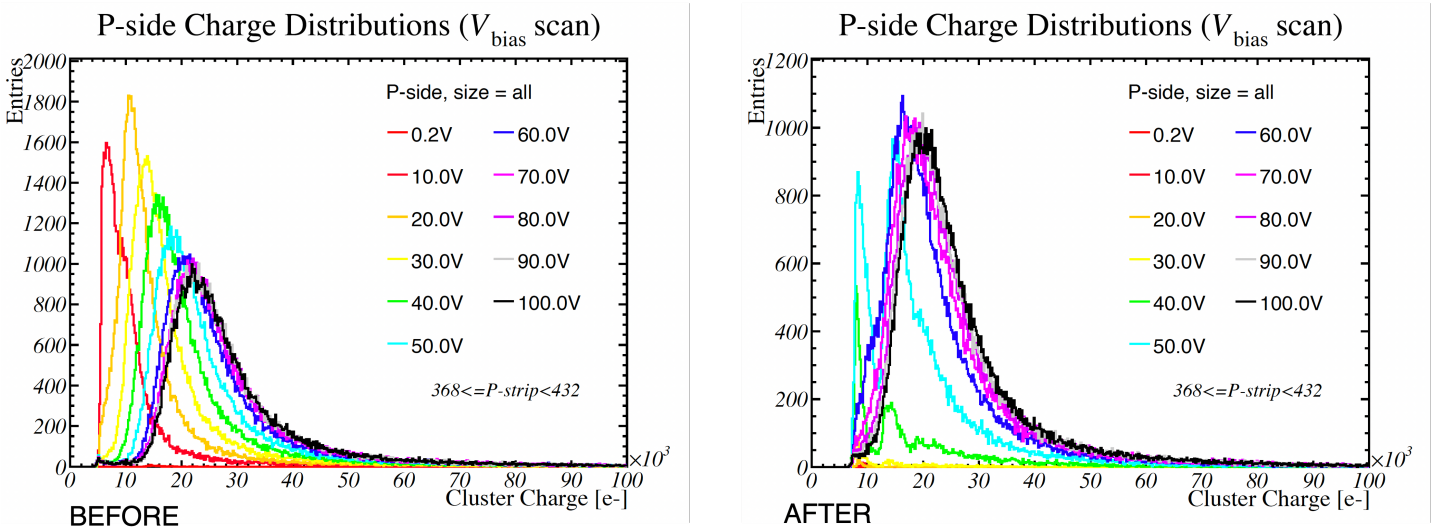

Figure 6.20: The cluster charge distribution of P side in the selected area with difference voltages before (left) and after (right) irradiation (cluster size = all)

correct the measured data for each voltage. Here we shall discuss the P side. In addition to that, the discussion is focusing on the cluster size = 1 and 'all cluster' events. The results of the cluster size = 1 are shown in Fig. 6.19 and Fig. 6.20.

Although the number of entries differs, it can be confirmed that the peak of the cluster charge distribution is proportional to the voltage, even when the cluster size is 1 or 'all'. Furthermore, in the region where V exceeds V_{FD} , the peak shift is slower.

Meanwhile, the distribution below 50V after irradiation was cut off by zero suppression (SNR $>$ 3; cut to reduce the amount of data in the event, the criteria is the same as Belle II official one.) because the noise increased due to irradiation, which is either not visible or not visible at all. The peak is clearly visible after 60 V, which is the region beyond V_{FD} . However, the position of the peak has shifted significantly compared to before irradiation, moving about 10 ke^- from 60 V to 100V.

Here, fitting is performed for each distribution in order to quantitatively evaluate the peaks. The clustered charge collected by the silicon strip sensor is related to the energy loss of the β ray traversed. It can be evaluated with Gaussian convoluted Landau distribution function [5]. Thus we used the function to fit the cluster charge distribution with ROOT; a software widely used in the high-energy physics field for analysis. Fitting parameters were adjusted visually. The peak of the fitted curve is called the 'Most Probable Value (MPV)'.

The Charge MPV vs bias voltage is shown in Fig. 6.21 for cluster size = 1 and Fig. 6.22 for cluster size = 'all'. As mentioned above, there is a voltage that does not peak after irradiation due to the zero suppression cut. The MPV of that voltage is not considered in the plot.

The results of both cluster sizes confirm that the MPV increases in proportion to voltage and the maximum value of MPV decreased from 20 ke^- to 18 ke^- (10%) for cluster size = 1, from 22 ke^- to 20 ke^- (10%) for cluster size = 'all' before and after irradiation. The voltage at which the MPV changes to a plateau with respect to voltage is 70 V before irradiation and nearly 100 V after irradiation. However, the MPV after irradiation still appears to be slightly increasing.

We should note that results in Fig. 6.21 and Fig. 6.22 cannot be immediately evaluated as changes in CCE, as mentioned in Fig. 6.17, it is possible that the peak of the cluster charge distribution, i.e., MPV, may change after irradiation due to an increase in noise, which may be cut by the SNR criterion. To investigate this, we calculate the MPV assuming the same noise as in Fig. 6.17. Fig. 6.23 and Fig. 6.24 show the results of calculations assuming the same noise before and after irradiation.

Comparing Fig. 6.23 and Fig. 6.24, calculated with the same noise, and Fig. 6.21 and Fig. 6.22, calculated with the different noise, respectively, there is still a difference in MPV before and after irradiation comparing the same voltage before and after irradiation, but the difference is smaller when the noise is aligned. For example, if we look at cluster size=1, 100 V, the difference is $3\,\mathrm{k}e^-$ ($20\,\mathrm{k}e - 17\,\mathrm{k}e^-$) when the noise is each own noise, but $2\,\mathrm{k}e^-$ ($19\,\mathrm{k}e^- - 17\,\mathrm{k}e^-$) when the noise is the same. Also, when comparing the maximum MPV values for each, the difference is less than $500\,e^-$. This is confirmed by the fact that the SNR criteria were tightened due to increased noise, which resulted in many charges not being collected as clusters. In addition, since there is no significant difference in the number of hits when noise is aligned from Fig. 6.17 for any cluster size, Fig. 6.23 and Fig. 6.24 can be considered as the difference in the CCE. And while CCE is indeed lower at the same voltage before and after irradiation, by applying a sufficiently high voltage, CCE recovers to the pre-irradiation level. The CCE before irradiation has a voltage near V_{FD} and the change plateaus but after irradiation the voltage plateaus at a much higher position ($\sim 100\,\mathrm{V}$) than the expected V_{FD} , and still increased slightly.

We have a possible interpretation: It is thought that the sensor bulk after 100kGy irradiation undergoes type inversion and becomes P type bulk. Therefore, the depletion layer expands from the N side to the P side. The V_{FD} defined by our current IV curve is thought to pick up the structure of the IV curve that appears when the depletion layer touches the P side strip, and it is thought that there is still a part of the depletion (especially between strips) around the P side strip. As a result, at that point, the P strip has a mixture of depleted and undepleted regions and generates a complex electric field, causing the CCE to decrease. As the voltage is increased, the undepleted region decreases and the electric field becomes orderly, gradually increasing the CCE.

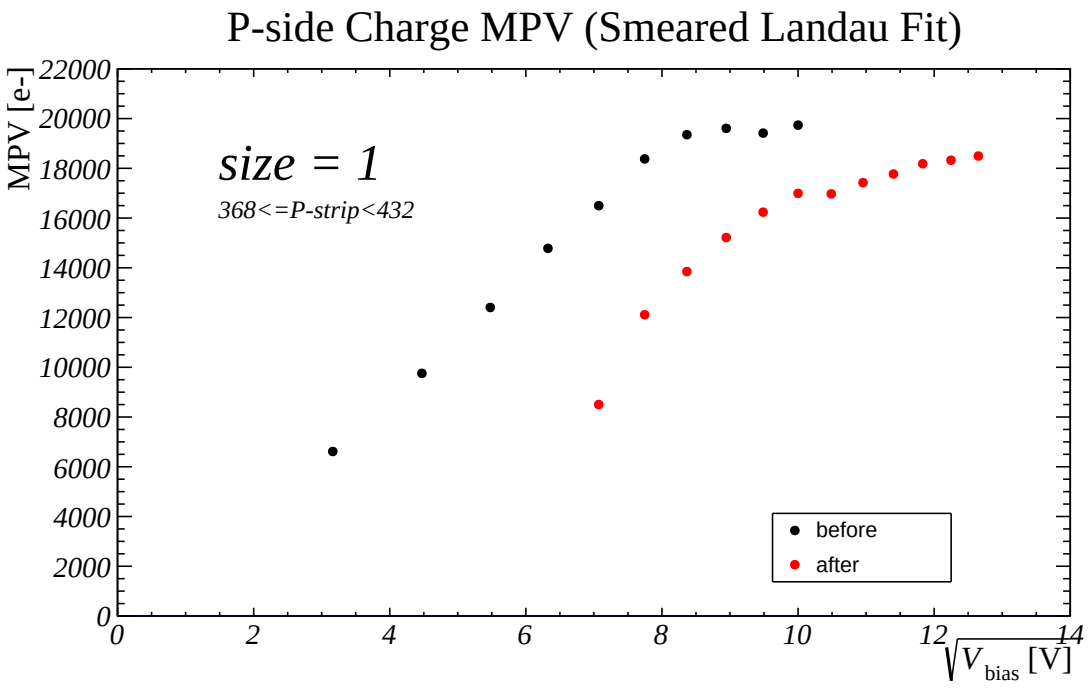

Figure 6.21: Most provable value change in the selected area before and after irradiation (cluster size = 1)

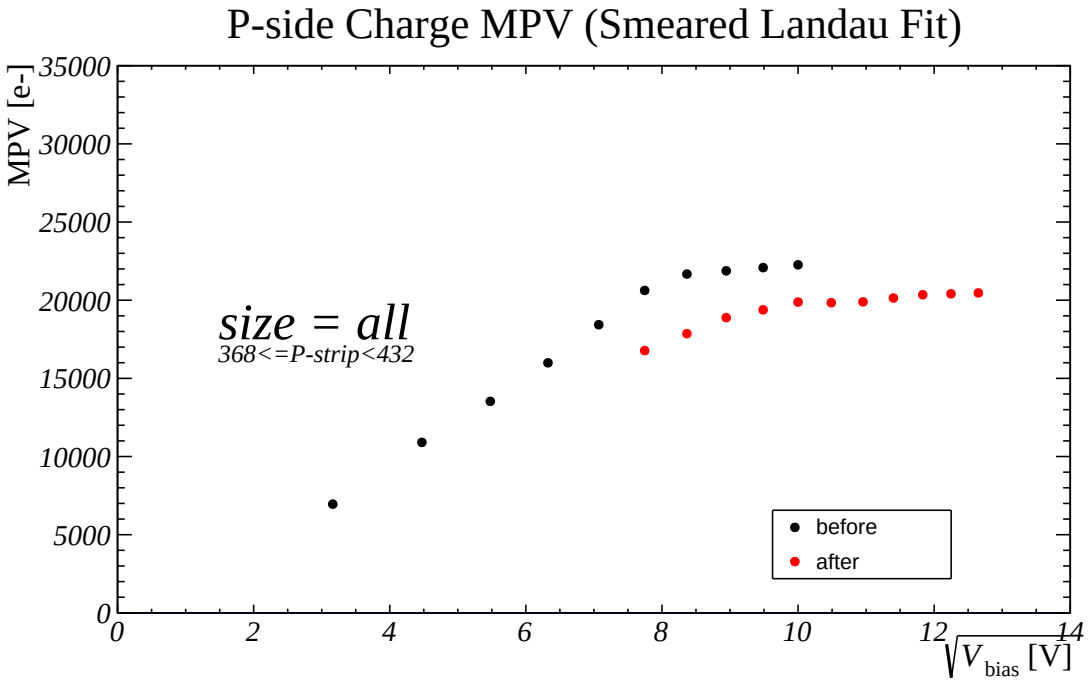

Figure 6.22: Most provable value change in the selected area before and after irradiation (cluster size = 'all')

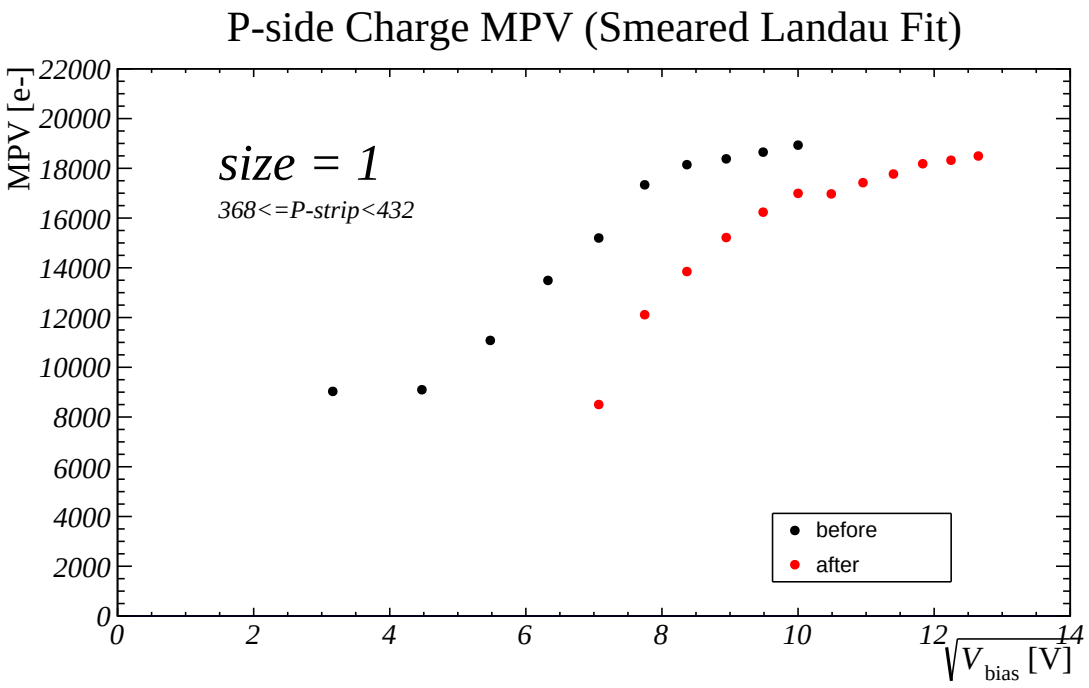

Figure 6.23: Most provable value change in the selected area before and after irradiation, with using same noise calibration data (cluster size = 1)

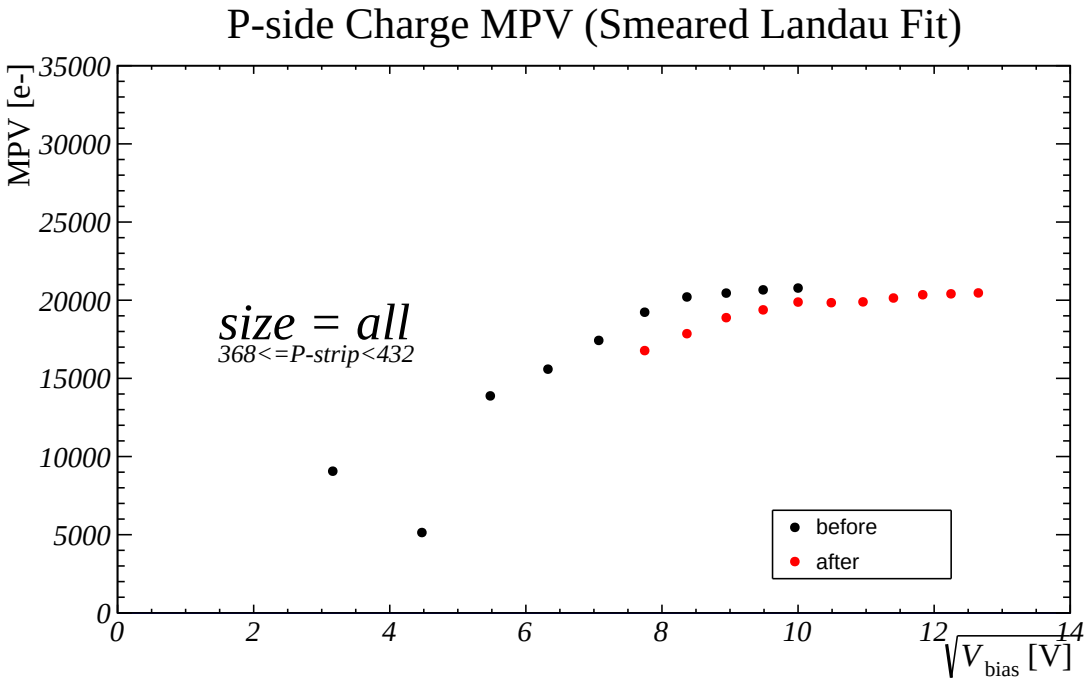

Figure 6.24: Most provable value change in the selected area before and after irradiation, with using same noise calibration data(cluster size = 'all')

Chapter 7

Conclusion

In pursuit of understanding the fundamental nature of the universe beyond the Standard Model (SM), precision measurements of B meson decays are being performed by the Belle II experiment. To enhance these measurements, efforts are currently being made to improve the instantaneous luminosity of the SuperKEKB collider. The target luminosity is $6 \times 10^{35}\,\mathrm{cm}^2/\mathrm{s}$. Simulations predict that, after 10 years of operation at this luminosity, the innermost layer of the Belle II silicon vertex detector (SVD) will have received a cumulative radiation dose of 20 kGy. As the SVD plays a crucial role in the detection of new physics, an evaluation was conducted by irradiating SVD sensors with electron beams to assess the potential operational impacts of this level of radiation exposure.

The following points should be understood in terms of the potential effects of radiation damage on the operation of the SVD:

1. The amount of radiation that causes type inversion of the sensor.
2. The increase of the full depletion voltage V_{FD} of the sensor.
3. The increase in the leakage current of the sensor as a rate of radiation (damage factor).
4. The increase in the interstrip capacitance.
5. The increase in the noise due to the increased leakage current and the interstrip capacitance.
6. The degradation of charge collection efficiency (CCE).

To evaluate these items, we performed IV, CV, and $\mathrm{C_{int}V}$ measurements and, noise, and CCE measurements.

A measurement system was developed for an electron irradiation test to sensors and it was utilized. The measurement system enabled remote switching of measurement circuits for IV, CV, and $\mathrm{C_{int}V}$ measurements for each irradiation dose, this is to acquire data during the testing period. To examine the changes in noise and CCE, we connected the sensor to the APV25 chips (SBW module) and acquired noise and collected change data using the beta-ray before and after irradiation.

Our conclusions corresponding to the enumerated items above is

1. The type inversion occurred in $15 \sim 20$ kGy just after irradiation. The irradiation damage is restored with the annealing effect of 1×10^3 hours, and we can confirm that the type inversion shifts to even higher doses $50 \sim 80$ kGy.

2. The V_{FD} was confirmed not to exceed 150 V at 80 kGy just after the irradiations. 80 kGy is 4 times the radiation dose that the innermost layer of the SVD receives in 10 years of operation of the target luminosity; safety factor 4. Additionally, through the annealing effect of 1×10^3 hours, it can be confirmed that the V_{FD} does not exceed 100 V even when a dose of 100 kGy is irradiated. On the other hand, The maximum voltage that can be supplied by the current SVD power supply is 200 V, therefore, Therefore, a bias voltage exceeding the SVD sensor's V_{FD} can be applied with the current power supply without any problem.

3. While the allowable current of our power supply module is 10 mA, It was confirmed that the leakage current does not exceed 10 mA up to 75 kGy immediately after irradiation. The damage factor was estimated to be 4 A/cm. On the other hand, the annealing effect recovered the radiation damage of the sensor and reduced the leakage current. This reduced the damage factor to 2.2 A/cm, and the power supply module is expected to withstand current increases up to 130 kGy. Therefore, there is no problem with the SVD operation in 10 years of target luminosity operation.

4. It was observed that as irradiation dose increased, $\mathrm{C_{int}}$ also increased. After 30 kGy irradiation, the maximum value of $\mathrm{C_{int}}$ is more than 2.6 times higher than that of unirradiated $\mathrm{C_{int}}$, but this value can be reduced to about 1.5 times by applying sufficient voltage beyond V_{FD} . The annealing effect also reduced $\mathrm{C_{int}}$ in the whole bias voltage range, i.e., the sensor surface damage was also recovered.

5. Measurements using the SBW module showed that the noise increased $\approx 400e^-$ before and after 100 kGy irradiation. This increase was found to be consistent with the increase in noise calculated from the increase in leakage current and the interstrip capacitance seen in the large sensor with the same dose, so these two factors can be attributed to the noise increase.

6. The MPV of the collected charge was found to drop by about $2\,\mathrm{k}e^-$ after irradiation. This is not because the CCE of the sensor itself has decreased, but rather because the threshold of the signal that can be collected as a cluster has increased due to the higher noise, and the amount of charge that was not collected as a signal has increased. Assuming the same noise before and after irradiation, the calculated value of the MPV of the collected charge did not differ significantly before and after irradiation, thus the CCE was hardly lowered.

In conclusion, based on the results of the evaluation, it was determined that the SVD is capable of functioning effectively even when exposed to radiation doses equivalent to SuperKEKB's target luminosity for 10 years of operation.

References

[1] *Luminosity projection of the SuperKEKB*, https://www-superkekb.kek.jp/Luminosity_projection.html.

[2] K. Adamczyk and Others (Belle II SVD collaboration), *The design, construction, operation and performance of the Belle II silicon vertex detector*, Journal of Instrumentation **17** (2022), no. 11, P11042.

[3] Kazunori Akai, Kazuro Furukawa, and Haruyo Koiso, *Superkekb collider*, Nuclear Instruments and Methods in Physics Research Section A: Accelerators, Spectrometers, Detectors and Associated Equipment **907** (2018), 188–199, Advances in Instrumentation and Experimental Methods (Special Issue in Honour of Kai Siegbahn).

[4] T. Akimoto, S. Arai, K. Hara, T. Nakayama, Y. Ikegami, Y. Iwata, H. Kobayasi, T. Kohriki, T. Kondo, I. Nakano, T. Ohsugi, M. Shimojima, S. Shinma, R. Takashima, S. Terada, N. Ujiie, Y. Unno, K. Yamamoto, and K. Yamamura, *Characteristics of irradiated silicon microstrip detectors with $\langle 100 \rangle$ and $\langle 111 \rangle$ substrates*, Nuclear Instruments and Methods in Physics Research Section A: Accelerators, Spectrometers, Detectors and Associated Equipment **466** (2001), no. 2, 354–358, 4th Int. Symp. on Development and Application of Semiconductor Tracking Detectors.

[5] T Antičić, R Battiston, W Braunschweig, Y.H Chang, C.-Y Chien, A.E Chen, S.R Hou, C.H Lin, W.T Lin, R Ostonen, K Spartiotis, O Syben, O Toker, and B Wittmer, *Energy straggling and multiple scattering in silicon strip detectors*, Nuclear Instruments and Methods in Physics Research Section A: Accelerators, Spectrometers, Detectors and Associated Equipment **374** (1996), no. 3, 309–314.

[6] Patricia Ball, Gareth W. Jones, and Roman Zwicky, *$B \to V\gamma$ beyond QCD factorization*, Phys. Rev. D **75** (2007), 054004.

[7] Thomas Bergauer, *Silicon Detectors in High Energy Physics*, https://www.oeaw.ac.at/fileadmin/Institute/HEPHY/PDF/ausbildung/teilchendetektoren/VO-4-2018-SemiconductorDetectors.pdf, 2017.

[8] C.M Buttar, P.P Allport, J.R Carter, G Casse, M.J Costa, I Dawson, L.M Drage, A Greenall, C Grigson, R.S Harper, J.C Hill, L.G Johansen, G Moorhead, D Morgan, R Nicholson, P Phillips, P Riedler, D Robinson, J Sanchez, S Stapnes, B Stugu, and A Werner, *Recent results from the atlas sct irradiation programme*, Nuclear Instruments and Methods in Physics Research Section A: Accelerators, Spectrometers, Detectors and Associated Equipment **447** (2000), no. 1, 126–132.

[9] C. Bozzi and Others, *The BaBar silicon vertex tracker*, Nuclear Instruments and Methods in Physics Research Section A: Accelerators, Spectrometers, Detectors and Associated Equipment **435** (1999), no. 1, 25–33.

[10] Belle II collaboration, *Belle II Technical Design Report*, (2010).

[11] M.J. French and Others, *Design and results from the apv25, a deep sub-micron cmos front-end chip for the cms tracker*, Nucl. Instrum. Methods. Phys. Res. A **466** (2001), no. 2, 359–365, 4th Int. Symp. on Development and Application of Semiconductor Tracking Detectors.

[12] K. Kang, *The Silicon Vertex Detector of the Belle II Experiment*, https://indi.to/7RR3N, 2022.

[13] G Lindström, S Watts, and F Lemeilleur, *3rd RD48 status report*, Tech. report, CERN, Geneva, 1999, Under the title: The ROSE collaboration (R & D silicon for future experiments).

[14] Michael Moll, *Displacement damage in silicon detectors for high energy physics*, IEEE Transactions on Nuclear Science **65** (2018), no. 8, 1561–1582.

[15] Hiroshi Nakano, *Search for new physics by a time-dependent CP violation analysis of the decay $B \to K_s\eta\gamma$ using the Belle detector*, http://hdl.handle.net/10097/58814.

[16] Etam Albert Noah Messomo, *Radiation and Temperature Effects on the APV25 Readout Chip for the CMS Tracker*, Ph.D. thesis, Imperial Coll., London, 2002.

[17] D. Pitzl, N. Cartiglia, B. Hubbard, D. Hutchinson, J. Leslie, K. O'Shaughnessy, W. Rowe, H.F.-W. Sadrozinski, A. Seiden, E. Spencer, H.J. Ziock, P. Ferguson, K. Holzscheiter, and W.F. Sommer, *Type inversion in silicon detectors*, Nuclear Instruments and Methods in Physics Research Section A: Accelerators, Spectrometers, Detectors and Associated Equipment **311** (1992), no. 1, 98–104.

[18] I. Rachevskaia, S. Bettarini, L. Bosisio, S. Dittongo, E. Quai, and G. Rizzo, *Radiation damage of silicon structures with electrons of 900mev*, Nuclear Instruments and Methods in Physics Research Section A: Accelerators, Spectrometers, Detectors and Associated Equipment **485** (2002), no. 1, 126–132, Proceedings of the 5th International Conference on Large Scale Ap plications and Radiation Hardness of Semiconductor Detectors.

[19] P. Raimondi., *2nd SuperB Workshop, Frascati, Italy*, 2006.

[20] Marthin Raymond, Marcus French, Jonathan Fulcher, G. Hall, L. Jones, Kostas Kloukinas, L.-K Lim, G. Marseguerra, Paulo Moreira, Quentin Morrissey, Andrea Neviani, and E. Noah, *The APV25 0.25 μm CMOS readout chip for the CMS tracker*, vol. 2, 02 2000, pp. 9/113 – 9/118 vol.2.

[21] V. Re and Others, *Radiation damage studies for the babar silicon vertex tracker*, Nuclear Instruments and Methods in Physics Research Section A: Accelerators, Spectrometers, Detectors and Associated Equipment **549** (2005), no. 1, 11–15, VERTEX 2003.

[22] Rey.Hori (KEK), *Overview of the Belle II detector*, https://www.kek.jp/ja/imagearchive/images/20180425_belle2_002.png, 2018.

[23] Keysight technologies, *Impedance measurement handbook 6th edition.*

[24] M. Valentan, *Beam test analysis status, SVD PXD meeting, Wetzlar (Germany)*, https://indico.mpp.mpg.de/event/2114/contributions/3489/attachments/2987/, 2013.

[25] Zihan Wang, private comminication.

[26] R. L. Workman and Others, *Review of Particle Physics*, PTEP **2022** (2022), 083C01.

[27] Zihan Wang, *Performance studies of Thin Fine-Pitch Silicon Vertex Detector forBelle II Vertex Detector upgrade*, Master's thesis, The University of Tokyo, 2022.

[28] 御子柴宣夫, 半導体の物理, 半導体工学シリーズ, 培風館, 1991.

[29] 森田 昭夫, *SuperKEKB* のマシンパラメータと *IR Optics* の設計 *(1)(2)*, http://accwww2.kek.jp/oho/OHOtxt4.html, 2019.

Acknowledgements

I first would like to express my sincere gratitude to my supervisor, Takeo Higuchi (樋口岳雄) for their unwavering guidance, encouragement and support throughout my studies. His dedicated mentorship has helped me to achieve my goals.

I would like to express my deep appreciation and gratitude to my co-researcher of this irradation test, Yo Sato (佐藤瑶), for not only his invaluable contributions to our campain and also his kind advise to my research life throughout his experience.

I also would like to express my deep appreciation and gratitude to Katsuro Nakamura (中村克朗) for his invaluable contributions and guidance. Without his expertise, dedication and hard work, I would not have been able to overcome the difficulties I faced during my research.

I would like to express my heartfelt thanks to Koji Hara (原康二), Toru Tsuboyama (坪山透), onuki Yoshiyuki (小貫良行) and Ishikawa Akimasa (石川 明正) for their immense support and kind advises.

I would also like to thanks to the SVD groups for their insightful and productive discussions.

I would like to thank Hikaru Tanigawa (谷川輝), Yuma Uematsu (植松佑真), Zihan Wang (王子涵), Tomoyuki Shimasaki (島崎奉文), Ping Ni (倪平), Xiaodong Shi (師暁東), Yuxin Liu (劉宇鑫), Hiroto Sudo (須藤裕人) who all have made my life in KEK enjoyable.

Thank you again to the member who participating in the radiation test.